

Multiobjective Optimization and Analysis of Slotted Waveguide
Antenna Stiffened Structures

Joseph Brooks

Dissertation submitted to the faculty of Virginia Polytechnic Institute and State

University in partial fulfillment of the requirements for the degree of

Doctor of Philosophy

In

Aerospace Engineering

Robert A. Canfield, Ch

Rakesh K. Kapania

Mayuresh J. Patil

Gary D. Seidel

John N. D'Angelo

September 23, 2022

Blacksburg, VA

Keywords: SWASS, multiobjective optimization, multifunctional

Copyright 2022, Joseph P. Brooks

Multiobjective Optimization and Analysis of Slotted Waveguide Antenna Stiffened Structures

Joseph P. Brooks

Abstract

Slotted Waveguide Antenna Stiffened Structures (SWASS) offer a new way to integrate the antennas used by many aircraft systems in modern aircraft. Looking at the weather radars used by current aircraft and using the loading estimates of the X-47B from Northrop Grumman, the designs went through several stages in the optimization procedure. The first stage centered around accounting for the stress concentrations present at the corners of the slots. These points led to local failure around the slots prior to the buckling of the overall structure, but the development of a concentration factor curve fit accounted for these in the optimization procedure and filled in a gap in the current literature. The models are then optimized, exposing a weakness in that these stress concentrations would lead to failure well before buckling in most designs with a loaded copper insert. To avoid this and shift most of the load to the supporting material, an initial gap is implemented in the eigenvalue buckling analysis, thus allowing for the simple 1-D models to be rapidly optimized without the need for contact modelling upon the gap's closure. The waveguide designs are then analyzed to ensure that the optimization of the individual waveguides is not prioritizing the structural performance to the detriment of the electromagnetic performance. Multiple points along the optimized Pareto front are tested and showed that their electromagnetic performance was consistent across the various regions of the front, and that the desired frequency of 10 GHz used by weather radars was within the optimal operational range for the various designs. Continuing from the individual waveguides now to larger panels, high fidelity models were used to develop another curve fit that relates the buckling of a panel simply supported on all four sides to the buckling of a single constituent waveguide simply supported on both ends. This curve fit is then used to validate the larger panel's performance against anticipated flight loads, without the need to model entire panels during the optimization procedure.

Multiobjective Optimization and Analysis of Slotted Waveguide Antenna Stiffened Structures

Joseph P. Brooks

General Audience Abstract

Modern aircraft utilize antennas for a variety of purpose, ranging from the weather radars in the nose of passenger airlines, to the communications antennas mounted on the exterior of military aircraft, and even the targeting radars used by weapons systems in modern military craft. However, these systems often require large empty spaces within the aircraft or interfere with the profile of the aircraft if mounted externally. Slotted Waveguide Antenna Stiffened Structures (SWASS) aims to eliminate these issues by integrating these antennas into the skin of the aircraft but uses the antennas themselves to help strengthen the structures, thereby eliminating the need to reroute the loads around them and making the aircraft lighter. These designs consist of a slotted metallic waveguide enclosed within supporting composite materials, which are substituted in place of the standard aircraft skin so as to fit seamlessly into the designs. Multiple issues can arise when attempting to do this, which this dissertation tackles. To develop optimized, multifunctional designs the dissertation balances the structural needs to integrate the designs into existing aircraft against the electromagnetic needs of the antenna systems it replaces. Gaps in the existing literature are addressed through the development of a curve fit to properly account for issues caused by the slots cut into the upper surface of the waveguides. New methods are also employed to simplify the optimization procedure. The first is reducing the load on the metallic waveguide through an initial gap by deriving a simplified model and eliminating the need for the complex models previously required. The next step is the creation of a new curve fit to relate the buckling of a single, less complex single waveguide model, to the buckling of the larger, more complex panel models. Throughout all of this, constraints and model validations are used to ensure that the designs meet their requirements, both as an antenna as well as a load bearing part of the aircraft's skin, specifically that of the X-47B.

Dedicated to my family, who have made it possible for me to pursue this degree.

Acknowledgements

I would like to thank Dr. Canfield, who has worked with and guided me over the past several years. Throughout the course of my graduate career, he has provided me multiple opportunities, both as part of my dissertation, but also as part of the wider AOE department and engineering field.

I would also like to thank Drs. D'Angelo, Kapania, Patil, and Seidel, who each agreed to serve on my advisory committee and over the course of several years have contributed to my growth as an Aerospace Engineer, with many of the things I learned from them directly contributing to this very dissertation.

Table of Contents

Abstract..... ii

General Audience Abstract.....iii

Acknowledgements v

List of Figures.....viii

List of Tablesxii

Chapter 1 1

Introduction..... 1

Motivation..... 2

Research Objectives..... 3

State of Prior Research..... 4

Research Contributions..... 6

Dissertation Organization 7

Chapter 2 Slotted Waveguide Stress Concentration Factor 9

1. Introduction..... 9

2. Concentration Factor Curve Fit 10

3. Multifidelity Design Application of Bivariate Fit..... 15

4. Multifidelity Design Application of Trivariate Fit with Composite Materials 19

5. Conclusion..... 20

Chapter 3 Electromagnetic Performance of Structurally Embedded Waveguides 21

1. Introduction..... 21

2. Model Verification 22

3. Optimized Designs..... 25

4. Conclusions 31

Chapter 4 Multifidelity Design of Structurally Embedded Waveguides 33

1. Introduction..... 33

2. Gap Modeling Using Prestress Terms..... 35

3. Single Waveguide Implementation 40

4. Optimization 44

5. Panel Application 51

6. Conclusions 56

Chapter 5 58

Future Work..... 58

Conclusions..... 59

Acknowledgements

Appendix A.	Corner Concentration Factor Data	61
Appendix B.	Stress Concentration Factor Supplemental Derivation.....	63
Appendix C.	AFRL Document	66
Appendix D.	Offset Gap Term Derivation	72
Appendix E.	Panel Curve Fit Data	75
Appendix F.	Design Variable Pareto Trends.....	76
References.....		81

List of Figures

Figure 1.1 A) Airborne Weather Radar [1] and B) F-18 with External Antennas Visible [2]. The dish in A requires a hollow nose cone, while the antennas in B are visible underneath the aircraft.	1
Figure 1.2 X-47B with Proposed Embedded Waveguide Panels. Concept created by Nick Albertson for SWASS implementation, showing the SWASS panels integrated into the upper skin of the aircraft’s wing [10].	3
Figure 1.3 Waveguide Dimensions and Nomenclature. The dimensions for the slot and waveguide are depicted on an example thin-walled waveguide.	5
Figure 1.4 Initial Candidate SWASS Designs. The designs iterate through material combinations and layups.	6
Figure 2.1 Roark Type 5 Irregularity. Roark’s Type 5 irregularity, as shown within Roark’s Table 17.1, is similar to the area between two slots on adjacent waveguides within an array [20].	9
Figure 2.2 Example Waveguide Array Element. Roark’s cases use the polynomial equation $K_t = C_1 + C_2(2h/D) + C_3(2h/D)^2 + C_4(2h/D)^3$, with the expansion on the right [20] similar to a subset of the waveguide array.	10
Figure 2.3 Waveguide Parameter Definitions. The full waveguide with material locations is shown on the left, material thicknesses (t_f , t_c , t_g) in the center, and the additional waveguide and slot specific parameters (d_1 – d_6) shown on the right.	11
Figure 2.4 Mesh Study Grids. The mesh was varied to ensure proper coverage of the fillet curves.	11
Figure 2.5 COMSOL FEM Data Compared Against Bivariate Fit for each D/d ratio of slot spacing to reduced width Data. Most cases track fairly well, with only one case slightly overestimating values and one case slightly underestimating values.	12
Figure 2.6 Bivariate and Trivariate fits for 10 mm slots. Both data sets track the two inner curves well, while the trivariate appears to be the more accurate of the two cases.	14
Figure 2.7 Bivariate and Trivariate fits for 15 mm slots. As with the 10 mm length slots, the trivariate form appears to track better, but now appear to overestimate the lowest D/d = 1.043 line.	14
Figure 2.8 Waveguide Configurations for A) Nominal Values and B) Optimized Values. The nominal design shows the larger initial slots and their squarer shape, while the optimized design shows the narrowed and rounded slots.	18
Figure 2.9 A) COMSOL Mesh Compared to B) Low-fidelity Design Model Mesh. The COMSOL mesh added many elements to fully capture the corner effects, while the fit allowed for the low-fidelity mesh to account for the corner stresses.	18
Figure 2.10 Stress Patterns for A) Nominal Slot Dimensions and B) Optimized Slot Dimensions. The nominal design shows higher stress concentrations at the corners, while the optimized form has reduced their magnitudes to a level closer to the rest of the waveguide.	19
Figure 3.1 Waveguide Concept and Components. A SWASS panel is composed of multiple singular waveguides consisting of an inner metallic core, surrounded by fiberglass and CFRP supporting material.	22
Figure 3.2 A) Cross-Sectional Profile and B) Lengthwise Profile. The signal propagates such that the electric field is maximum in the center and 0 at the edges, and also oscillates in accordance with the guided wavelength.	23
Figure 3.3 Model Gain Data. The models displayed larger maximum gains than the prediction, necessitating a fit.	24
Figure 3.4 Optimized Pareto Front. Optimization balanced minimum mass and maximum buckling designs while imposing electromagnetic performance constraints.	27

Figure 3.5 CREATE-RF™ SENTRI Fillet Meshing. The filleted slot models used dozens of triangular elements to properly capture the curve of the fillets at each corner..... 28

Figure 3.6 Design 45 with A) Filleted Slot Corners and B) Square Slots. The presence of fillets on the corners of the slots has a minimal effect on the gain’s magnitude and has no observable effect on the radiation pattern [38] [30]. 29

Figure 3.7 10 GHz Radiation Pattern for A) Design 25, B) Design 35, and C) Design 25. All three designs have identical radiation patterns, with small variations in peak gain [38] [30]. 29

Figure 3.8 Frequency Sweep Results. Designs 35 and 45 have nearly identical regions of peak performance, and a wider operational range than the nominal design, but a lower peak gain. 30

Figure 4.1 Offset Proposal. The supporting material will extend a distance δ beyond one end of the waveguide insert. 33

Figure 4.2 Waveguide Concept and Components. The SWASS panel is composed of the inner metallic waveguide, fiberglass sleeve and outer mold line, and CFRP inner mold line, with the material thicknesses and waveguide dimensions specified by its target function. 34

Figure 4.3 Model Fidelities. A) Finer mesh would require remeshing every time parameters are changed. B) A coarse mesh that can be easily updated within an optimization routine. 34

Figure 4.4 Varying Cross Section. Along the waveguide’s length, the presence of a slot causes the waveguide’s cross section to change, influencing its stiffness, between unslotted cross sections (A) and slotted cross sections (B). 40

Figure 4.5 Nominal Buckling Analysis. Buckling occurs before unslotted copper failure, but local failure at slot corners occurs well before buckling..... 42

Figure 4.6 Gap Implementation. Inclusion of an initial gap delays the copper loading, allowing the supporting materials to take the majority of the load and prevent local failure of the slot corners. 43

Figure 4.7 Critical Load vs. Gap Length. As the gap length increases, more and more of the load is absorbed by the supporting material. 43

Figure 4.8 Dimpled Panel Model. Narrower panels pinned on all sides tended to see local failure, known as dimpling..... 47

Figure 4.9 Optimized Pareto Front. The gap allowed for designs with lower masses and/or stronger buckling loads, while the front without a gap is entirely dominated. 49

Figure 4.10 X-47B Dimensions and Areas. Using the listed dimensions, the required areas, lengths, and thicknesses could be estimated [25]..... 51

Figure 4.11 X-47B Moment Distribution. The moment decays exponentially as it approaches the wingtip. 51

Figure 4.12 Load per Unit Span. The shortening chord lengths result in a spike near the hinge. 52

Figure 4.13 Panel Optimization Location. The test panel is placed in a location between two confirmed supports due to the underlying structure not being publicly available [50]. 53

Figure 4.14 COMSOL Data and Curve Fits. The curve fit tracks the COMSOL data, following an exponential decay..... 53

Figure 4.15 12 Waveguide Panel Optimization. The lower half of the front keeps the copper to a minimum by increasing the supporting materials, while the upper half is forced to add back copper to further increase its strength..... 55

Figure 4.16 Optimum Panel Buckling Mode A) Corner View and B) Top View. The optimum design buckles with a global mode when constrained on the nodal axis..... 56

Figure A.1 Roark Type 5 Irregularity vs. Trivariate Fit for 10 mm Slots. As the D/d ratio increases, Roark’s fit becomes less and less accurate, while the Trivariate Fit maintains its accuracy throughout.... 62

Figure A.2 Roark Type 5 Irregularity vs. Trivariate Fit for 15 mm Slots. Just as with the 10 mm Slots, Roark’s fit decreases in accuracy as D/d increases, while the Trivariate Fit maintains its accuracy throughout.	62
Figure C.1 Antenna Array Under a Radome. The slotted waveguide array is housed within the large void in the nose [1].	66
Figure C.2 SWASS Panel Design. The inner conductive material acts as the antenna, while the additional wrap and mold lines provide additional structural support.	67
Figure C.3 Waveguide Dimensions. A slotted waveguide’s dimensions are divided between those corresponding to the slot size (d_1 and d_2), slot locations (d_3 and d_4), and waveguide dimensions (d_5 and d_6).	67
Figure C.4 A) COMSOL Waveguide Model and B) CREATE-FT Capstone Waveguide Model. The COMSOL model shows the spherical volume of air modeled around the waveguide itself, while the waveguides themselves are consistent with one another.	68
Figure C.5 Full Waveguide Model. The full model includes the metallic waveguide at the center, along with the additional supporting sleeve and face sheets.	69
Figure C.6 Full Panel Model. Five identical versions of the previous full waveguide model are combined in an array to create an example panel, but can be varied for any desired size	69
Figure C.7 A) COMSOL 10 GHz Radiation Pattern and B) CREATE-RF™ SENTRi 10 GHz Radiation Pattern. Both models show the circular radiation pattern with decreasing magnitude as you move away from the vertical immediately above the slotted surface.	69
Figure C.8 COMSOL Frequency Sweep Peak Gain Values. The waveguide’s design appears to keep the peak frequency closer to the 10 GHz design of a WR-90 style waveguide antenna. Smaller gain values seem to indicate a wider operating range between 8.9 GHz and 10.9 GHz.	70
Figure C.9 CREATE-RF™ SENTRi Frequency Sweep Peak Gain Values. The inclusion of the waveguide’s thickness appears to have shifted the peak frequency closer to 10.3 GHz and slightly narrowed the operating range to between 9.1 GHz and 10.7 GHz.	70
Figure C.10 COMSOL Panel Radiation Pattern for Simultaneous Firing. The patterns from each waveguide combine in a way that results in two main lobes approximately 40 degrees off from vertical.	71
Figure C.11 CREATE-RF™ SENTRi Radiation Patterns for Each of the Five Port Fired Individually. Each port appears to resemble a slightly rotated version of the single waveguide’s pattern in Fig. C.7b, changed due to the presence of the other waveguides.	71
Figure E.1 Panel Buckling Data Sets. When pinned on two sides, designs buckle at loads roughly equal to the array length times the original buckling load, while designs pinned on four sides buckle at loads that exponentially decay towards the simply supported on two sides as the width approaches the length.	75
Figure E.2 Panel Buckling Fit. The curve fit closely matches the majority of data points, with only a single outlying set outside of the fit lines.	75
Figure F.1 Slot Width Pareto Trend. The Slot width remains at its maximum value with small spikes, likely from convergence issues.	76
Figure F.2 Slot Centerline Offset Pareto Trend. The centerline offset increases it becomes 10 percent greater than the optimal value, followed by a region of instability as the active constraints change, then a slow decrease as the dimpling constraints deactivate.	77
Figure F.3 Waveguide Height Pareto Trend. The height increases linearly from its minimum to its maximum to increase the stiffness of the designs.	77
Figure F.4 Slotted Copper Thickness Pareto Trends. The slotted copper thickness remains roughly constant for all designs, with only slight variations caused by the convergence of the solver.	77
Figure F.5 Unslotted Copper Thickness Pareto Trends. The unslotted copper thicknesses remains roughly constant for all designs, with similar variations to the slotted copper thickness.	78

Figure F.6 Fiberglass Sleeve Thickness Pareto Trend. The sleeve thickness increases until reaching a point where the inner mold line begins to thicken for additional strength, remaining constant until the inner and outer mold lines have reached their maximum thicknesses. 78

Figure F.7 Fiberglass OML Thickness Pareto Trend. The OML thickness remains small until the height peaks, after which it begins to increase linearly until reaching its maximum value. 78

Figure F.8 0° Ply Thickness Pareto Trend. The 0° plys increases linearly, with the slope increasing slightly after the height reaches its maximum. 79

Figure F.9 90° Ply Thickness Pareto Trend. The 90° plys remained roughly at their minimum with slight variations due to convergence. 79

Figure F.10 Fillet Radius Over Slot Width Pareto Trend. The fillet radius remains close to its maximum of half the slot width, but has some variations where active constraints begin to change and begins to decrease as the designs become stiffer. 79

Figure F.11 Offset Pareto Trend. The offset increased linearly until the height reached its peak, after which it decreased as the inner and outer mold lines thickened, only increasing again once both reach their maximum values. 80

Figure F.12 Concentration Factor Pareto Trend. The concentration factor is kept low until the fillet radius begins to decrease in the higher mass designs. 80

Figure F.13 Panel Factor Pareto Trend. As the designs become stronger, the panel factor decreases, not increase again until the inner and outer mold lines reach their maximum and the sleeve thickness begins increasing again. 80

List of Tables

Table 2.1 Bivariate Solution Weakness. When either equation is applied to slots outside of its original data set, it losses accuracy.	13
Table 2.2 SQP Optimization Results for a Copper Waveguide. The slots were expanded and the height and thickness reduced with buckling was not constrained, while constraining the buckling resulted in smaller slots and increased fillet radii.	17
Table 2.3 Optimization of a Full Waveguide Design. The reduction in mass from decreasing the copper thickness offsets the increase due to increasing the thickness of the supporting materials, while also increasing the overall buckling load.	20
Table 3.1 Waveguide Dimensions.	21
Table 3.2 Geometric Constraints.	25
Table 3.3 Electromagnetic Constraints.	26
Table 3.4 Design Dimensions.	27
Table 3.5 10 GHz Peak Gain Data.	30
Table 3.6 Frequency Sweep Peak Data.	31
Table 4.1 Variable Nomenclature.	41
Table 4.2 Material Properties.	41
Table 4.3 Geometric Constraints.	45
Table 4.4 Stress Constraints.	45
Table 4.5 Gap Constraints.	46
Table 4.6 Electromagnetic Constraints.	46
Table 4.7 Panel Constraints.	47
Table 4.8 Pareto Design Point.	50
Table 4.9 Optimized Element and Objective Values.	50
Table 4.10 Pareto Optimal Objective Values.	50
Table 4.11 Optimized Panel Dimensions.	55
Table 4.12 Panel Optimized Properties.	56
Table 4.13 Pareto Optimal Panel Design.	56
Table A.1 Mesh Refinement Values. Finest mesh stress concentration factor converged to two significant digits.....	61
Table A.2 Residuals for Each D/d Value. Global bivariate fit has a residual similar to the univariate models created for each individual model. With the overall accuracy of the same magnitude.	61
Table A.3 Residuals for Global Fits for Each D/d Value. Bivariate fit is no longer able to maintain its accuracy for multiple slot lengths, with the inclusion of the slot-corner-distance term in the trivariate case recapturing the accuracy of the univariate fit.....	61
Table C.1 Nominal Waveguide Dimensions. The base waveguide dimensions correspond to a WR-90 designed to operate at a frequency of 10 GHz.	68

Chapter 1

Introduction

As aircraft have proliferated over the decades, designs have been constantly improved and streamlined. Every piece on an aircraft has a specific function to perform, but many modern designs have begun using multifunctional components, where a single portion of the aircraft is required to fulfil multiple requirements simultaneously. Multifunctional designs allow for tasks that previously would require multiple pieces, to now be fulfilled by a single design, eliminating the weight or design penalties of the previous iteration. However, this also means that the designs must find a balance between the requirements of each function, as they are often at odds with one another.

One area of particular interest is centered on the electromagnetic (EM) equipment employed by current aircraft in both civilian and military capacities. Many of these systems require large empty spaces within the aircraft for the things such as the radar antenna in Fig. 1.1A, or externally mounted antenna as in Fig. 1.1B. The former can cause issues in designs, as it limits the shape of certain areas of the aircraft, while the latter can interfere with aerodynamic profiles, as well as the stealth capability of more recently developed military aircraft.

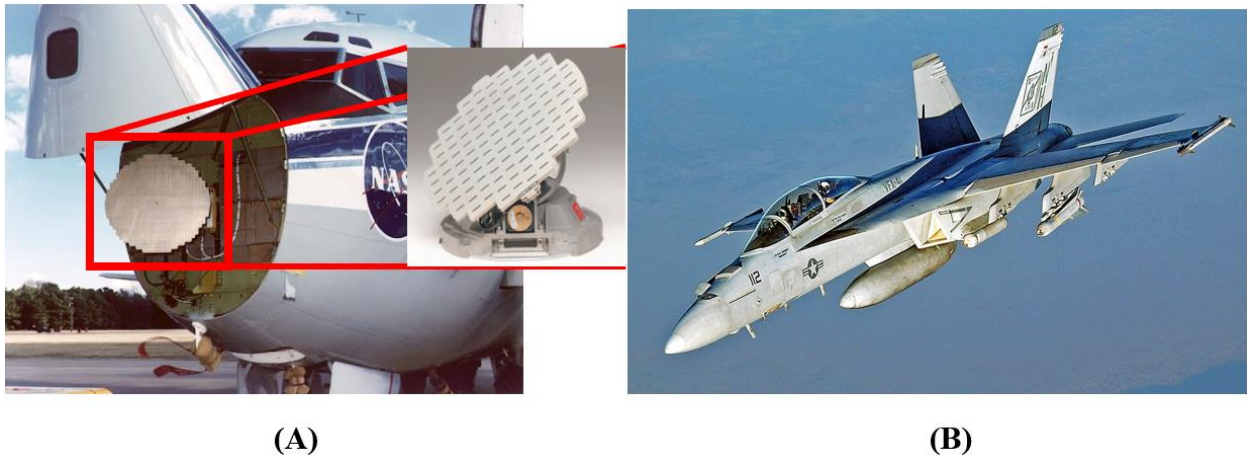


Figure 1.1 A) Airborne Weather Radar [1] and B) F-18 with External Antennas Visible [2]. The dish in A requires a hollow nose cone, while the antennas in B are visible underneath the aircraft. However, alternatives have been proposed to deal with these issues. A form relevant to this document, known as Conformal Load-Bearing Antennae Structures (CLAS), was examined by Paul Callus. These early designs were composed of a series of layers in which a conductive antenna would be embedded within a supporting structure that diverted the loads around the antenna itself. However, these designs are limited by their complexity and difficulty to integrate into existing aircraft [3].

Further refinement led to Callus examine a series of novel designs to account for these issues. One such design was the Slotted Waveguide Antenna Stiffened Structure (SWASS), which refined an earlier slot-array concept by initially combining it with the stiffeners in aircraft skin designs. Later designs included the idea of integrating the slot bases into the center of the skin support material, with the inner layers providing structural support while an electromagnetically transparent material composed the outer mold line [4]. The design was further refined and tested in an experiment conducted by Callus et al., in which a Carbon-Fiber Reinforced Polymer (CFRP) array of 10 waveguides was created and tested as a viable iteration of the design [5]. Similar designs were also examined by Sabat, but found that the designs relying solely on CFRP could not support sufficient loading to justify their use over other materials such as aluminum, recommending thicker designs to compensate for the penalties from the slots [6]. While Sabat focused on the structural side, other research such as Bojovschi et. al. looked into the electromagnetic performance of CFRP waveguides and the effects of their layup schemes [7].

With the viability of the designs confirmed, the next step in the concept's development came at the hands of Kim, Ha, and Canfield. In their work, Callus's SWASS design was refined and optimized, with the first study looking at the effects of each waveguide dimension on the electromagnetic performance [8]. They then examined several potential structural designs that will be detailed in a later section [9]. These designs formed the base for the research to be detailed in the succeeding chapters, which will detail the structural optimization and refinement of the designs. The electromagnetic performance was examined in more detail by Albertson and Canfield [10], and used to build the groundwork from which this research grows.

Motivation

To ensure proper analysis and consideration of real-world requirements, the X-47B unmanned combat aerial vehicle designed by Northrop Grumman is used as a case study. The SWASS panels are designed to fulfill a role as weather radar using an X-band (10 GHz) frequency. The same case study was used for an analysis by Albertson, who focused on optimizing the waveguide itself [11]. Continuing from this point, the current research aims to perform a multi-objective optimization of the full structure, including the waveguide itself, as well as the supporting materials. In the course of this optimization, maximizing the buckling load and minimizing the mass will be the driving forces within the structural optimization, while ensuring the peak frequency of the waveguide remains as close to the target frequency of 10 GHz governs the electromagnetic side, and ensuring that the structural aspect do not compromise its performance.

Research Objectives

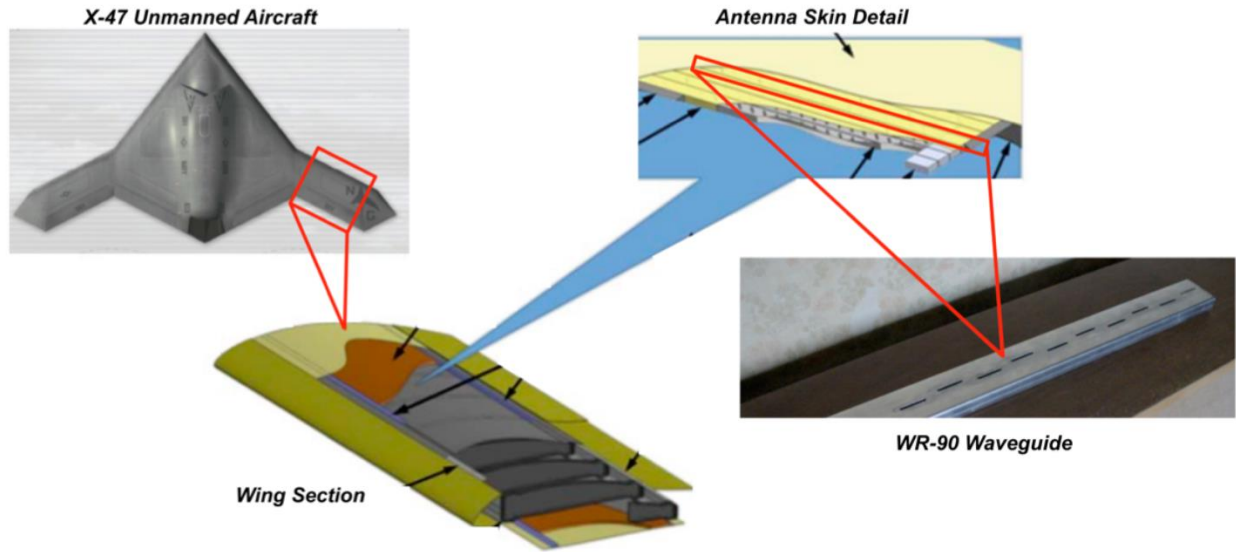


Figure 1.2 X-47B with Proposed Embedded Waveguide Panels. Concept created by Nick Albertson for SWASS implementation, showing the SWASS panels integrated into the upper skin of the aircraft's wing [10].

The buckling load will be compared against example flight loads calculated for the X-47B to verify it meets requirements, while the resulting electromagnetic profile will be analyzed to ensure estimated peak frequency matches with the predicted peak frequency of a high-fidelity modeler.

Research Objectives

The overarching goal of this research is to verify the SWASS concepts and show whether or not they are viable for implementation on the X-47B platform in place of its weather radar systems. Doing so may facilitate the creation of a new approach to analyze the system structurally, eliminating the high-fidelity models currently required and replacing them with a lower-fidelity alternative that reduces the overall computational costs for analysis and optimization. Such a system will allow for optimized panels to be analyzed and designed against example flight and mission requirements at a fraction of the current computational cost. Based upon the previous iterations of the designs and their analyses, a series of more focused research of research objectives was created, including: creating a governing equation to model the stress concentrations that occur at the corners of the slots cut into the waveguide, due to their shape not matching any known stress concentration formula; integration of electromagnetic performance as a design objective alongside the structural objectives, as well as validation of the designs' electromagnetic performance using both commercially available analysis software and the Department of Defense's High Performance Computer Modernization Program (DoD HPCMP) in-house developed CREATE-RF™ SENTRI module; and creation of an

eigenvalue analysis of the buckling problem capable of handling the discontinuous stiffness created by an initial offset within the design. The first objective was achieved as part of a paper included within Chapter 2 of the dissertation, while the electromagnetic performance of the second objective is quantified in Chapter 3 and the modeling of the offset and panel form of the waveguides is detailed in Chapter 4.

State of Prior Research

In 1999, Lockyer et al. published a study sponsored by the Air Force Research Laboratory, entitled the Smart-Skin Structure Technology Demonstration (S³TD). Within this study, an initial CLAS design, composed of a spiral multi-armed spiral antenna designed for operation in the 0.15 to 2.2 GHz frequencies, was integrated into a panel designed to be fitted into an F-18, F-22, or similar fighters and unmanned platforms. The study showed the design withstood the example loading case of an F-18 over the 6,000-hour fatigue life, while also handling the electromagnetic requirements placed upon it [12]. Alt et al. published a second study in 2001, giving an overview of the Department of Defense's RF Multifunction Structure Aperture Program (MUSTRAP). A similar multi-armed spiral antenna was tested under axial and shear loading consistent with fuselage loading over a 6,000-hour service life, while an additional vertical tail end cap design was tested against the acoustic environment caused by the empennage noise and aimed at increasing the voice communications range from 30 to 400 MHz. These designs showed promise, withstanding the loading requirements, while still meeting the electromagnetic requirements and resulting in a net mass reduction in the aircraft systems [13].

While the aforementioned studies looked at the general viability of CLAS panels themselves, additional studies were conducted to measure the effect of wing bending and deformation on proposed CLAS panels integrated into the wings of a joined-winged sensor craft. Smallwood, Canfield, and Terzulio found that the electromagnetic performance was sensitive to the bending of the wing itself, with gust and maneuver loading potentially causing enough bending to shift the main beam elevation angle significantly enough for the phased array to compensate for [14]. Additional research by Urcia and Banks looked into integrating load bearing structural phased arrays composed of embedded antenna elements into various structures of an aircraft, such as doors, wing panels, and fairings. They showed that the designs which could be integrated into these various structures were viable within tertiary structures, resulting in net weight reductions without compromising the structural capabilities of the designs [15].

From this point, the research that immediately precedes that presented in this document, shifts to focus on designs similar to the SWASS designs proposed by Callus [5]. The waveguides themselves were governed by the equations

State of Prior Research

laid out by Elliott that govern waveguide antenna performance based upon the size and shapes of the slots and waveguide itself [16].

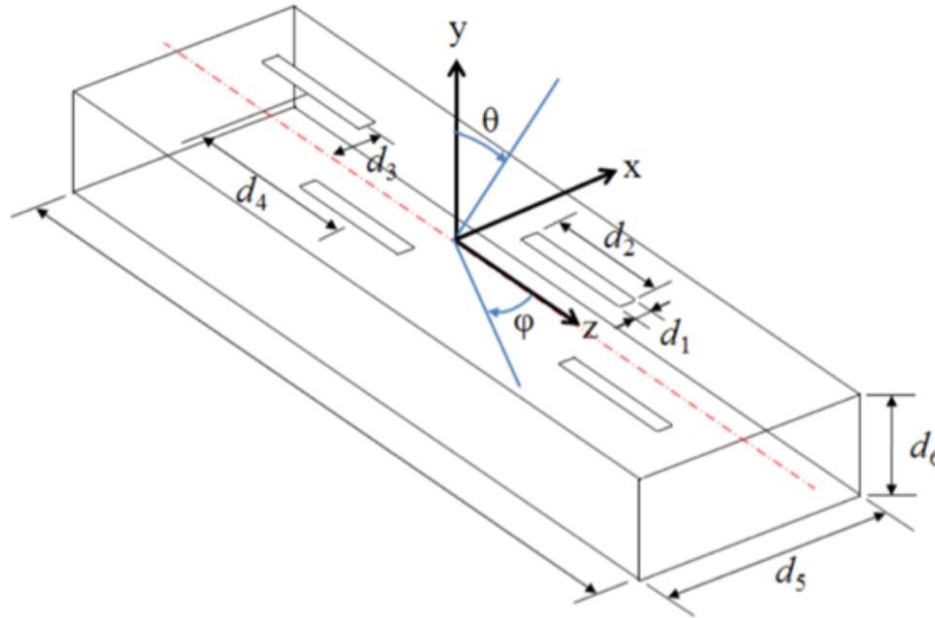


Figure 1.3 Waveguide Dimensions and Nomenclature. The dimensions for the slot and waveguide are depicted on an example thin-walled waveguide.

Ha and Canfield studied the effects of varying each of the waveguide's design variables shown in Fig. 1.3 (d_1 - d_6) on the electromagnetic performance of the waveguide was analyzed. They found that the slot length (d_2), slot longitudinal spacing (d_4), and waveguide width (d_5) had the greatest effects upon the design's electromagnetic performance [17]. Manipulating these parameters would have the greatest effect on the electromagnetic performance. Work conducted by Kim et al. proposed the four potential designs for a SWASS panel shown in Fig. 1.4. The first concept makes use of CFRP for all layers; however, this does not permit electromagnetic signals to pass through freely, requiring slots be cut in the outer surface and filled with an electromagnetically transparent material. These designs resemble those examined by Sabat [6] and Bojovschi et. al [7]. The second and third designs replaced the outer and inner mold lines with fiberglass, which is electromagnetically transparent, with the former retaining the Carbon-Fiber Reinforced Polymers (CFRP) waveguide while the latter replaced it with a metallic waveguide surrounded by fiberglass. The fourth design matched the third, but now with a CFRP inner mold line for additional strength. Analysis showed that the fourth design had the best performance [18] and was chosen as the basis for the work presented in later portions of this document, despite concerns regarding buckling end conditions in the original work.

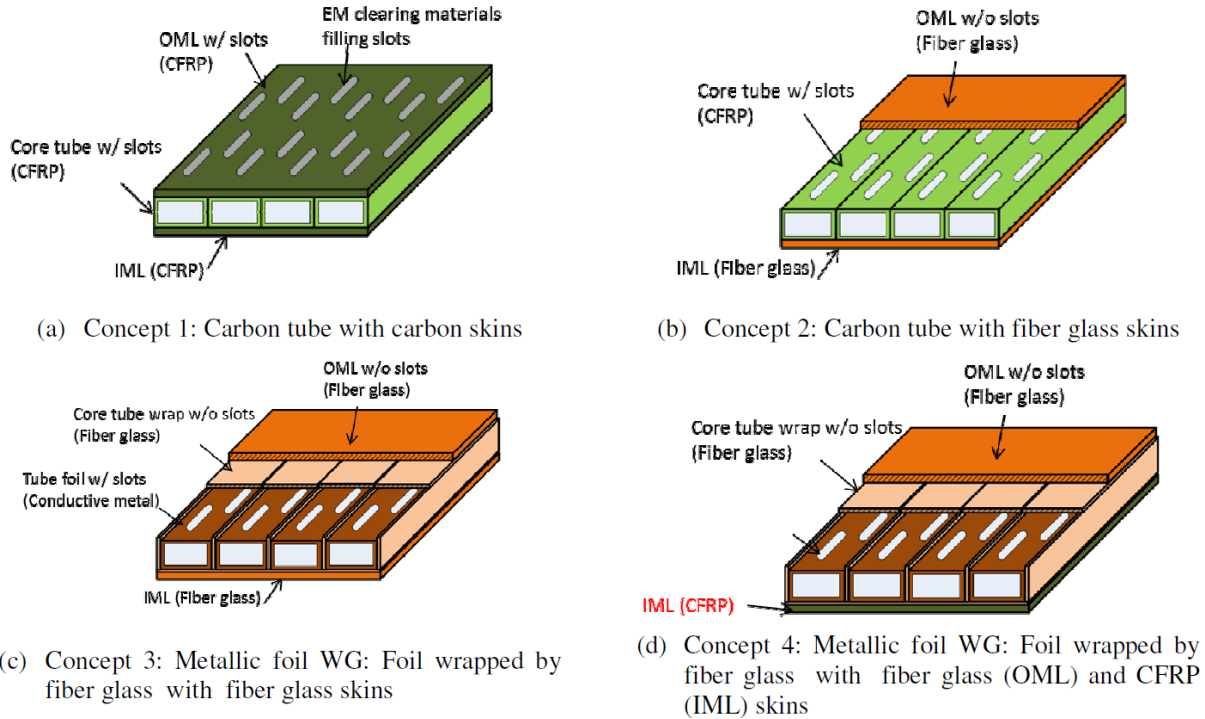


Figure 1.4 Initial Candidate SWASS Designs. The designs iterate through material combinations and layups.

The direct predecessor to this document is the work coming from Albertson, which showed the waveguide design could be optimized to meet weather radar performance requirements, while also including initial structural requirements on mass and buckling performance [19].

Research Contributions

Over the course of this dissertation, several advancements were made in the study and modelling of slotted waveguide antenna stiffened structures. The first of these was the creation of a curve fit that filled in a gap in the existing literature for stress concentration factors. Prior literature dealt in larger filleted structures, such as Roark’s Formulas for Stress and Strain [20], but none matched the size and shape of slots in a waveguide. This necessitated a new curve fit to account for curves that were smaller and closer together than pre-existing fits. The resulting fit can be used not only for slotted waveguides, but for similar structures that Roark’s equations cannot be applied to.

In combination with the concentration factor fit, the implementation of fillets into a slotted waveguide was another area of study that had not been examined in prior literature. Traditionally, slots in a waveguide are typically shown as square, with sharp turns at each of its four corners. In the course of electromagnetic analysis, the effects of the slot fillets were examined, showing that despite being varied from their maximum size of half the slot width back to zero

Dissertation Organization

for a square slot, the gain showed no detrimental effects. This was also part of a wider multifidelity analysis that combined the electromagnetic and structural analyses together, where earlier analyses largely kept the two separated from one another.

The next area of advancement was the inclusion of an initial gap term in the eigenvalue buckling analysis. Before, properly modelling such a gap would require a higher fidelity model with contact modeling. While the term had been used in prior research for eigenfrequency analysis, it had never been used for an eigenvalue buckling analysis. This allowed the modeling of individual waveguides to be simplified to low fidelity 1-D models for rapid optimization, which could then be combined into larger panel models through the use of a panel fit similar to the one generated for the stress concentrations at the slot corners. The panel fit relates the buckling load of a single waveguide pinned on both ends to the buckling load of a panel composed of multiple waveguides and pinned on all four sides. This fit can be used to eliminate the need for higher fidelity panel models and streamline the optimization process even further. All of these advancements help contribute to an optimization protocol that can generate multiple waveguide designs that range from minimum mass to maximum buckling.

Dissertation Organization

The remaining chapters of the document shall focus on each of the research topics outlined above and their findings. Chapter 2 consists of the work co-authored by Dr. Canfield and published in the AIAA Journal “Slotted Waveguide Stress Concentration Factor,” [21] along with its supporting calculations. This will include the governing equations used within buckling and mass analyses, as well as all the equations and data created for modeling the stress concentrations at the corners of the slots. To maintain the consistency of the original journal article, the supporting mathematics and governing equations that are used within it are discussed within Appendix B.

Chapter 3 is composed of an article being prepared for future publication composed of work overseen by Dr. Canfield and with the aid of Dr. D’Angelo. Within it, the paper examines the electromagnetic performance of several optimized designs and the effects of implementing fillets on the corners of the slots. Multiple models from various locations along the Pareto front are modeled to ensure that the performance is consistent along the entire front, while frequency sweeps are used on two models to confirm the operational frequency range of the designs and ensure that they are not shifted away from the desired operational frequency of 10 GHz. An earlier form of these analyses was conducted as part of a project for the Air Force Sensors Directorate designed to compare the HPCMP’s CREATE-

RFTM SENTRi modelling software against the commercially available COMSOL Multiphysics, which is included in Appendix C.

Chapter 4 is composed of an article co-authored by Dr. Canfield and submitted for publishing in an AIAA Journal entitled “Multifidelity Design of Structurally Embedded Waveguides.” The chapter includes the derivation and implementation of a term to account for an initial gap in the eigenvalue buckling analysis and a new curve fit used to link the buckling load of a single waveguide simply supported on two ends to the buckling load of the larger panel that is simple supported on all four sides. The intermediate steps used in the derivation of the gap term are included within Appendix D, while the data used to derive the panel fit equation are included within Appendix E. Finally, Chapter 5 includes the final conclusions and important points from each of the preceding three chapters, as well as recommendations for future work.

Chapter 2 Slotted Waveguide Stress Concentration Factor

1. Introduction

The overall shape of a structure under load can lead to certain areas having a higher stress than others. Often, these stress concentrations are the result of sudden changes in the structural layout, such as sharp turns, and act as the most likely failure points within a structure. As a result, it is important to estimate what the increased stresses will be to prevent any local failures that could lead to an overall compromise of the structure. Within a load-bearing slotted waveguide, these stress concentrations occur at the corners of the slots cut into the waveguide's surface. The ratio between this higher corner stress and the uniform stress away from the point of interest is defined as a concentration factor, K_t , and can be used to estimate the corner stress from a given uniform stress.

In linear elasticity theory, the stress at a sharp corner is singular and will tend to infinity. Nonetheless, no crack or corner is perfectly sharp, resulting in a measurable, but finite, stress increase. As a result, a rounded corner, or fillet, is usually introduced to limit stress at these points of interest. Elasticity solutions are rarely available for more than simple geometries, so the effects of the fillets are often studied by refining meshes of numerical models to best capture the behavior. Many widely used shapes are then generalized into an empirical curve-fit, such as those found in *Roark's Formulas for Stress and Strain*, that can be employed for design calculations. For the waveguide structure, Roark's type 5 fillet, as shown within the portion of Table 17.1 [20], replicated in Figs. 2.1) and (2.2), was used as a guide for expected results, due to the similarity between its shape and a filleted waveguide slot, except for a slot that would be caught within the central area of the equivalent Roark irregularity.

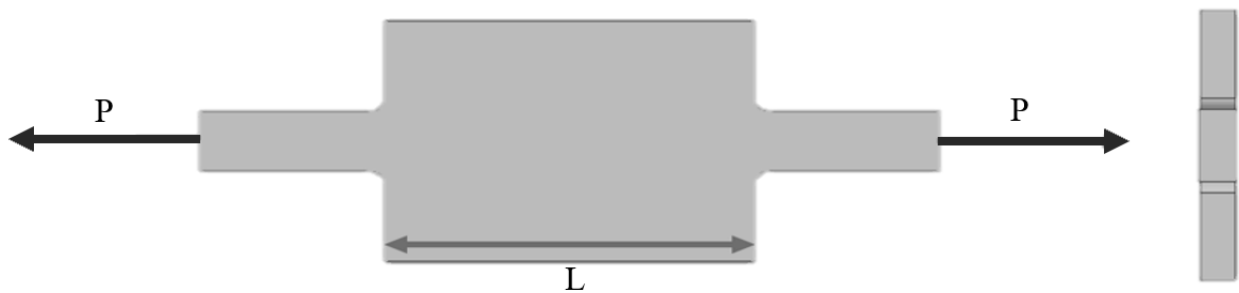


Figure 2.1 Roark Type 5 Irregularity. Roark's Type 5 irregularity, as shown within Roark's Table 17.1, is similar to the area between two slots on adjacent waveguides within an array [20].

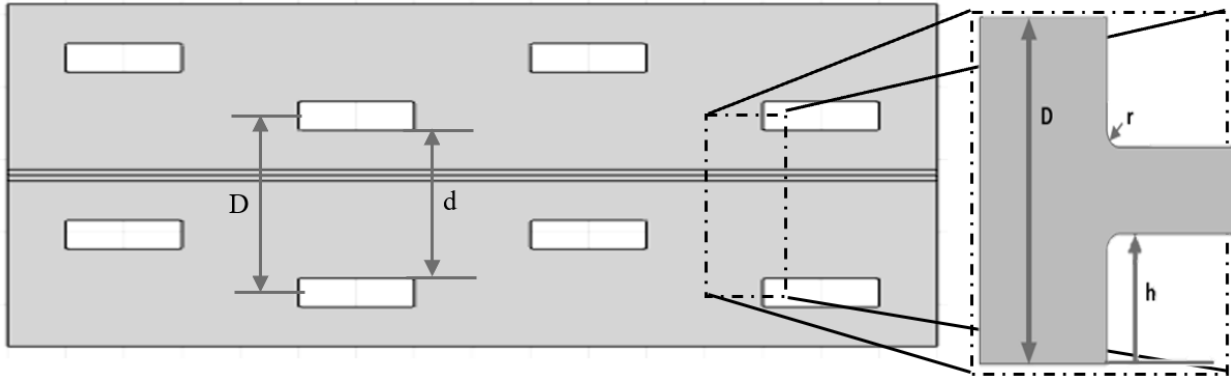


Figure 2.2 Example Waveguide Array Element. Roark's cases use the polynomial equation $K_t = C_1 + C_2(2h/D) + C_3(2h/D)^2 + C_4(2h/D)^3$, with the expansion on the right [20] similar to a subset of the waveguide array.

The concepts are based on earlier studies conducted by Kim and Canfield, in which multiple potential waveguide configurations were analyzed. While some concepts kept the waveguide itself unloaded, others examined the idea of the waveguide itself bearing part of the load [17] [22]. As such, the concentration factors caused by the slots are of interest, to ensure accurate low-fidelity structural models of the waveguide. These low-fidelity models will allow for designs to be compared against design requirements quickly and efficiently. The analysis herein began with a purely copper waveguide, finding an empirical curve fit for the waveguide slot stress concentration, before then moving on to its role within a larger optimization and use within a composite design.

2. Concentration Factor Curve Fit

For a given waveguide, the dimensions that affect the overall shape are the individual width of each waveguide ($d_5 = 22.86$ mm), the thickness of the fiberglass sleeves encasing each waveguide ($t_f = 0.75$ mm), the varying slot width (d_1), and slot centerline spacing (d_3). These parameters and additional parameters used later can be seen in Fig. 2.3, with the waveguide layup shown on the left [18], the waveguide sleeve material thicknesses shown in transparency in the center, and the dimensions specific to the copper waveguide itself shown on the right. The nomenclature employed for the waveguide itself (d_1 - d_6) were adopted as a continuation of the nomenclature employed in Kim and Canfield, while the design layup shown on the left corresponds to the fourth design in an earlier study by Kim and Canfield that examined their influence on electromagnetic performance [18].

Concentration Factor Curve Fit

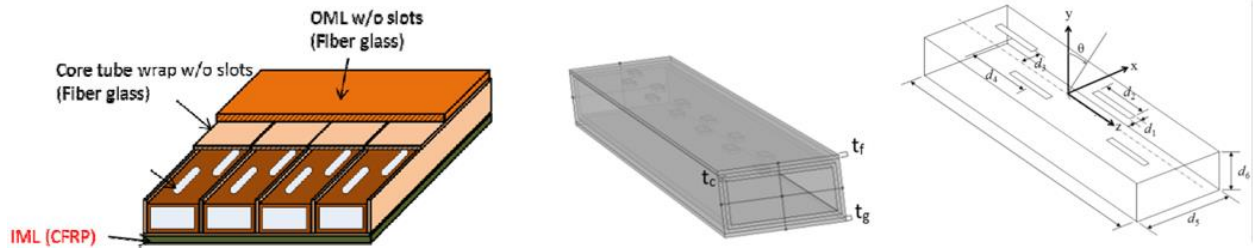


Figure 2.3 Waveguide Parameter Definitions. The full waveguide with material locations is shown on the left, material thicknesses (t_f , t_c , t_g) in the center, and the additional waveguide and slot specific parameters (d_1 – d_6) shown on the right.

A mesh convergence study was conducted to ensure the changes in stress concentrations were properly captured. Three meshes were tested, as shown in Fig. 2.4. The “Fine” mesh had seven nodes along the curvature of the fillet and 4,212 elements. The “Finer” mesh increased the number of nodes on the fillet to eight. Further refinement from 5,322 elements to 7,900 elements in the “Finest” mesh did not change the number of nodes along the fillet. The concentration factor only varied slightly with mesh refinement, as shown in Table 6.1 of the Appendix A.

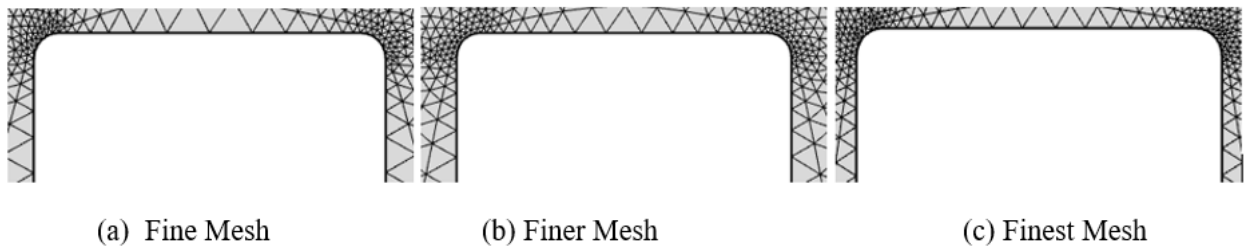


Figure 2.4 Mesh Study Grids. The mesh was varied to ensure proper coverage of the fillet curves.

The fillet radius, r , at the corners of the slots was varied from half of the slot width down to $1/12^{\text{th}}$ or $1/16^{\text{th}}$ of the slot width, depending upon the slot width’s magnitude. This process was repeated for four slot widths, ranging from 1 millimeter to 4 millimeters, using a slot length of 10 millimeters. For each combination of slot size and fillet radius, the concentration factor is determined by dividing the von Mises stress at the corner node, σ_{corner} , by the nominal (applied) stress in the unreduced area, σ_1 .

$$K_t = \frac{\sigma_{corner}}{\sigma_1} \quad (2.1)$$

The von Mises stress was chosen for the isotropic material (copper in this case) failure criterion, due to it being more restrictive than the principal stresses alone. However, data was also taken for principal stress, as well as von Mises stress for both tensile and compressive loads to ensure the most conservative design. The data shown corresponds to the compressive von Mises case, as it was roughly equal to the tensile case and only slightly higher than the principal

stress case. Fig. 2.5 shows the data for each of the four designs modeled with a unit compressive load, labeled as COMSOL FEM data.

Curve fits were then created for the data collected from COMSOL [23] finite element models, with the overall goal being to find a general fit that could be used for any given ratio of radius over reduced area width (r/d) and slot spacing (unreduced area) width over reduced area width (D/d). Initial attempts used polynomial forms similar to Roark, but power law curves were found to fit the data far better than pure polynomial forms. Various forms of the power law fit were tested, each with different dependencies upon D/d , until settling on the following bivariate form.

$$K_t = \left(A \left(\frac{D}{d} \right) + B \right) \left(\frac{r}{d} \right)^\alpha \tag{2.2}$$

The coefficients A and B , as well as the exponential α , were determined using a least-squares fit and resulted in the final form shown in Eq. (2.3), with an overall residual squared of $R^2=0.914$. The residuals for each case, along with the comparable univariate curve fits for each individual line, are contained within Table 6.2 of the Appendix.

$$K_t = \left(3.7962 \left(\frac{D}{d} \right) - 3.2394 \right) \left(\frac{r}{d} \right)^{-0.2905} \tag{2.3}$$

The accuracy of the bivariate fit is of the same order of magnitude as the univariate fits for each parameter varied with the other fixed, while also allowing for more convenient estimation of intermediate points. Fig. 2.5 shows how the trends for each D/d compared to the data themselves.

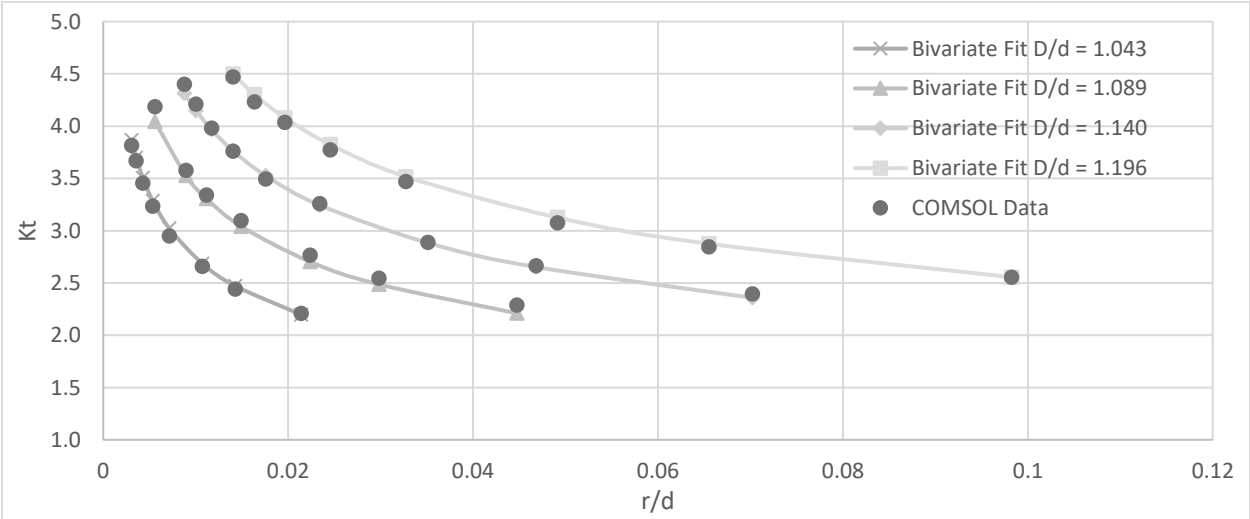


Figure 2.5 COMSOL FEM Data Compared Against Bivariate Fit for each D/d ratio of slot spacing to reduced width Data. Most cases track fairly well, with only one case slightly overestimating values and one case slightly underestimating values.

After validating the accuracy of the bivariate curve fit, additional data was included for a longer slot of 15 millimeters. However, the bivariate form in Eq. (2.3) no longer predicted the concentration factors accurately. Instead, with the exception of $D/d = 1.089$, the R^2 value of each data set dropped below 0.8. As a result, a new form the

Concentration Factor Curve Fit

equation was derived from the 15-millimeter slot data for comparison. Its data regression led to the variables A , B , and α changing significantly as follows.

$$K_t = \left(4.354 \left(\frac{D}{d} \right) - 3.841 \right) \left(\frac{r}{d} \right)^{-0.2993} \quad (2.4)$$

Similarly, when Eq. (2.4) was used, it accurately predicted the concentration factors for its original data set, but failed to produce accurate results, as shown in Table 2.1.

Table 2.1 Bivariate Solution Weakness. When either equation is applied to slots outside of its original data set, it loses accuracy.

	10 mm Slots		15 mm Slots	
	Equation 3 R ²	Equation 4 R ²	Equation 3 R ²	Equation 4 R ²
$D/d = 1.043$	0.9834	0.9952	0.9216	0.9680
$D/d = 1.089$	0.9598	0.6062	0.9547	0.9381
$D/d = 1.140$	0.9860	0.2491	0.5576	0.9788
$D/d = 1.200$	0.9843	0.5251	0.0096	0.9616
Total	0.9135	-0.6243	-0.5565	0.8465

As mentioned in Roark's text, the stress concentration exponentially decays towards unity as it moves away from the corner/hole [20]. The proximity of the nearby slots, which changed as a result of the lengthwise extension or contraction, likely explains the change in the equation's coefficient values, as well as the decrease in accuracy when applied to slots of different lengths. As a result, a third term was added to account for the influence of additional nearby slots and their corresponding stress concentrations. Additionally, the terms were now normalized by the unreduced area (D) to allow for consistent scaling within the equation as the slot sizes and spacings were varied.

Multiple forms of the trivariate form were tested, with different inclusions of a new distance term (s) corresponding to the distance between the nearest corners. Various forms were tested, including adding the new term in a manner similar to the D/d term in Eq. (2.2), as well as multiplying or dividing Eq. (2.2) by the distance term. The best result came from the form shown in Eq. (2.5), where the middle term facilitates recovery of the original bivariate form as the distance between nearest corners approaches infinity.

$$K_t = \left(A * \left(\frac{d}{D} \right) + C \right) \left(1 + \frac{B}{\left(\frac{s}{D} \right)} \right) \left(\frac{r}{D} \right)^\alpha \quad (2.5)$$

Just as with the bivariate form, the coefficients for the trivariate curve fit were determined using a least-square fit, but now for the entire data set of both 10 millimeters and 15 millimeters long slots. The resulting Eq. (2.6) maintained a residual squared greater than 0.9 for all cases, with comparisons against the bivariate and univariate solutions for each dataset shown within Table A.3 of the Appendix A.

$$K_t = \left(-4.262 \left(\frac{d}{D}\right) + 4.712\right) \left(1 + \frac{0.0308}{\frac{s}{D}}\right) \left(\frac{r}{D}\right)^{-0.295} \tag{2.6}$$

Figs. 2.6 and 2.7 show how the trivariate and bivariate curves compare against the 10 millimeters and 15 millimeters data points from the COMSOL models, respectively.

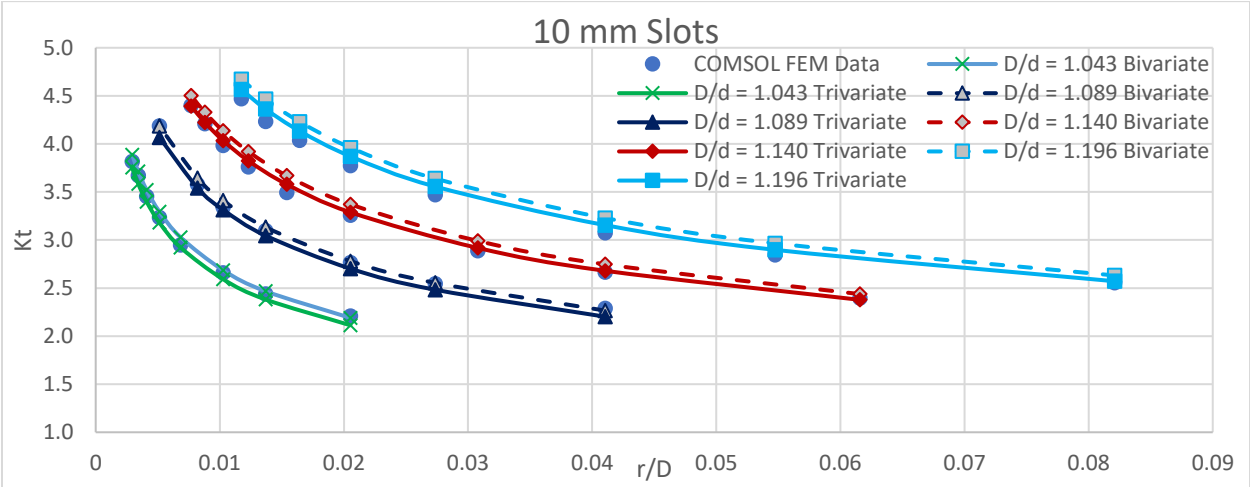


Figure 2.6 Bivariate and Trivariate fits for 10 mm slots. Both data sets track the two inner curves well, while the trivariate appears to be the more accurate of the two cases.

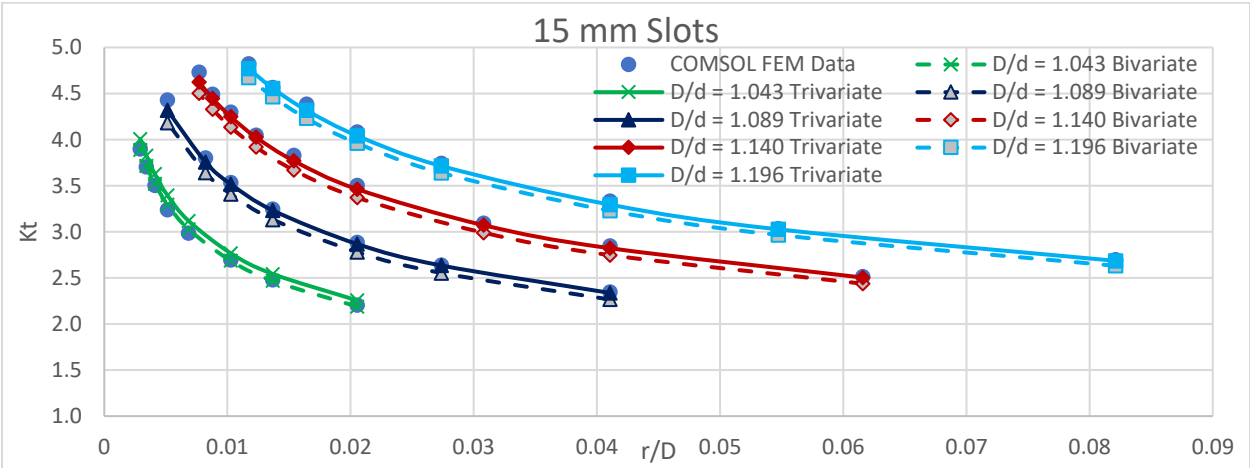


Figure 2.7 Bivariate and Trivariate fits for 15 mm slots. As with the 10 mm length slots, the trivariate form appears to track better, but now appear to overestimate the lowest D/d = 1.043 line.

With the finalized trivariate form, a direct comparison to the nearest Roark form can be made. However, Roark’s Type 5 Irregularity is not considered valid if the ratio between the unreduced area distance, L , and the slot separation distance, D , is too low, as governed by the inequality:

$$\frac{L}{D} \geq \frac{3}{\left[\frac{r}{D - 2h}\right]^{\frac{1}{4}}} \tag{2.7}$$

Multifidelity Design Application of Bivariate Fit

Due to the slots within a waveguide being so close to one another, the equivalent L/D ratio falls below the threshold. Consequently, the residual for the Roark approximation was poor, varying between negative values of -0.089 and -11.36 , whereas the trivariate fit had residuals varying between 0.90 and 0.99 . The comparison is easier to see in Figs. A.1 and A.2 of the Appendix A, which demonstrates how the Roark fit becomes less and less accurate as the D/d ratio increases. The bivariate and trivariate curve fits were also compared to *Peterson's Stress Concentration Factors*, which also fared poorly, because it too was found to be below its viability threshold [24].

3. Multifidelity Design Application of Bivariate Fit

With the bivariate and trivariate curve fit coefficients determined, the corner stresses can now be accounted for within an optimization procedure without requiring a finely re-meshed finite element model for each candidate geometry. Here the waveguide optimization focuses on varying the slot width and centerline spacing, since the slot length is dictated by the target frequency and the lengthwise spacing by the desired radiation pattern. These two factors combine to determine the unreduced area width (D) and reduced area width (d). Fillet radius was added as the final variable. The centerline spacing was constrained to ensure that slots do not overlap on a single waveguide. This leaves the slot width and radius as the driving forces for the optimization that accounts for these corner concentrations.

In practice, the embedded waveguides would be installed as panels in the aircraft's wing or fuselage skin, placing them between ribs on each end. These panels would therefore be subject to in-plane compressive or tensile loads, depending upon whether they are in the top or bottom skins, respectively. These loads are applied uniformly across the end areas of 3D models, or as an edge load in the simplified plate models, simulating skin compression as the wing bends due to flight loads. To realize practical design loads and stress limits for this example, estimated flight loads of the X-47B were used to test designs. The loads were calculated based upon the listed maximum takeoff gross weight (MTOGW) of 44,000 lb. and an assumed lift profile varying from linear on the narrowing inboard section to elliptical along the constant span outer section. The resulting moment distribution was consistent with the typical root-wing bending moment (RWBM) of about 10×10^6 lb.-in for military class aircraft of this size. Next, based on the geometry of the X-47B wing [25], the RWBM was used to estimate a representative compressive load in the top skin panel. A 3g load factor and a 1.5 factor of safety required that the designs withstand at least 19,400 Newtons (4,340 lb.) of load applied to the embedded antenna panel.

A mass minimization was conducted in MATLAB with a coarse FEM that neglected the slot fillet, using instead the bivariate fit to account for stress concentration, which was then verified in a higher fidelity filleted FEM in

COMSOL Multiphysics. Within the optimization code, slot width (d_1), slot centerline-offset (d_3), waveguide height (d_6), fillet radius (r), and waveguide material thickness were all allowed to vary. Several geometric constraints were added to ensure the slots remained within the perimeter of the waveguide upper surface, while an additional constraint ensured that the fillet radius could not exceed half of the slot width, in addition to its side constraints. Another constraint ensured that the mass had to be less than the nominal mass. The final constraint ensured the stress at the corner of the slot did not exceed the yield stress of the copper given in Table 2.2. The corner stress was calculated by multiplying the concentration factor from the geometry against the stress in the unreduced area, with the applied load being calculated as the buckling load for the given waveguide geometry. The buckling load was calculated through Euler-column buckling modified by a Timoshenko shear reduction factor:

$$P_{cr} = \frac{P_e}{1 + \frac{\eta P_e}{AG}} \quad (2.8)$$

In Eq. (2.8), P_e represents the lowest eigenvalue of the standard beam buckling problem, A is the end area of the beam, G is the shear modulus of the beam's material, and η represents the Timoshenko shear coefficient, which is typically taken as 5/6 [26].

The optimization was conducted using a MATLAB implementation [27] of Sequential Quadratic Programming (SQP) [28] in conjunction with the bivariate form in Eq. (2.4), with the resulting design variable values shown in Table 2.2. Fig. 2.9 shows the difference between the meshing of the high-fidelity COMSOL model and the low-fidelity MATLAB model. The waveguide height and thickness were both taken to their minimum values, while the slot width increased to its maximum value. With three of the five values at their extremes, the slot offset only varied slightly from its initial value at the minimum, and the fillet radius was decreased to the minimum value necessary to meet the stress constraint. The first tests conducted validated the original bivariate version of the curve fit, showing its viability, before implementing the additional modifications for the trivariate fit listed in the previous section. The resulting design decreased the waveguide's mass by 37.4 percent, from approximately 0.0867 kg to 0.0542 kg, while the waveguide's buckling load decreased by 58.9 percent, from approximately 13,700 Newtons to 5,630 Newtons.

Multifidelity Design Application of Bivariate Fit

Table 2.2 SQP Optimization Results for a Copper Waveguide. The slots were expanded and the height and thickness reduced with buckling was not constrained, while constraining the buckling resulted in smaller slots and increased fillet radii.

Variable	Nominal (mm)	Optimized without P_{cr} constraint (mm)	Optimized with P_{cr} constraint (mm)
d_1	2.00	3.00	1.30
d_3	2.00	2.10	2.20
d_6	10.16	8.00	9.30
r	0.200	0.900	0.630
t_c	0.750	0.500	0.710
Objective & Constraint Values			
Mass (kg)	0.0867	0.0542	0.0810
Buckling Load (N)	13,700	5,630	10,900
Max Stress (MPa)	1,055	544.9	550.0

The results indicate that the optimizer was removing as much mass as possible, with the reduction in height also having the added effect of reducing the applied buckling load and, as a result, the compressive stress in the waveguide. To combat this, a constraint was added to ensure the buckling load of the waveguide does not decrease beyond 80 percent of the original buckling load. The final column of Table 2.2 shows how this additional constraint resulted in a significant change in the optimized design. In order to meet the buckling constraint, the slot width was reduced, rather than increased, to provide additional stability. The fillet radius was limited by the constraint dictating that it cannot exceed half of the slot width, while a larger final thickness sustained the additional load. The resulting optimized design resulted in a mass decrease of 6.57 percent, from 0.0867 kg to 0.0810 kg, and the buckling load abiding by the 80 percent constraint, finalizing at 10,900 Newtons.

A 12-slot waveguide model, with fillet radii one-tenth of the slot's width, was created in COMSOL to verify these designs, as shown in Fig. 2.8A. According to the approximate model, the copper waveguide should have a buckling load of 13,700 Newtons and a concentration factor of 3.65 between the von Mises stress at the corner and the nominal compressive stress caused by a unit load. The COMSOL model for these nominal values determined that the buckling load was 13,200 Newtons, a difference of only 3.65 percent. Additionally, stress patterns in Fig. 2.10A result in a stress concentration factor of approximately 3.22 at the corner. While the prediction is in error relative to the FEM value by approximately 11.8 percent, it is worth noting that it is an overestimate the concentration factor, resulting in more conservative designs that are likely stronger than required. The discrepancy likely stems from the design's lower r/D value, placing it in the region where the curve becomes more exponential and tends to overestimate concentration factor values.

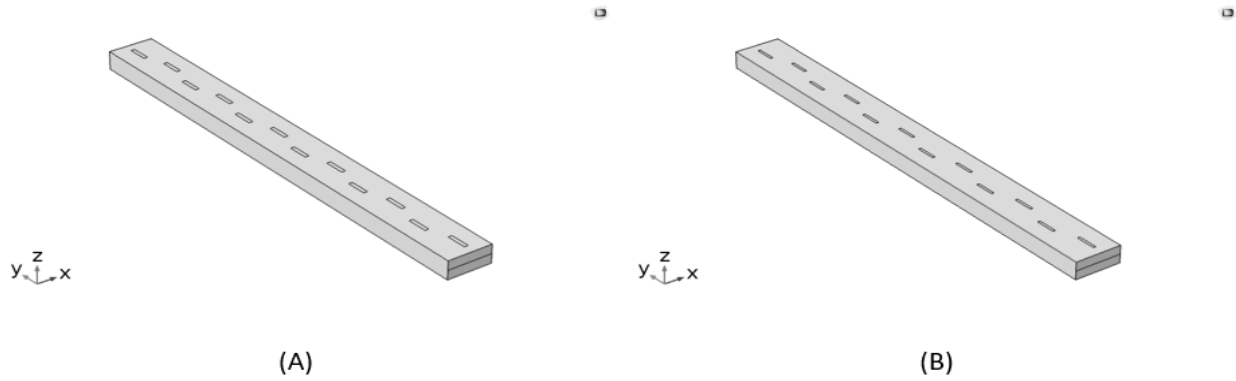


Figure 2.8 Waveguide Configurations for A) Nominal Values and B) Optimized Values. The nominal design shows the larger initial slots and their squarer shape, while the optimized design shows the narrowed and rounded slots.



Figure 2.9 A) COMSOL Mesh Compared to B) Low-fidelity Design Model Mesh. The COMSOL mesh added many elements to fully capture the corner effects, while the fit allowed for the low-fidelity mesh to account for the corner stresses.

After verifying the accuracy of the curve-fit estimate of stress concentration with the nominal design, the optimized design was modeled next in COMSOL, as shown within Fig. 2.8B. The model chosen was the second result in Table 2.2, with the additional buckling constraint was added. The COMSOL model predicted buckling would occur at 10,900 Newtons, consistent with the constraint’s estimate of 10,900 Newtons. The estimate predicted a corner stress concentration factor was 2.21, which is in line with the stress patterns within Fig. 2.10B, which correspond to a concentration factor of 2.22. While slightly less than the COMSOL model’s, the estimate is still within 0.48 percent of the actual value. The bivariate fit was used in this case due to the slot lengths being fixed during the analysis. The weakness for varying slot lengths appeared afterwards, when implemented in the larger optimization described next in Section IV.

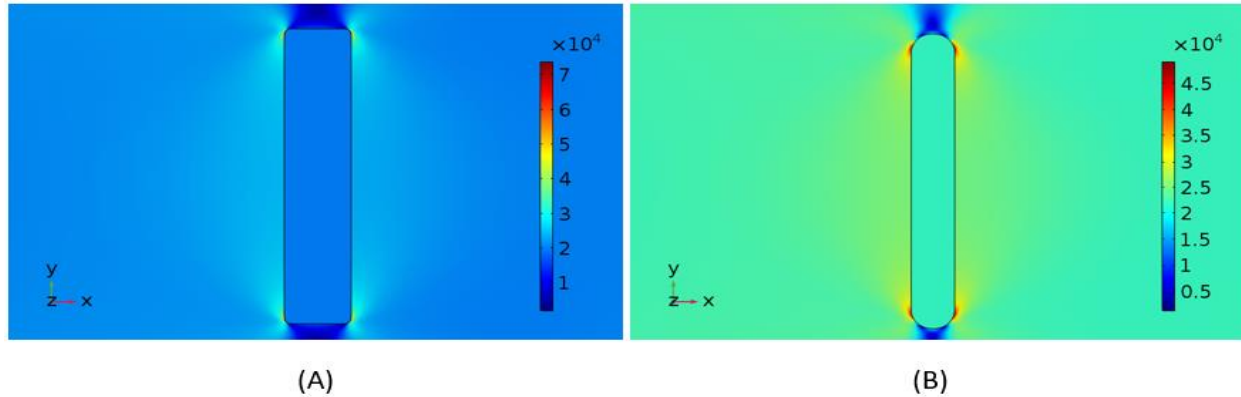


Figure 2.10 Stress Patterns for A) Nominal Slot Dimensions and B) Optimized Slot Dimensions. The nominal design shows higher stress concentrations at the corners, while the optimized form has reduced their magnitudes to a level closer to the rest of the waveguide.

4. Multifidelity Design Application of Trivariate Fit with Composite Materials

With the curve fit’s viability confirmed for the initial optimization for fixed slot length, the bivariate form was then implemented within an optimization procedure to simulate its intended use. However, problems with inaccuracy for varying slot lengths dictated a different curve fit for 15 mm slots. As an alternative, the trivariate form was developed and implemented within a multi-objective optimization for varying slot length. As shown in Fig. 2.3, the copper waveguide sits at the center of the design, with a supporting fiberglass sleeve around it, as well as an outer fiberglass face sheet covering the slotted waveguide and an inner graphite epoxy face sheet on the opposite side. Fiberglass was chosen due to its stiffness, but also because it is electromagnetically transparent and will allow radar transmission to be unhindered. Graphite epoxy was chosen for the inner face sheet due to its high stiffness and strength to mass ratio, allowing the design to increase in stiffness and strength at a reduced mass penalty. However, graphite epoxy is not electromagnetically transparent, resulting in it only being used on the inner face sheet where the impact on the electromagnetic performance is not a factor. While these supporting materials are intended to bear a large portion of the load, proper modeling of the concentration factors around the slot corners allows the optimization to load the copper without ignoring the local yielding that would occur as a result.

The optimization performed with a range of weightings for minimizing the mass and maximizing the buckling load, while subject to constraints ensuring the designs are both physically feasible and do not result in failure of any of the materials. However, the inclusion of the concentration factor showed that the copper cannot support loading from the outset without either the mass or buckling load deteriorating. When the copper was loaded, designs resulted that were drastically heavier and weaker than an unloaded copper waveguide. With all of these factors combined,

loading the copper from the start appears to be a significant restriction on the design process. As a result, the copper was left as an unloaded insert free to slide within the supporting fiberglass sleeve. The resulting designs, such as the one within Table 2.3, reduced the copper thickness to save on mass, which then allows for the graphite epoxy and fiberglass thicknesses to be increased to strengthen the material without violating the mass constraint.

Table 2.3 Optimization of a Full Waveguide Design. The reduction in mass from decreasing the copper thickness offsets the increase due to increasing the thickness of the supporting materials, while also increasing the overall buckling load.

Variable	Nominal (mm)	Optimized (mm)
d_1	2.00	3.00
d_3	2.00	2.50
d_6	10.16	12.0
r	0.500	0.664
t_c	0.750	0.125
t_f	0.750	1.10
t_g	0.750	2.00
Objective & Constraint Values		
Total Mass (kg)	0.162	0.108
Copper Mass (kg)	0.109	0.0183
Buckling Load (N)	36,680	100,300
Max Fiberglass Stress (MPa)	-	421.9
Max Graphite Epoxy Stress (MPa)	-	999.5
Max Copper Stress (MPa)	-	0

5. Conclusion

To properly analyze a loaded waveguide, it is important that the stress concentrations at the slot corners are properly modeled. In contrast to the initial polynomial forms used, analysis showed that a power law better fit the data, allowing both the initial bivariate and trivariate forms to accurately model the corner stresses using a coarser mesh. As a result, slotted waveguides can be analyzed with a simplified mesh, rather than the more complex meshes currently required to properly capture the curvature at the slot corners, or even simply with a hand calculation of the unreduced area's stress. The final trivariate form's slot-corner-distance term allowed the approximation to be used across multiple slot lengths, allowing for use within design optimization. The initial designs showed that the copper cannot be fully loaded from the start without a significant mass and buckling penalty.

Chapter 3 Electromagnetic Performance of Structurally Embedded Waveguides

1. Introduction

Since the development of radar in the early 20th century, the technology has been refined and developed over the decades. Beginning initially as large ground-based stations, the designs were refined so that they could be used by ships and even aircraft, with applications ranging from simple weather radars, to target acquisition systems in modern military aircraft and weaponry. Most of these systems saw dedicated internal systems such as nose mounted dishes for weather radars as in Fig. 1.1A, but designs have also been examined that aimed to integrate the radiating elements into the structure of the aircraft itself. One of these relevant forms are the Conformal Load-Bearing Antenna Structures (CLAS) examined by Paul Callus [3]. These designs were composed of a series of conductive antennas embedded within supporting structures that diverted most of the loading around the antenna itself. However, these concepts were difficult to integrate into existing aircraft [3].

A subsequent study by Kim and Canfield further developed the concept for Slotted Waveguides Antenna Stiffed Structures (SWASS). These designs integrated the slot-array antennas into the stiffeners of the aircraft's skin, and then shifted to integrating the slotted waveguides into the skin of the aircraft itself. Among the multiple skin panel configurations, the design most relevant to this paper is the one that Kim and Canfield denoted as Concept 4, shown in Fig. 3.1A, which is composed of an inner metallic waveguide surrounded by an electromagnetically transparent sleeve of fiberglass, and sandwiched between a fiberglass outer mold line and a graphite-epoxy inner mold line [22]. The dimensions most relevant to the analyses conducted later in the paper are those of the metallic waveguide itself, shown in Fig. 3.2C and defined in Table 3.1.

Table 3.1 Waveguide Dimensions.

Waveguide Dimension	Representative
Slot Width	$d1$
Slot Length	$d2$
Slot Offset (mid-slot to mid-line)	$d3$
Slot Spacing	$d4$
Waveguide Inner Width	$d5$
Waveguide Inner Height	$d6$
Waveguide Length	L
Slot Corner Fillet Radius	r

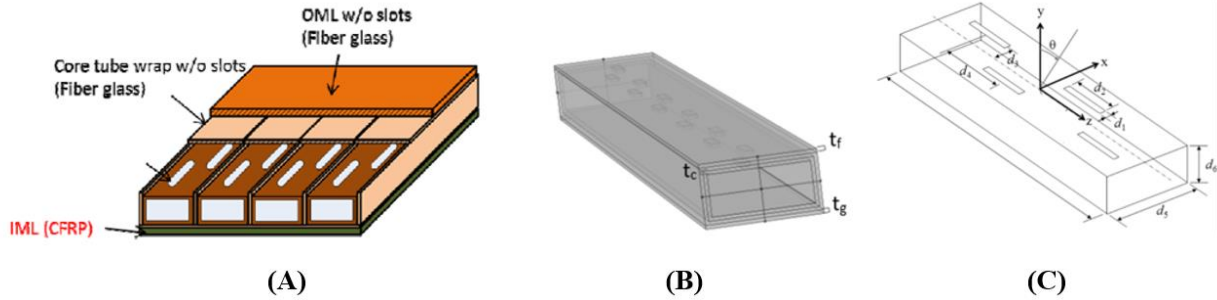


Figure 3.1 Waveguide Concept and Components. A SWASS panel is composed of multiple singular waveguides consisting of an inner metallic core, surrounded by fiberglass and CFRP supporting material.

Brooks and Canfield further refined this concept by developing multifidelity models to account for the structural requirements of the designs while imposing electromagnetic performance requirements [29].

Here, multiple Pareto optimal designs are created through an optimization process based upon the structural and electromagnetic performance requirements. Using modeling results from the HPCMP's CREATE-RF™ SENTRI [30] program, the effects of variations in the design variables are quantified, and the anticipated electromagnetic performance validated. Frequency sweeps validate that the peak performance of each design occurs at the design frequency and have not been shifted by structural changes during the optimization process. Additionally, analyzing the far field gain patterns verify that properly phased arrays will radiate with sufficient power and directivity to meet the design requirements.

2. Model Verification

Throughout the design process, the dimensions of the waveguide itself were governed by the general rules for waveguide antenna design. Within these equations, the three important wavelengths are governed by

$$\lambda_0 = \frac{c}{f} \quad (3.1)$$

$$\lambda_c = 2a \quad (3.2)$$

$$\lambda_g = \sqrt{\frac{1}{\left(\frac{1}{\lambda_0}\right)^2 - \left(\frac{1}{\lambda_c}\right)^2}} \quad (3.3)$$

where f is the target frequency measuring the number of oscillations per second in the signal, c is the speed of light, a is the inner waveguide width d_5 , λ_0 is the free space wavelength measuring the distance between peaks in the signal, λ_c is the cutoff wavelength that dictates the smallest frequency that the waveguide can transmit, and λ_g is the

Model Verification

guided wavelength that governs how the signal propagates along the waveguide's length [4]. Each of these wavelengths are integral in the sizing of the waveguides, with half the free space wavelength dictating the length of each slot d_2 for proper resonance, the cutoff wavelength dictating the minimum frequency which can be transmitted along the waveguide shown in Fig. 3.2A, and half the guided wavelength dictating the optimal longitudinal spacing d_4 of the slots along each individual waveguide such that they align with the peaks and troughs of the guided wavelength signal shown in Fig. 3.2B. In accordance with the simplification of a slotted waveguide as an analog for a transmission line, each slot is spaced $\lambda_g/2$ apart and alternate their displacement relative to the centerline so that successive slots remain in phase with one another. The first and final slots are each $\lambda_g/4$ from their respective ends, as a short circuit of that length in a transmission line is equivalent to an open circuit [4] [31].

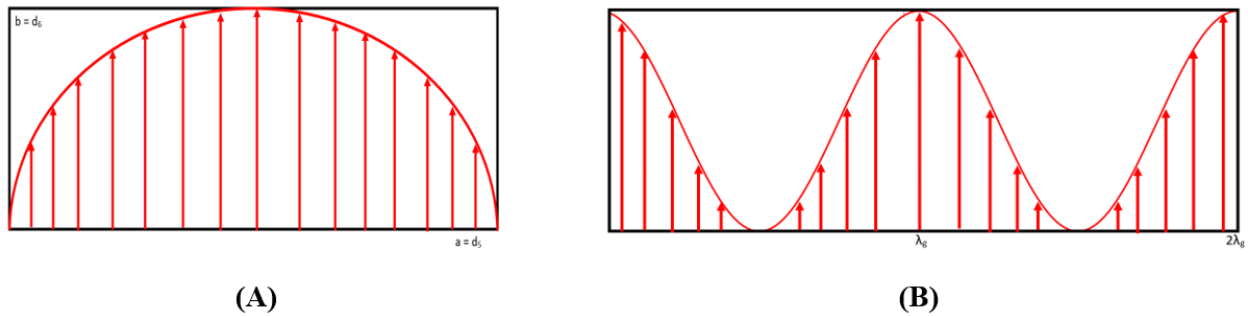


Figure 3.2 A) Cross-Sectional Profile and B) Lengthwise Profile. The signal propagates such that the electric field is maximum in the center and 0 at the edges, and also oscillates in accordance with the guided wavelength.

A prior study by Ha and Canfield confirmed the importance of the slot length, slot longitudinal spacing, and inner waveguide width, as they had the largest impacts on the waveguide's radiation pattern [17]. As a result, these three dimensions were left constant in this study to minimize the changes to the radiation pattern.

The remaining design variables that were allowed to vary during the design process were the slot width d_1 , slot centerline spacing d_3 , waveguide height d_6 , and the thicknesses of the various materials shown in Fig. 2C. The centerline spacing that gives the best reflection coefficient is given by [32] [33]

$$d_{3t} = \frac{a}{\pi} \sqrt{\sin^{-1} \left(\frac{1}{N \cdot G} \right)} \quad (3.4)$$

where

$$G = 2.09 \cdot \frac{a}{b} \cdot \frac{\lambda_g}{\lambda_0} \cdot \left[\cos \left(0.464\pi \cdot \frac{\lambda_0}{\lambda_g} \right) - \cos(0.464\pi) \right]^2 \quad (3.5)$$

In these equations, $b = d_6$ corresponds to the waveguide height, N to the number of slots within each waveguide, and d_{3t} denotes the optimal, or target, uniform centerline spacing. The coefficients in the equation are based upon the resonance lengths compiled with the studies conducted by Elliott and Kurtz [34]. The prior research presented in Ha and Canfield [17] showed that, while increasing the centerline spacing resulted in slight increases in the peak gain, when the slot length is matched to the transmission frequency, the increases are minimal beyond these target values. Similar results were also shown when looking at the data on the slot width and the waveguide height.

One difference between theory and the COMSOL and CREATE-RF™ SENTRi models is the magnitude of the radiation patterns. According to theory, the gain of a slotted waveguide antenna should increase by roughly 3 decibels (dB) each time the number of slots N is doubled [35], in accordance with

$$G_{peak} = 10 \cdot \text{Log}(N) \tag{3.6}$$

However, the data points collected through CREATE-RF™ SENTRi models and prior research [10], as in Fig. 3.3, do not follow this pattern. To account for the gain being higher than the theory’s prediction, a fit was developed to better estimate the model’s performance

$$G_{peak} = 11.19 \text{Log}(N) + 4.65 \tag{3.7}$$

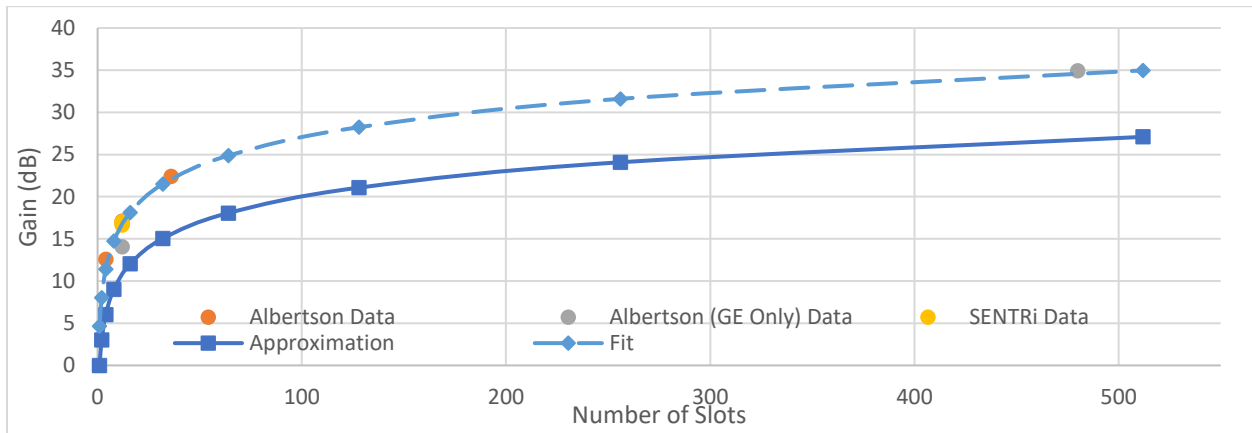


Figure 3.3 Model Gain Data. The models displayed larger maximum gains than the prediction, necessitating a fit.

Due to the data from both new models and those in prior studies [10] exceeding the theoretical values, the curve was created to better predict the modelling results, but is not used in the optimization due to it being independent of the chosen design variables

3. Optimized Designs

Various Pareto optimal designs were developed over the course of prior optimization procedures [36], which were required to meet electromagnetic constraints. The optimization primarily focused on a combination of minimizing the total mass of a design M_{tot} and maximizing the buckling load of the design P_{cr}

$$\min f = \eta \cdot f_1 + (1 - \eta) \cdot f_2 \quad (3.8)$$

$$f_1 = \frac{P_{cr0} - P_{cr}}{P_{cr0}} \quad (3.9)$$

$$f_2 = \frac{M_{tot} - M_{tot0}}{M_{tot0}} \quad (3.10)$$

where P_{cr0} represents the minimum acceptable buckling load and M_{tot0} represents the maximum acceptable total mass. An initial Pareto front is generated through weighted sums method, which varies the weighting factor η between 0 and 1, in increments of 0.02, to find several points along the front. The front was then filled in using the epsilon constraint method, which chooses one of the objectives in Eq. (3.8), while constraining the other to a parametrically varying value, ϵ

$$\min f_1 \text{ s.t. } f_2 \leq \epsilon \quad (3.11)$$

$$\min f_2 \text{ s.t. } f_1 \leq \epsilon \quad (3.12)$$

Depending upon which value is being optimized, the other is converted into a constraint where P_{cr0} or M_{tot0} in the numerator are replaced by a target value along the suspected Pareto front based upon the initial results from weighted sums [37]. Throughout the optimization, a series of 24 constraints were employed based upon the designs' dimensions, stress profile, electromagnetic performance, and other design constraints. These constraints, given in Tables 4.3 to 4.7, are formulated such that they are only satisfied when non-positive, $g_j \leq 0, j = 1, \dots, 24$. Those most relevant to the electromagnetic performance are presented in Tables 3.2 and 3.3 but maintain their numbering consistent with the original publication.

Table 3.2 Geometric Constraints.

$$g_1 = d_6 - d_5$$

$$g_2 = d_1 + 2 * (d_2 + t_{cs}) - d_5$$

$$g_3 = 2 * d_1 - d_5$$

$$g_4 = d_2 - d_4$$

$$g_5 = d_2 + (n_{slots} - 1) * d_4 - L_c$$

$$g_8 = r - \frac{d_1}{2}$$

Table 3.2 details the constraints that governed the physical dimensions with g_1 ensuring the waveguide is wider than it is tall. Constraint g_2 ensures the waveguide's slots are not cutting into the side walls, while g_3 ensures that two slots are not wider than the central void of the waveguide. Constraint g_4 ensures that the slots are spaced apart such that they do not overlap lengthwise, while g_5 ensures that the waveguides do not extend beyond the total length of the copper waveguide L_c . Finally, constraint g_8 ensures that the fillets on the corners are no larger than half the slot width, so as to avoid points at the center of each slot.

Table 3.3 Electromagnetic Constraints.

$$g_{17} = \frac{d_{3t} - d_3}{d_{3t}} - 0.1$$

$$g_{18} = \frac{d_3 - d_{3t}}{d_{3t}} - 0.1$$

$$g_{19} = \frac{\frac{\lambda_g}{2} - d_4}{d_4} - 0.1$$

$$g_{20} = \frac{d_4 - \frac{\lambda_g}{2}}{d_4} - 0.1$$

Table 3.3 details the constraints related specifically to Eq. (3.3) and Eq. (3.4). Constraints g_{17} and g_{18} together ensured that the slot spacing from centerline was within ten percent of the optimal value calculated in Eq. (3.3). Constraints g_{19} and g_{20} ensured that the slots were spaced within 10 percent of the calculated guided wavelength value from Eq. (4). In both cases, a ten-percent limit was chosen because prior modelling showing that as one moved beyond ten percent from the target frequency's optimal values, performance began to quickly degrade, as will be shown later.

While the optimization could not directly analyze the electromagnetic performance, the governing equations in prior sections ensure that the resulting designs do not sacrifice the electromagnetic performance for better structural performance. Multiple designs were taken from along the Pareto front shown in Fig. 3.4 to demonstrate that the performance was consistent in each region of the Pareto front.

Optimized Designs

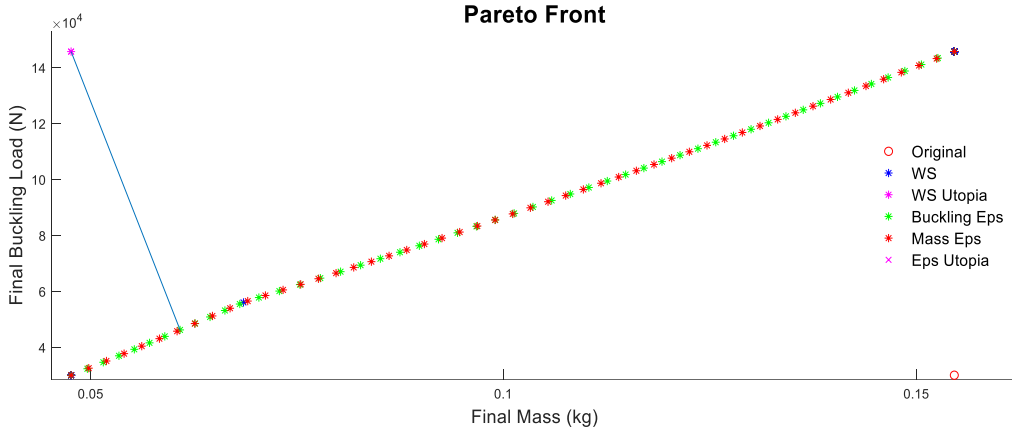


Figure 3.4 Optimized Pareto Front. Optimization balanced minimum mass and maximum buckling designs while imposing electromagnetic performance constraints.

Three designs were pulled from Pareto front, shown in Table 3.4, and analyzed to confirm that their electromagnetic performances were consistent.

Table 3.4 Design Dimensions.

Dimension	Nominal (mm)	Design 25 (mm)	Design 35 (mm)	Design 45 (mm)
d1	2	1.2	1.2	1.3
d2	15	15	15	15
d3	2	3.0	3.0	3.0
d4	20	19	19	19
d5	22.11	22.86	22.86	22.86
d6	9.41	12	12	12
t_c	0.75	0.3	0.189	0.144
t_{cs}	0.75	0.125	0.125	0.125
t_f	0.75	0.5	1.0	1.4
t_{fo}	0.75	2.0	2.0	2.0
t_{ga}	0.1875	0.95	0.95	0.95
t_{gn}	0.1875	0.0325	0.0325	0.0325
r	0	0.6	0.6	0.6
δ	0	1.4	1.5	1.6

In Table 3.4, the design numbers correspond to their locations along the Pareto front, which is composed of 51 points numbered from 1 as the minimum mass design in the bottom left, to 51 as the maximum buckling load design in the top right.

The thickness of the slotted surface of the copper waveguides is represented by t_c , while the thickness of the three unslotted surfaces are represented by t_{cs} . All the copper surfaces are treated as impenetrable electric conductors and use the listed copper conductance of 5.814×10^7 S/m. The fiberglass sleeve around the metallic waveguide is represented by t_f and the thickness of the fiberglass outer mold line is represented by t_{fo} . Fiberglass was chosen for both layers due to it being electromagnetically transparent and was denoted as electromagnetically transparent within the modelling. This choice in material allows the electromagnetic signals to propagate without interference.

While t_g in Fig. 3.2 represents the total thickness of the graphite-epoxy layer, a $[0\ 90]_s$ layup is employed, allowing each layer's thickness, t_{ga} and t_{gn} respectively, to be varied for greater control of the inner mold line's strength. Additionally, the material's position on the inner surface means that, while it does interfere with the radiation pattern of the waveguide slightly due to its characterization as electromagnetically impenetrable in the models, its effects are not considered detrimental because it is in the same direction as the underlying structures. Finally, r corresponds to the fillet radius on the corners of each slot and δ corresponds to an initial offset added during the course of the optimization procedure to avoid overloading the copper when each design is loaded.

Design 45 was used to study the effect of the fillets on the antenna gain for a set frequency, with triangular elements used to capture the curvature of fillets at the corners as in Fig. 3.5B. For all models, the waveguides are fed through a port at one end of the copper waveguide and a copper cap at the other end, which acts as a short to end the circuit of the waveguide.

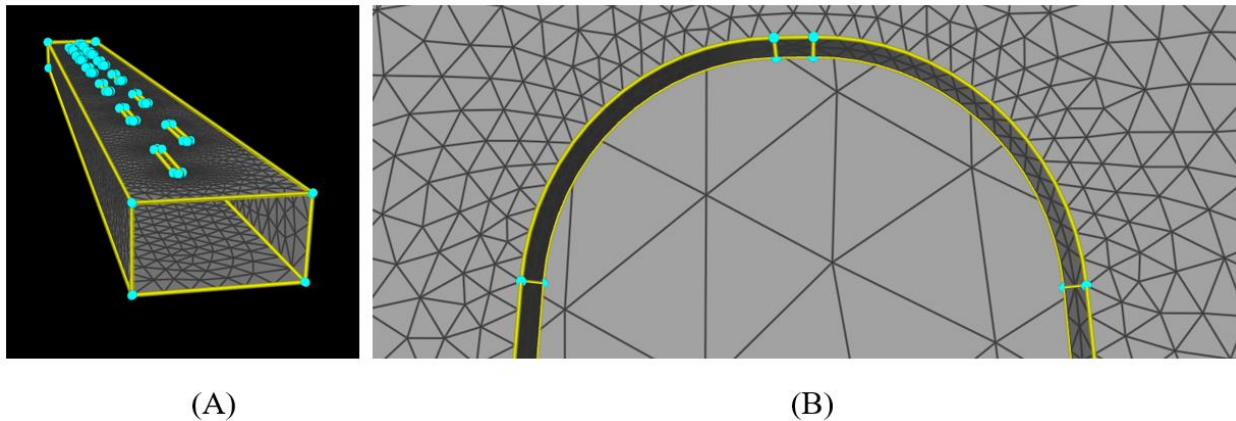


Figure 3.5 CREATE-RF™ SENTRi Fillet Meshing. The filleted slot models used dozens of triangular elements to properly capture the curve of the fillets at each corner.

Using a target frequency of 10 GHz and a unit input of 1 Watt, the design detailed in Table 3.4 was analyzed and shown to have a largely omnidirectional radiation pattern as in Fig. 3.6A. When the radius of the fillets on the corners of the slots is reduced to 0, this returns them to the traditional square representation. However, the square slot version of Design 45 in Fig. 3.5B shows an identical radiation pattern, with the two designs having peak gains within 0.01 dB of each other, as shown in Table 3.5. Due to the difference in peak gains being so small, and the patterns being identical the effects of fillet size appear to be minimal.

Optimized Designs

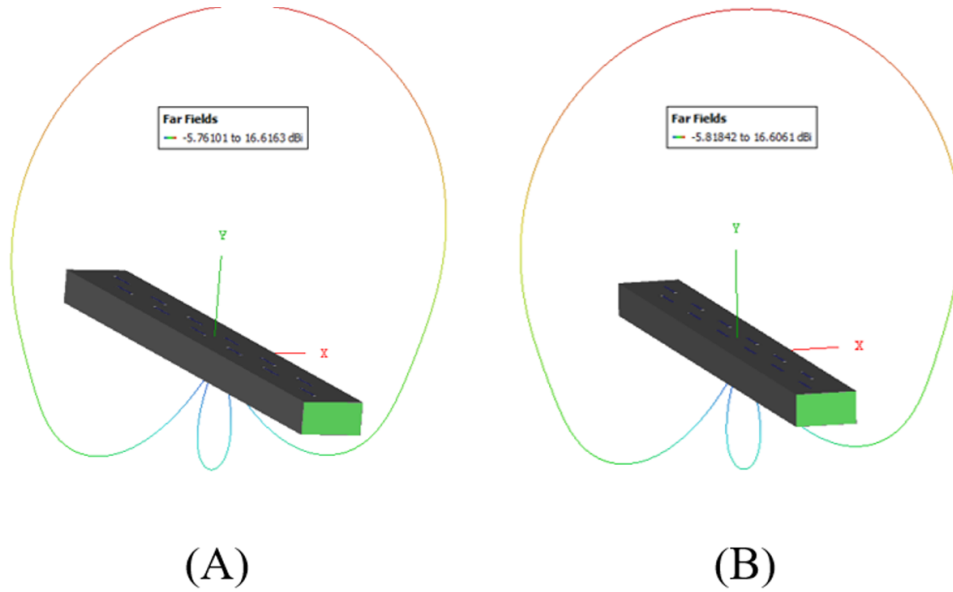


Figure 3.6 Design 45 with A) Filleted Slot Corners and B) Square Slots. The presence of fillets on the corners of the slots has a minimal effect on the gain's magnitude and has no observable effect on the radiation pattern [38] [30].

The next stage of the analysis involved analyzing Designs 25 and 35 at 10 GHz as well, shown in Fig. 3.7A and Fig. 3.7B respectively. Both designs showed the same type of radiation patterns as Design 45, while the peak frequency values are still very similar, as shown in Table 3.5. While the peaks are within 0.05 dB of one another, the identical radiation patterns indicate the designs are largely equivalent to one another. One possible explanation for the variation in peak gain is the variation in the top slotted surface thickness, however additional modelling would be needed to confirm this.

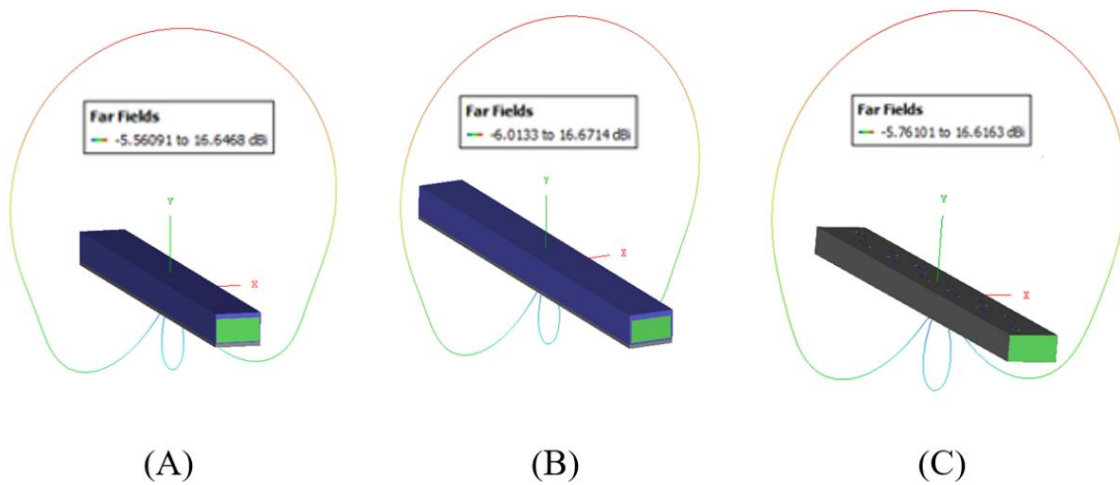


Figure 3.7 10 GHz Radiation Pattern for A) Design 25, B) Design 35, and C) Design 25. All three designs have identical radiation patterns, with small variations in peak gain [38] [30].

Table 3.5 10 GHz Peak Gain Data.

Design	Peak Gain at 10 GHz (dB)
25	16.65
35	16.67
45	16.62
45 w/ Square Slots	16.61

Another point to examine in future analyses is the effect of the dielectric properties of the supporting materials, as current models assume the sleeve and outer mold line are electromagnetically transparent, while fiberglass’s exact permeability depends upon its composition, with most being nearly transparent, but not perfectly. Full implementation would also depend upon the location of integration on the aircraft, however that would introduce additional variables beyond the scope of the current analysis.

The final analysis conducted was a frequency sweep of Designs 35 and 45 to confirm which frequencies resonate within the designs and confirm that the target frequency of 10 GHz is within that region. Using the models in CREATE-RF™ SENTRI, the excitation frequency was varied from 8 GHz to 11.25 GHz. In Fig. 3.8, both designs follow very similar variations, as the frequency was increased. These results were then compared against the results of the nominal design shown in Table 3.4. One important point for the nominal design, however, is that the waveguide width d_5 is defined from the center of the side walls, rather than the inner edge as would be done for the optimized designs.

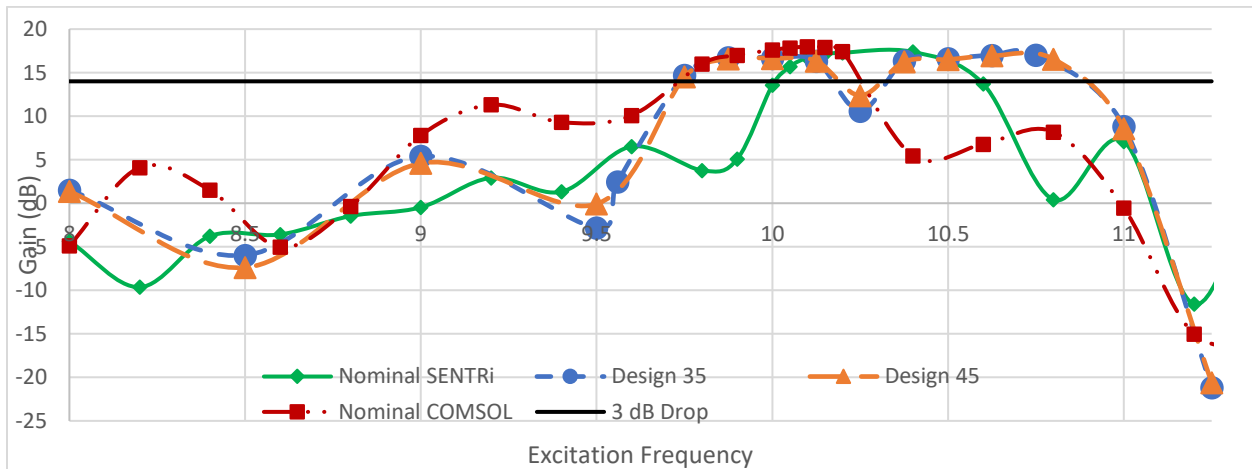


Figure 3.8 Frequency Sweep Results. Designs 35 and 45 have nearly identical regions of peak performance, and a wider operational range than the nominal design, but a lower peak gain.

Conclusions

Design 35 and design 45 had very similar gain patterns throughout the frequency sweep, with identical operational ranges as shown in Table 3.6. While there is a dip centered around 10.25 GHz, the optimized designs remain within 0.5 dB of their peak gain for a much larger range than the nominal design, which includes the target frequency of 10 GHz.

Table 3.6 Frequency Sweep Peak Data.

Design	Peak Gain (dB)	Peak Frequency (GHz)	Operational Range (GHz)
35	17.03	10.75	9.7–10.2 & 10.3–10.9
45	16.93	10.625	9.7–10.2 & 10.3–10.9
Nominal SENTRi	17.38	10.4	10.0–10.6
Nominal COMSOL	17.98	10.1	9.7–10.25

One potential explanation for the dip is that the slot sizes and spacing are not exactly matched. While the slots are 15 mm long to properly match the desired 10 GHz frequency, the exact longitudinal spacing according to half the guided wavelength from Eq. 3 would be 19.9 mm, rather than 19 mm. A similar phenomenon can be seen between the two nominal analyses. COMSOL Multiphysics [23] uses plate modeling that placed the EM surface at the centerline of plates, as opposed to the face plate models created by CREATE-FT Capstone [38] that placed the EM surfaces on the outer faces, which then were analyzed in CREATE-RFTM SENTRi [30]. As a result, the thicknesses cutting into the inner width and height only appear in the CREATE-RFTM SENTRi models, resulting in the peak shift similar to how the mismatched longitudinal spacing has caused shifts in the optimized designs. If the excitation frequency is instead increased to 10.25 GHz, the optimal spacing reduces to 19 mm, but the optimal slot length also decreases to 14.6 mm. Updating either of these two dimensions would likely result in improvements in the peak gain and remove the dip in the center of the operational range of Fig 3.8. This would also explain why the nominal designs have a much narrower operational range and only the plate model from COMSOL maintained a higher gain value for the desired frequency of 10 GHz.

4. Conclusions

Throughout prior structural optimization procedures, side constraints on geometric parameters were applied to maintain electromagnetic performance at satisfactory levels. The optimized designs showed that, while the introduction of fillets at the corners of the slots was very beneficial for the structural side, its impact on the electromagnetic performance was minimal. Three of the various designs, despite each coming from different points

along the optimized Pareto front, show very similar radiation patterns and magnitudes, verifying similar electromagnetic performance across the front, which justifies that decoupling these design variables from those that had the largest effect on the electromagnetic performance is a good approach. This is further confirmed by the frequency sweeps, which have matching operational ranges. Additionally, the designs maintain similar peak gains for the same frequencies and over a wider range than the nominal design. All these factors together show that the SWASS panels can meet their electromagnetic performance requirements while being optimized for better structural performance.

Chapter 4 Multifidelity Design of Structurally Embedded Waveguides

1. Introduction

When a structure is composed of multiple materials, the differing material properties often lead to different limiting stress values for each material. As a result, structures may see certain materials fail before others due to the uneven loading and the varying stiffness and strength properties for each material. For the structurally embedded, load-bearing slotted waveguides presented by Brooks and Canfield [21], it was shown that the copper waveguide could not withstand the compressive loads before buckling instability of the structure. Copper's high stiffness value results in it shouldering a sizable portion of the load, but the low yield stress means that it fails well before the supporting graphite-epoxy inner skin and fiberglass sleeve and outer skin. To alleviate this issue, one solution is to implement an initial gap between the copper waveguide and the end of the supporting materials, as shown in Fig. 4.1, allowing them to absorb a portion of the initial loading so that when the copper encounters the loading surface that it does not fail prematurely.

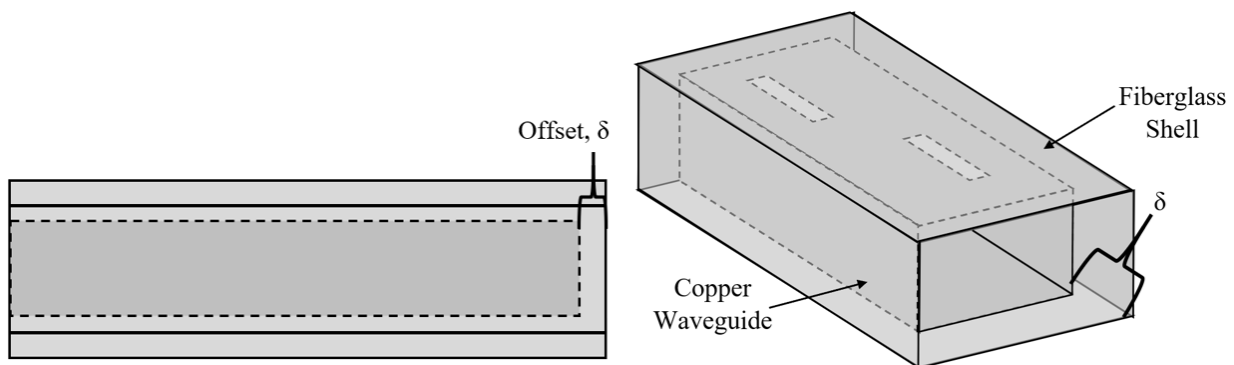


Figure 4.1 Offset Proposal. The supporting material will extend a distance δ beyond one end of the waveguide insert.

The slotted waveguide antenna stiffened structures (SWASS) being analyzed are based upon the fourth proposed design shown in Kim and Canfield [22] [17] for an aircraft skin panel, composed of a metallic inner waveguide surrounded by a fiberglass sleeve, fiberglass skin outer mold line (OML), and graphite epoxy skin of the aircraft panel inner mold line (IML) as in Fig. 4.2A. Each material has its own independent thickness shown in Fig. 4.2B, while the slot dimensions themselves use the same nomenclature as depicted in Fig. 4.2C.

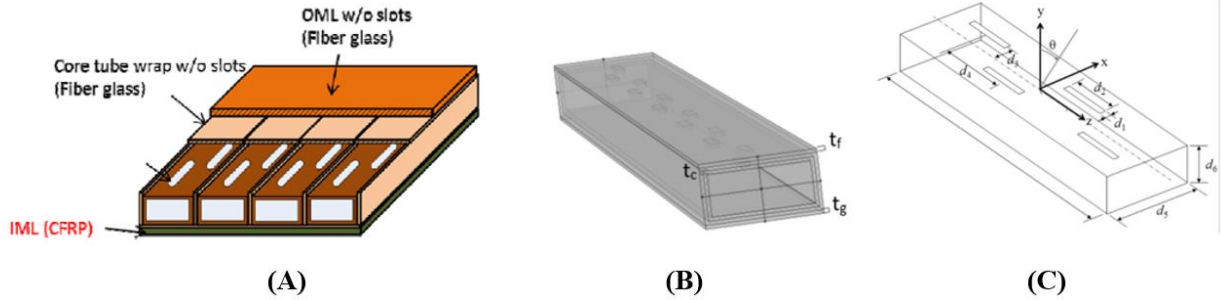


Figure 4.2 Waveguide Concept and Components. The SWASS panel is composed of the inner metallic waveguide, fiberglass sleeve and outer mold line, and CFRP inner mold line, with the material thicknesses and waveguide dimensions specified by its target function.

However, the modeling of the initial gap leads to issues when analyzing the structure's buckling characteristics. The standard eigenvalue finite element analysis relies upon a set of nodes placed along the structure's length, but since the copper does not experience initial loading prior to the gap's closing, it does not compress axially with these initial nodes. However, the copper does resist the transverse deflection, and thus cannot be ignored prior to the gap's closing.

The approach described here accounts for the initial gap in the eigenvalue analysis, thereby allowing low-fidelity models to properly model the gap's impact without the need for computationally expensive contact modelling for use within an optimization procedure.

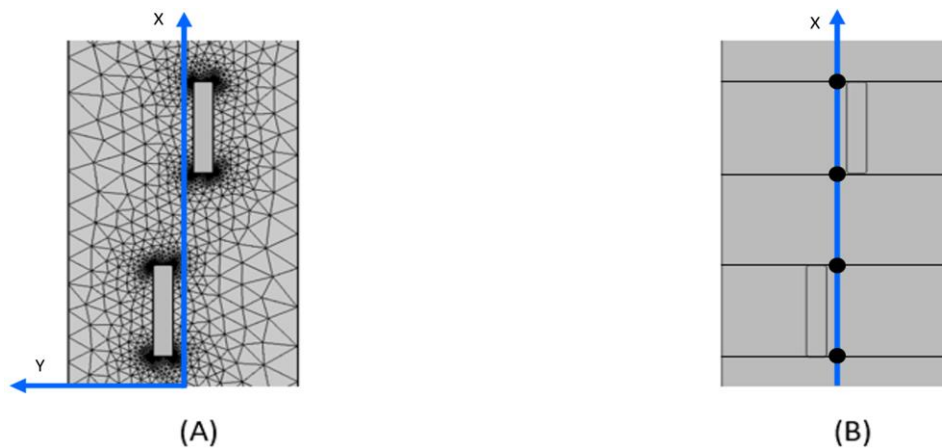


Figure 4.3 Model Fidelities. A) Finer mesh would require remeshing every time parameters are changed. B) A coarse mesh that can be easily updated within an optimization routine.

The low-fidelity model replaces the several thousand elements required for the higher-fidelity model with a series of two 1D element types: those with slots and those without, as shown in Fig. 4.3B. The stress concentrations created by the slot corners are accounted for using a fit developed by Brooks and Canfield [21], while the need for contact modeling is eliminated by the revised eigenanalysis detailed below. In this analysis, the nodal points on the supporting

Gap Modeling Using Prestress Terms

materials are chosen based upon the gap length and the initial stress required to close the gap. Doing so ensures that these initial nodes align with the corresponding nodes on the previously unloaded copper waveguide when the gap is closed. Using this choice of nodes allows for consistent post-gap displacement among all materials, while the pre-gap displacements are still accounted for, eliminating the need to perform load-displacement analyses for every design in a potential optimization procedure.

2. Gap Modeling Using Prestress Terms

Due to the presence of the offset, the standard eigenvalue problem must be updated to account for the change in stiffness that occurs when the gap is closed. Just as in the standard eigenvalue problem, total potential energy may be used to formulate the eigenanalysis.

$$\Pi^e = U + V \quad (4.1)$$

The main difference stems from the change to the strain energy (U) that now includes additional terms for initial strains (ϵ_0) or initial stresses (σ_0), although they typically would not be used at the same time [39].

$$U = \int \left(\frac{1}{2} \{\epsilon\}^T [E] \{\epsilon\} - \{\epsilon\}^T [E] \{\epsilon_0\} + \{\epsilon\}^T \{\sigma_0\} \right) dV \quad (4.2)$$

based upon the relationship

$$\{\sigma\} = [E](\{\epsilon\} - \{\epsilon_0\}) + \{\sigma_0\} \quad (4.3)$$

This method will account for the gap by using either the initial strain term to account for the displacement needed to close the gap due to an axial load and shorten it to the same length as the copper waveguide within, or by using the initial stress term to represent the load needed to close the gap. Similar methods have been used for analyzing the eigenfrequencies of structures under follower loading, as in Goyal and Kapania, but these looked at their effects on eigenfrequency analysis rather than eigenvalue buckling analyses [40].

In Eq. (4.1), V corresponds to the potential of the applied compressive load, equal to the applied load multiplied by the distance by which the beam is shortened [41].

$$V = P \int_0^L \epsilon_{xx} dx \quad (4.4)$$

For both strain energy and applied load potential terms, the axial strain for a beam can be expanded as [42].

$$\epsilon_x = \epsilon_{xx} + z\kappa_{xx} = \left(\frac{du}{dx} + \frac{1}{2} \left(\frac{dw}{dx} \right)^2 + \frac{1}{2} \left(\frac{du}{dx} \right)^2 \right) + z \left(\frac{d^2w}{dx^2} \right) \quad (4.5)$$

where ϵ_{xx} corresponds to the strain of the nodal/midplane and κ_{xx} corresponds to the curvature. Substituting Eqs. (4.2), (4.4), and (4.5) into Eq. (4.1) and assuming only the axial strains are substantial:

$$\Pi^e = \int \left(\frac{1}{2} [E](\epsilon_x)^2 - [E]\epsilon_x \epsilon_0 + \epsilon_x \sigma_0 \right) dV - P \int_0^L \epsilon_{xx} dx \quad (4.6)$$

While the offset distance is dictated as a design variable in the larger optimization procedure, the term used is dictated by the analysis method employed. For an eigenvalue problem, the initial stress term is used to account for the closed gap, after which the displacements in the sleeve and copper waveguide are the same. Alternatively, the initial strain term can be used for a two-step load-displacement analysis as a validation case.

The eigenvalue problem may be formulated by setting the first variation of Eq. (4.6) to zero. Focusing on the total strain energy term and distinguishing between the post gap strain ϵ_c and the initial strain ϵ_0 :

$$\delta U = \int \left(\frac{1}{2} E \delta \epsilon_c \epsilon_c + \frac{1}{2} E \epsilon_c \delta \epsilon_c + E \delta \epsilon_c \epsilon_0 \right) dV = \delta U_1 + \delta U_2 \quad (4.7)$$

Expanding Eq. (4.7) in terms of the relationship within Eq. (4.5) and consolidating like terms [43]:

$$\begin{aligned} \delta U_1 &= \int_0^L \left[EA \left(\frac{du}{dx} \right) \frac{d\delta u}{dx} + EQ \left(\frac{d^2w}{dx^2} \right) \frac{d\delta u}{dx} + EQ \left(\frac{du}{dx} \right) \frac{d^2\delta w}{dx^2} + EI \left(\frac{d^2w}{dx^2} \right) \frac{d^2\delta w}{dx^2} \right. \\ &\quad \left. + EA \frac{d\delta u}{dx} \frac{du_0}{dx} + EQ \frac{d^2\delta w}{dx^2} \frac{du_0}{dx} + EQ \frac{d\delta u}{dx} \frac{d^2w_0}{dx^2} + EI \frac{d^2\delta w}{dx^2} \frac{d^2w_0}{dx^2} \right] dx \quad (4.8) \\ \delta U_2 &= \int_0^L \left[EA \left(\frac{1}{2} \left(\frac{dw}{dx} \right)^2 + \frac{1}{2} \left(\frac{du}{dx} \right)^2 \right) \frac{d\delta u}{dx} + EA \left(\frac{du}{dx} \frac{dw}{dx} + \frac{1}{2} \left(\frac{dw}{dx} \right)^3 + \frac{1}{2} \left(\frac{du}{dx} \right)^2 \frac{dw}{dx} \right) \frac{d\delta w}{dx} \right. \\ &\quad + EQ \left(\frac{d^2w}{dx^2} \right) \frac{dw}{dx} \frac{d\delta w}{dx} + EA \left(\left(\frac{du}{dx} \right)^2 + \frac{1}{2} \left(\frac{dw}{dx} \right)^2 \frac{du}{dx} + \frac{1}{2} \left(\frac{du}{dx} \right)^3 \right) \frac{d\delta u}{dx} \\ &\quad + EQ \left(\frac{d^2w}{dx^2} \right) \frac{du}{dx} \frac{d\delta u}{dx} + EQ \left(\frac{1}{2} \left(\frac{dw}{dx} \right)^2 + \frac{1}{2} \left(\frac{du}{dx} \right)^2 \right) \frac{d^2\delta w}{dx^2} \\ &\quad + EA \left(\frac{1}{2} \left(\frac{dw_0}{dx} \right)^2 + \frac{1}{2} \left(\frac{du_0}{dx} \right)^2 \right) \frac{d\delta u}{dx} \\ &\quad + EA \left(\frac{du_0}{dx} + \frac{1}{2} \left(\frac{dw_0}{dx} \right)^2 + \frac{1}{2} \left(\frac{du_0}{dx} \right)^2 \right) \left(\frac{d\delta w}{dx} \right)^2 \\ &\quad + EA \left(\frac{du_0}{dx} + \frac{1}{2} \left(\frac{dw_0}{dx} \right)^2 + \frac{1}{2} \left(\frac{du_0}{dx} \right)^2 \right) \left(\frac{d\delta u}{dx} \right)^2 + EQ \left(\frac{d^2w_0}{dx^2} \right) \left(\frac{d\delta w}{dx} \right)^2 \\ &\quad \left. + EQ \left(\frac{d^2w_0}{dx^2} \right) \left(\frac{d\delta u}{dx} \right)^2 + EQ \left(\frac{1}{2} \left(\frac{dw_0}{dx} \right)^2 + \frac{1}{2} \left(\frac{du_0}{dx} \right)^2 \right) \frac{d^2\delta w}{dx^2} \right] dx \quad (4.9) \end{aligned}$$

Gap Modeling Using Prestress Terms

where δU_2 corresponds to the higher order terms that are neglected in the analysis. In each of these terms, Q corresponds to the first area moment of inertia.

$$EQ = \int EzdA \quad (4.10)$$

In a homogenous structure, Q would be equal to zero when taken about the structure's centroidal axis. However, for structures composed of multiple materials, these values become nonzero and are proportional to the areas of each k^{th} material multiplied by its distance above or below the global centroidal axis.

$$EQ = \int EzdA = \int E(z_k + z_0)dA \approx z_0A \quad (4.11)$$

Returning to the potential of the applied compressive load P from Eq. (4.4), inserting Eq. (4.5) updates the equation such that [41]:

$$V = P \int_0^L \epsilon_{xx} dx = P \int_0^L \left(\frac{du}{dx} + \frac{1}{2} \left(\frac{du}{dx} \right)^2 + \frac{1}{2} \left(\frac{dw}{dx} \right)^2 \right) dx \quad (4.12)$$

In an inextensible beam, the neutral axis is assumed to be a constant length, and therefore all $\frac{du}{dx}$ terms are zero, leaving only the term corresponding to the end shortening due to transverse deflection as the structure buckles. Looking next at the first variation, as was done with the strain energy, the equation becomes:

$$\delta V = P \int_0^L \left(\frac{d\delta u}{dx} + \frac{du}{dx} \frac{d\delta u}{dx} + \frac{dw}{dx} \frac{d\delta w}{dx} \right) dx \quad (4.13)$$

Substituting Eqs. (4.8) and (4.13) back into the first variation of Eq. (4.1) results in [43]

$$\begin{aligned} \Delta^{(1)}\Pi = 0 = \int_0^L \left[EA \left(\frac{du}{dx} \right) \frac{d\delta u}{dx} + EQ \left(\frac{d^2w}{dx^2} \right) \frac{d\delta u}{dx} + EQ \left(\frac{du}{dx} \right) \frac{d^2\delta w}{dx^2} + EI \left(\frac{d^2w}{dx^2} \right) \frac{d^2\delta w}{dx^2} \right. \\ \left. + EA \frac{d\delta u}{dx} \frac{du_0}{dx} + EQ \frac{d^2\delta w}{dx^2} \frac{du_0}{dx} + EQ \frac{d\delta u}{dx} \frac{d^2w_0}{dx^2} + EI \frac{d^2\delta w}{dx^2} \frac{d^2w_0}{dx^2} \right. \\ \left. - P \left(\frac{d\delta u}{dx} + \frac{du}{dx} \frac{d\delta u}{dx} + \frac{dw}{dx} \frac{d\delta w}{dx} \right) \right] dx + \delta U_2 + \delta V^e \end{aligned} \quad (4.14)$$

$$\text{where } V^e = -\sum_{k=1}^n (w_k F_k + \theta_k M_k), \text{ for } k = 1 \text{ to } n \text{ nodes} \quad (4.15)$$

With the formulation complete, and neglecting higher order terms, the equation can next be discretized in accordance with finite element method. The exact nature of the representative equations for axial and transverse displacements will vary depending upon which beam elements are employed, such as Euler-Bernoulli beam elements or Timoshenko

beam elements. In both cases, the equations used will be composed of some combination of both linear shape functions and the Hermite Cubic shape functions, with the former being used for axial deformation.

For a Timoshenko Beam Element, an additional constraint equation is added, relating the rotation θ to both the derivative of the transverse displacement w and the shear rotation ψ [44]:

$$\frac{dw}{dx} = \theta + \psi \quad (4.16)$$

This updates the transverse displacement w so that it can be divided into a portion due to bending w_b and a portion due to shear w_s , with the latter only dependent upon the shear load V

$$w = w_b + w_s \quad (4.17)$$

$$\frac{dw_s}{dx} = \kappa GA \psi, \text{ where } \psi = \frac{-V}{\kappa GA} \quad (4.18)$$

Rather than the standard Hermite Cubic shape functions, the shape functions used for these Timoshenko elements are found in Przemieniecki [45]. Nevertheless, for either element type an issue between the original, undeformed element lengths L_0 and the shortened element lengths L that are present after initial strain ε_0 . As a result, two sets of nodal displacements exist in the finite element analysis of this model: those for before any load was applied, and those for after the initial strain is reached.

Discretizing in accordance with either element type and integrating over the initial length L_0 , the initial displacements can be represented by

$$[K_0] \begin{Bmatrix} u_{10} \\ w_{10} \\ \theta_{10} \\ u_{20} \\ w_{20} \\ \theta_{20} \end{Bmatrix} = \begin{Bmatrix} P_0 \\ F_{10} \\ M_{10} \\ -P_0 \\ F_{20} \\ M_{20} \end{Bmatrix} \quad (4.19)$$

where K_0 corresponds to the initial stiffness matrix and P, F, and M correspond to the axial force, shear force, and moment at each end of the element before the gap's closing. Discretizing Eq. (4.14) and integrating across each element's now shortened length results the following nodal form of the equation:

Gap Modeling Using Prestress Terms

$$[K] \begin{Bmatrix} u_1 \\ w_1 \\ \theta_1 \\ u_2 \\ w_2 \\ \theta_2 \end{Bmatrix} + [K_0] \begin{Bmatrix} u_{10} \\ w_{10} \\ \theta_{10} \\ u_{20} \\ w_{20} \\ \theta_{20} \end{Bmatrix} - P[N] \begin{Bmatrix} u_1 \\ w_1 \\ \theta_1 \\ u_2 \\ w_2 \\ \theta_2 \end{Bmatrix} - \begin{Bmatrix} P \\ F_1 \\ M_1 \\ -P \\ F_2 \\ M_2 \end{Bmatrix} = ([K] - P[N]) \begin{Bmatrix} u_1 \\ w_1 \\ \theta_1 \\ u_2 \\ w_2 \\ \theta_2 \end{Bmatrix} + \left([K_0] \begin{Bmatrix} u_{10} \\ w_{10} \\ \theta_{10} \\ u_{20} \\ w_{20} \\ \theta_{20} \end{Bmatrix} - \begin{Bmatrix} P \\ F_1 \\ M_1 \\ -P \\ F_2 \\ M_2 \end{Bmatrix} \right) = 0 \quad (4.20)$$

where K corresponds to the element stiffness matrix and N corresponds to the geometric stiffness matrix. Using the relationship in Eq. (4.19), Eq. (4.20) can then be updated to:

$$([K] - P[N]) \begin{Bmatrix} u_1 \\ w_1 \\ \theta_1 \\ u_2 \\ w_2 \\ \theta_2 \end{Bmatrix} + \left([K_0] \begin{Bmatrix} u_{10} \\ w_{10} \\ \theta_{10} \\ u_{20} \\ w_{20} \\ \theta_{20} \end{Bmatrix} - \begin{Bmatrix} P \\ F_1 \\ M_1 \\ -P \\ F_2 \\ M_2 \end{Bmatrix} \right) = ([K] - P[N]) \begin{Bmatrix} u_1 \\ w_1 \\ \theta_1 \\ u_2 \\ w_2 \\ \theta_2 \end{Bmatrix} + \left(\begin{Bmatrix} P_0 \\ F_{10} \\ M_{10} \\ -P_0 \\ F_{20} \\ M_{20} \end{Bmatrix} - \begin{Bmatrix} P \\ F_1 \\ M_1 \\ -P \\ F_2 \\ M_2 \end{Bmatrix} \right) = 0 \quad (4.21)$$

In prior literature, such as Shames and Dym, the applied load P is equal to $-\lambda$ [43], but here the negative is already included due to the assumption of the load being compressive in nature. Using the identities outlined within Przemieniecki, K and N matrices become:

$$[K] = \begin{bmatrix} \frac{EA}{L} & 0 & \frac{EQ}{L} & -\frac{EA}{L} & 0 & -\frac{EQ}{L} \\ 0 & \frac{12EI}{L^3(1+\Phi_s)} & \frac{6EI}{L^2(1+\Phi_s)} & 0 & -\frac{12EI}{L^3(1+\Phi_s)} & \frac{6EI}{L^2(1+\Phi_s)} \\ \frac{EQ}{L} & \frac{6EI}{L^2(1+\Phi_s)} & \frac{(4+\Phi_s)EI}{L(1+\Phi_s)} & -\frac{EQ}{L} & -\frac{6EI}{L^2(1+\Phi_s)} & \frac{(2-\Phi_s)EI}{L(1+\Phi_s)} \\ -\frac{EA}{L} & 0 & -\frac{EQ}{L} & \frac{EA}{L} & 0 & \frac{EQ}{L} \\ 0 & \frac{12EI}{L^3(1+\Phi_s)} & \frac{6EI}{L^2(1+\Phi_s)} & 0 & \frac{12EI}{L^3(1+\Phi_s)} & -\frac{6EI}{L^2(1+\Phi_s)} \\ \frac{EQ}{L} & \frac{6EI}{L^2(1+\Phi_s)} & \frac{(2-\Phi_s)EI}{L(1+\Phi_s)} & \frac{EQ}{L} & -\frac{6EI}{L^2(1+\Phi_s)} & \frac{(4+\Phi_s)EI}{L(1+\Phi_s)} \end{bmatrix} \quad (4.22)$$

$$[N] = \begin{bmatrix} \frac{1}{L} & 0 & 0 & -\frac{1}{L} & 0 & 0 \\ 0 & \frac{\left(5 + \frac{1}{(1+\Phi_s)^2}\right)}{5L} & \frac{1}{10(1+\Phi_s)^2} & 0 & -\frac{\left(5 + \frac{1}{(1+\Phi_s)^2}\right)}{5L} & \frac{1}{10(1+\Phi_s)^2} \\ 0 & \frac{1}{10(1+\Phi_s)^2} & \frac{L}{60} \left(5 + \frac{3}{(1+\Phi_s)^2}\right) & 0 & -\frac{1}{10(1+\Phi_s)^2} & -\frac{L(2+10\Phi+5\Phi^2)}{60(1+\Phi_s)^2} \\ -\frac{1}{L} & 0 & 0 & \frac{1}{L} & 0 & 0 \\ 0 & -\frac{\left(5 + \frac{1}{(1+\Phi_s)^2}\right)}{5L} & -\frac{1}{10(1+\Phi_s)^2} & 0 & \frac{\left(5 + \frac{1}{(1+\Phi_s)^2}\right)}{5L} & -\frac{1}{10(1+\Phi_s)^2} \\ 0 & \frac{1}{10(1+\Phi_s)^2} & -\frac{L(2+10\Phi+5\Phi^2)}{60(1+\Phi_s)^2} & 0 & -\frac{1}{10(1+\Phi_s)^2} & \frac{L}{60} \left(5 + \frac{3}{(1+\Phi_s)^2}\right) \end{bmatrix} \quad (4.23)$$

where

$$\Phi_s = \frac{12EI}{\kappa GA_s L^2} \quad (4.24)$$

As stated earlier, if the beam is homogenous, then the EQ terms would go to zero due to symmetry, and the matrix in Eq. (4.22) would reduce to the standard form shown in Przemieniecki. Additionally, if the materials' shear stiffnesses are increased to near infinity, then Φ_s would reduce to zero and both matrices would further reduce to their Euler-Bernoulli forms.

3. Single Waveguide Implementation

For the foregoing revised eigenvalue problem, an example waveguide [17] was generated to test the procedure against a load-displacement analysis. In Fig. 4.4, the variation in cross sectional areas is shown with 4.4A denoting the unslotted cross section and 4.4B denoting the slotted cross section.

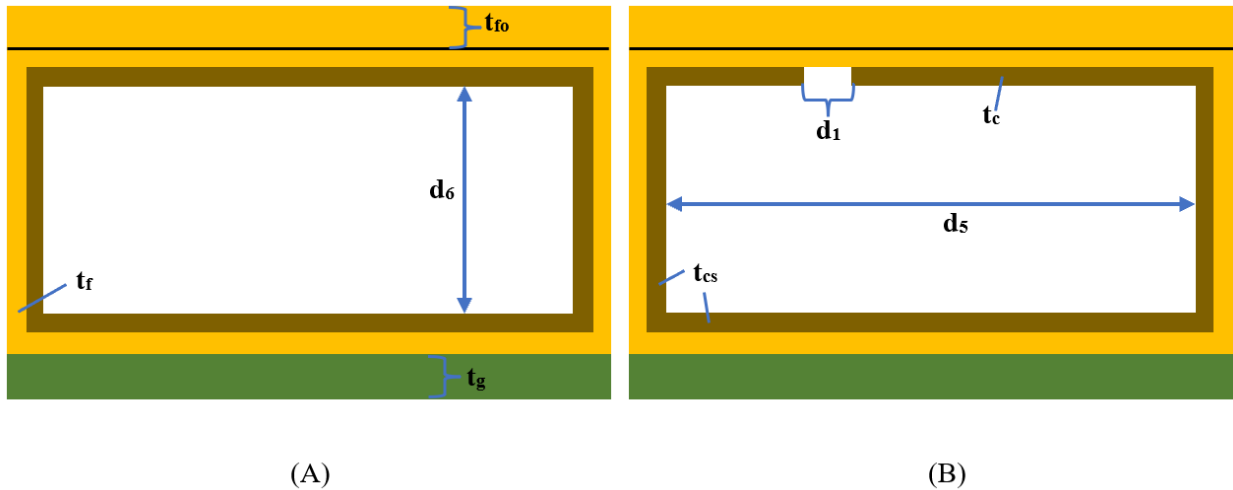


Figure 4.4 Varying Cross Section. Along the waveguide's length, the presence of a slot causes the waveguide's cross section to change, influencing its stiffness, between unslotted cross sections (A) and slotted cross sections (B).

Each material has its own independent thickness, as denoted in Table 4.1, alongside the dimensions corresponding to the waveguide itself (d_1-d_6). The copper thickness is divided between the top slotted surface t_c and the unslotted sidewalls and bottom t_{cs} . Additionally, the graphite epoxy composite used for the inner mold line is divided between the thickness of the 0° plys t_{ga} , 45° plys t_{g45} , and the 90° plys t_{gn} , though the optimization process discussed later in the document heavily favors the 0° plys in all designs using a $[0\ 90]_s$ or $[0\ +45\ -45\ 90]_s$ layup.

Single Waveguide Implementation

Table 4.1 Variable Nomenclature.

Dimension	Representative	Bounds	
Waveguide Dimensions		Lower (mm)	Upper (mm)
Slot Width	d_1	1	3
Slot Length	d_2	-	-
Slot Offset (mid-slot to mid-line)	d_3	2	7
Slot Spacing	d_4	-	-
Waveguide Inner Width	d_5	-	-
Waveguide Inner Height	d_6	8	12
Waveguide Length	L	-	-
Slot Corner Fillet Radius	r	0.0833	1.5
Material Thicknesses			
Copper Thickness (Slotted surface)	t_c	0.125	2
Copper Thickness (Unslotted surface)	t_{cs}	0.125	2
Fiberglass Thickness	t_f	0.125	2
Outer Mold Line Thickness	t_{fo}	0.125	2
Graphite Epoxy Thickness (0°)	t_{ga}	0.1	0.95
Graphite Epoxy Thickness (45°)	t_{g45}	0.0325	0.95
Graphite Epoxy Thickness (90°)	t_{gn}	0.0325	0.95

Due to the electromagnetic requirements, the copper waveguide's thicknesses are defined outward from the inner chamber, whose width is defined by d_5 and height by d_6 . With the basic waveguide shape created, the slots are then cut into the upper surface based upon how many are required for a given design. Every slot starts as a rectangle of width d_1 and length d_2 . Each slot is offset from the centerline of the waveguide by distance d_3 and from each successive slot by d_4 . For the low-fidelity models, the lengthwise location for each node corresponds to the ends of each slot, dividing it between two types of elements: those with a slot and those without, as shown in Fig. 4.4. Within Fig. 4.4, the green corresponds to the graphite epoxy, the orange corresponds to S-glass fiberglass, and brown corresponds to the copper waveguide itself, with each one's relevant material properties shown within Table 4.2. Copper [23] has a higher stiffness compared to S-Glass Fiberglass [46], and it is much denser and slightly weaker than the T300/5208 Graphite Epoxy [47] used for the supporting inner mold line.

Table 4.2 Material Properties.

	Young's Modulus (GPa)	Poisson's Ratio	Density (kg/m ³)
Copper (C26000)	110	0.35	8960
Fiberglass	89	0.22	2490
Graphite-Epoxy (T300/5208)	Axial - 132.38 Transverse - 10.76	$\nu_{12 \text{ or } 13}$: 0.24 ν_{23} : 0.49	1800

For either element type, the model is placed under a compressive axial load while pinned at each end. The location for this pinned condition depends upon where the common nodes are chosen for the 1D case within MATLAB. While

the nodes may be placed anywhere the user desires, the varying cross sections shown in Fig. 4.4 indicate that the vertical location for each element's modulus weighted centroid y_n , centroid y_c , and center of mass y_m will vary as:

$$y_n = \frac{\sum_i^n E_i A_i y_{ni}}{\sum_i^n E_i A_i}, \text{ for } i = 1 \text{ to } n \text{ areas} \quad (4.25)$$

$$y_c = \frac{\sum_i^n A_i y_{ci}}{\sum_i^n A_i}, \text{ for } i = 1 \text{ to } n \text{ areas} \quad (4.26)$$

$$y_m = \frac{\sum_i^n M_i y_{mi}}{\sum_i^n M_i}, \text{ for } i = 1 \text{ to } n \text{ areas} \quad (4.27)$$

The typical location used within the MATLAB models is halfway between the modulus weighted centroid for each element. With the nodal axis chosen, the stiffnesses are then calculated about that chosen axis:

$$EI = \sum_i^n E_i \cdot (I_i + A_i d_i^2), \text{ for } i = 1 \text{ to } n \text{ areas} \quad (4.28)$$

In Eq. (4.28), d_i corresponds to the distance between the target axis and the local centroidal axis for each sub area on the cross section.

Based upon the dimensions for Kim and Canfield's Design 4 [22], an initial analysis shows that the structure should buckle before copper failure occurs. However, inclusion of the stress concentrations present at the slot corners shows that the copper will fail well before reaching the buckling load, as in Fig. 4.5. Even if the fillet radius is increased to its maximum value of half the slot width, as in the analyses below, failure still occurs before reaching the buckling load.

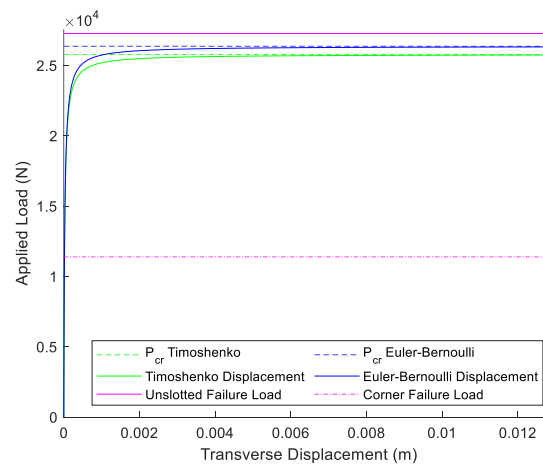


Figure 4.5 Nominal Buckling Analysis. Buckling occurs before unslotted copper failure, but local failure at slot corners occurs well before buckling.

However, Fig. 4.6 shows how implementing an initial offset of only 0.8 mm delays the copper loading long enough to increase the corner failure load to slightly more than the predicted failure load when using traditional Timoshenko

Single Waveguide Implementation

elements. This also shows that the eigenvalue accurately predicts the buckling load, as the load-displacement curves do not become unstable until they approach the predicted buckling load.

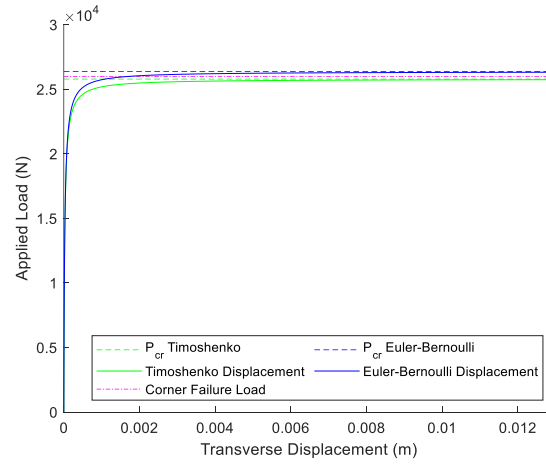


Figure 4.6 Gap Implementation. Inclusion of an initial gap delays the copper loading, allowing the supporting materials to take the majority of the load and prevent local failure of the slot corners.

Further increase in the offset linearly increases the load at which copper failure will occur, as shown in Fig. 4.7, but this is limited by the potential buckling of the supporting material prior to the gap's closure, which is accounted for in the optimization routine described next.

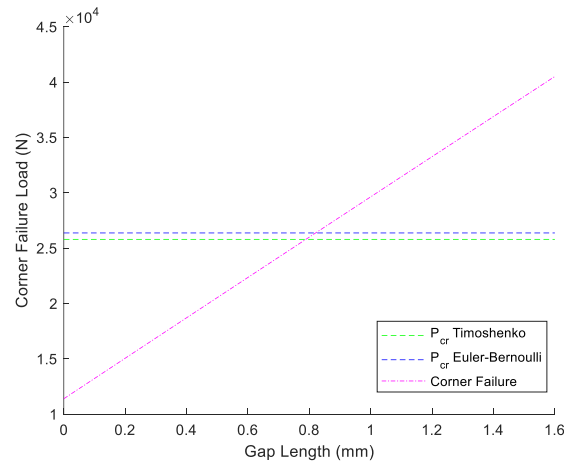


Figure 4.7 Critical Load vs. Gap Length. As the gap length increases, more and more of the load is absorbed by the supporting material.

4. Optimization

The inclusion of the EQ terms to account for non-uniform cross-sections and the gap to prevent premature failure of the copper insert allows for an optimization procedure to account for them and to develop designs that do not fail due to stress, leading to designs that are lighter and/or stronger. Within the optimization procedure, a low fidelity model of the designs is subjected to constraints that ensure the waveguide dimensions are physically feasible, that they meet minimum loading and maximum mass constraints, and that they meet the necessary electromagnetic performance requirements. Additionally, the optimization allows for designs to be tested both with and without the initial gap to show its impact.

Throughout the course of the multiobjective optimization, the two objectives employed were to minimize the mass and maximize the buckling load, using a MATLAB implementation [27] of Sequential Quadratic Programming (SQP) [28]. The initial Pareto front was generated using the weighted sums method

$$\min f = \eta \cdot f_1 + (1 - \eta) \cdot f_2 \quad (4.31)$$

$$f_1 = \frac{P_{cr0} - P_{cr}}{P_{cr0}} \quad (4.32)$$

$$f_2 = \frac{M_{tot} - M_{tot0}}{M_{tot0}} \quad (4.33)$$

where P_{cr0} represents the minimum acceptable buckling load and M_{tot0} represents the maximum acceptable total mass. The front was then filled in through the use of the epsilon constraint method, which chooses one of the objectives in Eq. (4.31), while constraining the other to a parametrically varying value, ϵ

$$\min f_1 \text{ s.t. } f_2 \leq \epsilon \quad (4.34)$$

$$\min f_2 \text{ s.t. } f_1 \leq \epsilon \quad (4.35)$$

Depending upon which value is being optimized, the other half is converted into a constraint where P_{cr0} or M_{tot0} in the numerator are replaced by a target value along the suspected Pareto front based upon the initial results from weighted sums [37].

In both epsilon constraint and weighted sums methods, a set of 24 non-positive inequality constraints are imposed. The first nine constraints in Table 4.3 are grouped together as geometric constraints, as they ensure the geometry of the waveguide is feasible.

Table 4.3 Geometric Constraints.

$$\begin{aligned}
 g_1 &= d_6 - d_5 \\
 g_2 &= d_1 + 2 * (d_3 + t_{cs}) - d_5 \\
 g_3 &= 2 * d_1 - d_5 \\
 g_4 &= d_2 - d_4 \\
 g_5 &= d_2 + (n_{slots} - 1) * d_4 - L_c \\
 g_6 &= \frac{M_{tot} - M_{tot0}}{M_{tot0}} \\
 g_7 &= \frac{P_{cr0} - P_{cr}}{P_{cr0}} \\
 g_8 &= r - \frac{d_1}{2} \\
 g_9 &= t_g - 2 \text{ mm}
 \end{aligned}$$

Constraints g_1 through g_5 ensure that the waveguide is wider than it is tall and that the slots do not overlap with either one another, or the edges of the walls of the waveguides itself. Constraints g_6 and g_7 ensure that any designs created are no worse than the worst acceptable design, and when filling in the Pareto front using epsilon constraint method, will be updated with the target value in place of M_{tot0} or P_{cr0} , depending upon which term is being optimized. Constraint g_8 ensures that the fillet radius is no larger than half of the slot width, which would result in an overall shortening of the slot and the ends having no points perpendicular to the slot sides. Finally, g_9 is a sizing constraint that, when combined with the bounds in Table 4.1, ensures that the inner and outer mold lines have the same maximum thickness, regardless of ply thicknesses within the inner mold line.

The second set are stress constraints in Table 4.4 ensure no material exceeds its yield criteria prior to buckling.

Table 4.4 Stress Constraints.

$$\begin{aligned}
 g_{10} &= \frac{\sigma_{ga} - \sigma_{gyield_a}}{\sigma_{gyield_a}} \\
 g_{11} &= \frac{\sigma_{gt} - \sigma_{gyield_n}}{\sigma_{gyield_n}} \\
 g_{12} &= \frac{\sigma_f - \sigma_{fyield}}{\sigma_{fyield}} \\
 g_{13} &= \frac{\sigma_{corner} - \sigma_{cyield}}{\sigma_{cyield}} \\
 g_{14} &= \frac{\sigma_c - \sigma_{cyield}}{\sigma_{cyield}}
 \end{aligned}$$

Constraints g_{10} and g_{11} verify that none of the plies within the graphite epoxy fail due to axial stress or transverse stress in their local coordinate systems. Similarly, constraints g_{12} and g_{14} ensure that the stress within the fiberglass sleeve, fiberglass outer mold line, and the copper waveguide do not exceed their yield stress, respectively. However, g_{13} also ensures that the stress concentrations at the corners of the slots in the copper waveguide's upper surface do not exceed the yield stress for copper either. The aim of g_{13} is to ensure local failure does not occur before buckling, thereby preventing degradation in performance, either structural or electromagnetic, due to local failure.

The next pair of constraints in Table 4.5, g_{15} and g_{16} , ensure that the gap itself is feasible. Constraint g_{15} ensures that the axial strain immediately before the supporting material buckles must be greater than the strain required to close the initial gap. Constraint g_{16} prevents infeasible negative gaps from arising during the optimization procedure.

Table 4.5 Gap Constraints.

$$g_{15} = \frac{\delta}{L} - \epsilon_{cr}$$

$$g_{16} = -\delta$$

The next set of constraints in Table 4.6 are aimed at ensuring the electromagnetic performance of the waveguide. Constraints g_{17} and g_{18} ensures that the centerline spacing d_3 is within ten percent of the theoretical target value d_{3t} , as calculated in accordance Misilmani et al's Eq. (2) [48]. Constraints g_{19} and g_{20} ensures that the waveguide wavelength λ_g is within ten percent of the chosen slot spacing. The ten percent limit is chosen to ensure the slots remain in phase with one another, as shifting the slot locations a few millimeters can cause the design to resonate with a frequency outside of the design's bandwidth. If the slots are no longer in phase, the radiation patterns from each slot will not reinforce one another properly and the overall performance will be degraded.

Table 4.6 Electromagnetic Constraints.

$$g_{17} = \frac{d_{3t} - d_3}{d_{3t}} - 0.1$$

$$g_{18} = \frac{d_3 - d_{3t}}{d_{3t}} - 0.1$$

$$g_{19} = \frac{\lambda_g}{2} - d_4 - 0.1$$

$$g_{20} = \frac{d_4 - \frac{\lambda_g}{2}}{d_4} - 0.1$$

Optimization

The final set of four constraints in Table 4.7 are those dealing specifically with the expansion of the single waveguide into a panel of multiple waveguides together. Expanding the designs into panels simply supported on all sides introduced a phenomenon known as dimpling, as illustrated in Fig. 4.8.

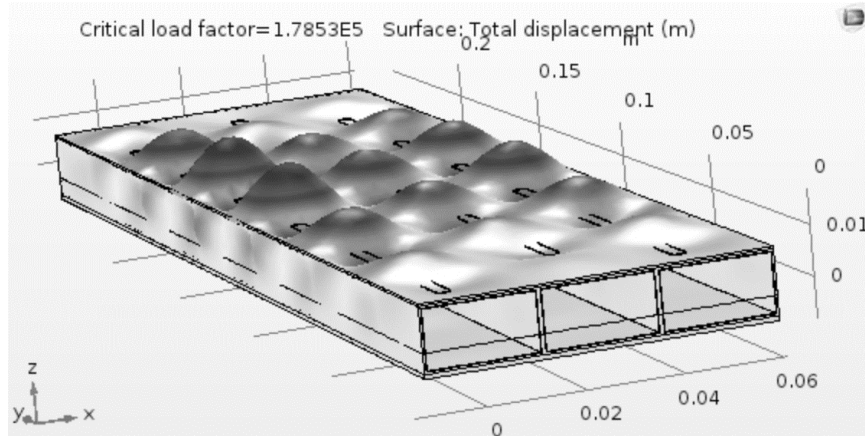


Figure 4.8 Dimpled Panel Model. Narrower panels pinned on all sides tended to see local failure, known as dimpling.

As a result, the constraints in Table 4.7 were introduced to prevent this phenomenon, as well as ensure the panel meets its loading requirements.

Table 4.7 Panel Constraints.

$$g_{21} = \frac{\max(\sigma_c, \sigma_f, \sigma_g) - (\sigma_{bottom\ dimple})}{\max(\sigma_c, \sigma_f, \sigma_g)}$$

$$g_{22} = \frac{\max(\sigma_c, \sigma_f) - (\sigma_{side\ dimple})}{\max(\sigma_c, \sigma_f)}$$

$$g_{23} = \frac{\max(\sigma_c, \sigma_f) - (\sigma_{top\ dimple})}{\max(\sigma_c, \sigma_f)}$$

$$g_{24} = \frac{P_{Panel0} - P_{Panel}}{P_{Panel0}}$$

Constraints g_{21} , g_{22} , and g_{23} prevent dimpling of the bottom, sides, and top edges of the panel in accordance with Ley et. al [49]:

$$\sigma_{dimple} = \frac{2E_f}{(1 - \nu_f^2)} \left(\frac{t_f}{s}\right)^2 \quad (4.36)$$

The equation is formulated in terms of the facesheet's Young's Modulus E_f , Poisson's Ratio ν_f , and thickness t_f , as well as the cell size s . Within the waveguide designs, the material values are based upon the material present on each face, while the "cell size" is based upon the corresponding dimension of the internal void. Looking back at Fig. 4.4, s

is set equal to d_5 for the top and bottom surfaces, while s is set equal to d_6 for the side walls. These differences in materials and thicknesses result in the three separate constraints. Finally, g_{24} ensures that the buckling load for a panel simply supported on four sides is greater than the load required by the panel's location along the X-47B's wing.

The first iteration of the procedure utilized weighted sums to attain an outline of the Pareto front, followed by the epsilon-constraint method to fill in the gaps between the weighted sums points. The driving constraints within the optimization procedure were the yield stress of the copper waveguide at the slot corners, the maximum offset length of the gap, the centerline slot spacing, and the dimpling of the top surface. Looking first at the centerline offset, this value contributed to the s/D term in the approximation for the stress concentration factor at the slot corners [21]

$$K_t = \left(-4.262 \left(\frac{d}{D} \right) + 4.712 \right) \left(1 + \frac{0.0308}{\frac{s}{D}} \right) \left(\frac{r}{D} \right)^{-0.295} \quad (4.37)$$

This equation was developed through the use of high-fidelity models in a prior publication [21], allowing the optimizer's low fidelity models to properly account for the stress concentrations at the slot corners. To reduce the stress concentration factor, the optimizer would attempt to increase s/D , but doing so would adversely affect the reflection coefficient [48] and harm the design's electromagnetic performance, and so the lower mass designs still fell short of the maximum centerline spacing.

Looking next at the maximum gap offset length, it was closely tied to the corner stress as well due to its ability to reduce the percentage of the load the copper experienced prior to buckling. However, if the gap was increased too much, the surrounding materials would begin to buckle before the copper ever came into contact with the loading surface. The inclusion of the dimpling constraints—implemented after high-fidelity models showed such failures—made designs without an initial gap impossible, as at least one constraint was always violated. Removing the dimpling constraints and setting the offset to zero resulted in the small Pareto front shown in Fig. 4.9, which is entirely dominated by the Pareto front for designs with a gap. The gap drastically increases the buckling load the designs can support, while also decreasing the corresponding mass due to the models without gaps needing to thicken the copper to prevent failure at the slot corners.

Optimization

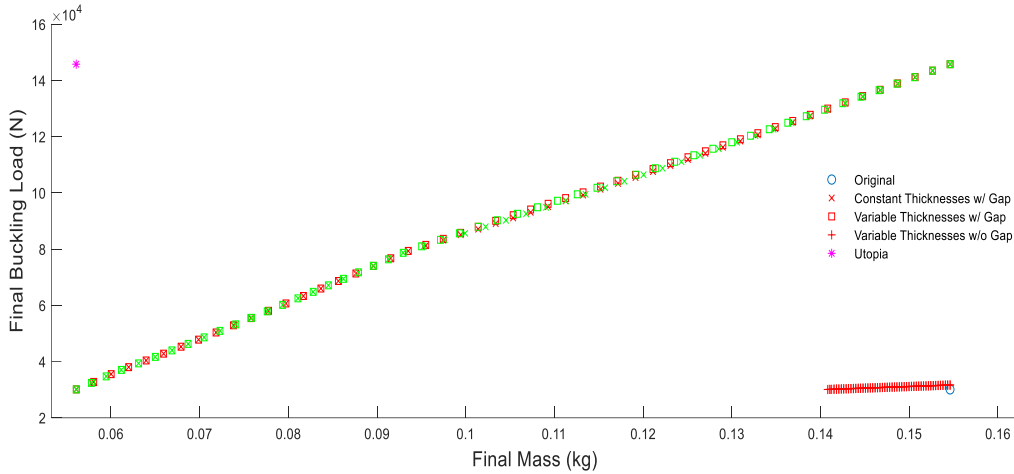


Figure 4.9 Optimized Pareto Front. The gap allowed for designs with lower masses and/or stronger buckling loads, while the front without a gap is entirely dominated.

The designs without a gap also could not satisfy the stress constraints without variable wall thickness of the copper waveguide, even with the dimpling constraints removed. If all four walls were required to be the same thickness, no feasible designs were found. Instead, allowing the slotted surface thickness to vary allowed the surrounding walls to be thickened and thus take some of the load away from the slotted surface and its concentration factors. The impact of allowing this variable thickness can also be seen in the gap models, with the variable thickness designs achieving slightly lower masses for the same buckling load or larger buckling loads for the same mass. Both were achieved by allowing the optimizer to thicken the slotted surface without the mass penalty of thickening the other three surfaces. Allowing the antennas to shoulder a portion of the loading turns them into multifunctional structures that are stronger than designs in which the copper remained entirely unloaded, while the gap allows the designs to be much lighter and stronger than the designs loading the copper from the offset.

For the bottom left edge of Fig. 4.9's Pareto front, the designs took the copper thicknesses to their minimum thickness of 0.125 millimeters for all four edges, due to copper having the highest density of all three materials used. Consequently, the gap and thicknesses of the inner and outer mold layers gradually increased to raise the buckling load. These designs are the closest to the Utopia point due to the wider range of mass values compared to the range of buckling loads, with the one closest to the Utopia when all constraints are active having the values given in Table 4.8. The optimized design thickens the outer mold line and 0° plies of the graphite epoxy, while also taking the slot width and fillet radii to their maximum values.

Table 4.8 Pareto Design Point.

Dimension	Value
d1	3.0 mm
d2	15 mm
d3	3.0 mm
d4	19 mm
d5	22.86 mm
d6	12 mm
t _c	0.125 mm
t _{cs}	0.125 mm
t _f	0.5213 mm
t _{fo}	1.067 mm
t _{ga}	0.6984 mm
t _{gn}	0.0325 mm
t _{g45}	0 mm ([0 90] _s layup)
r	1.5 mm
δ	1.1 mm

The optimum in Table 4.8 results in a buckling load greater than the nominal design, while also being significantly lighter. The slots cause a slight penalty in all three properties shown in Table 4.9, but the cross-sectional property values remain relatively similar between the elements where a slot is present and those that are not within the overall waveguide.

Table 4.9 Optimized Element and Objective Values.

	Unslotted Elements	Slotted Elements
EI	343.7 $N \cdot m^2$	340.5 $N \cdot m^2$
EA	8.832 MN	8.790 MN
κAG	1.408 MN	1.395 MN

Table 4.10 Pareto Optimal Objective Values.

Objective Values	
P _{cr}	52.91 kN
M _{total}	0.0738 kg

Due to the length of the Pareto front, the designs can vary greatly between those that favored a minimized mass versus a maximized buckling load. The former favored enlarged slots with minimal copper thickness, while the latter favored smaller slots but a thicker slotted surface thickness to compensate for the increased concentration factor. Additionally, as the thicknesses increased in the supporting materials for the higher buckling load designs, the gaps also increased in a roughly linear fashion to keep the portion of the load in the copper from causing local failure at the slot corners.

Panel Application

5. Panel Application

After optimizing a single waveguide, the next step was to combine multiple waveguides into a panel that can be placed within the skin of a target aircraft, such as Northrop Grumman's X-47B. While the exact load distributions are not available, a representative loading distribution can be created using the aircraft's publicly available geometry shown in Fig. 4.10 and maximum gross takeoff weight (MGTOW) to estimate a wing-root moment of 10×10^6 lb.-in.

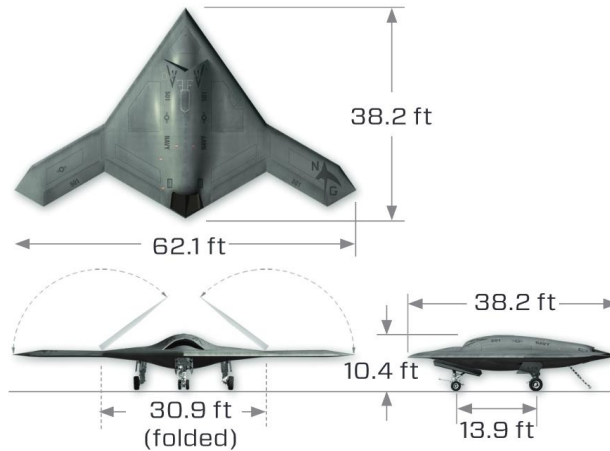


Figure 4.10 X-47B Dimensions and Areas. Using the listed dimensions, the required areas, lengths, and thicknesses could be estimated [25].

The most restrictive case used for optimization utilized the listed MGTOW of 44,000 lbs. [25], a flight load factor of 3, and a factor of safety of 1.5. Several assumptions were made when estimating the wing loading, including that the lift would be generated entirely by the portion of the wings outside of the engine nacelle, the lift distribution on the inboard section is linear due to its rapidly narrowing chord length, and elliptical lift on the constant chord length outboard section. These assumptions resulted in the moment distribution as a function of spanwise location shown in Fig. 4.11.

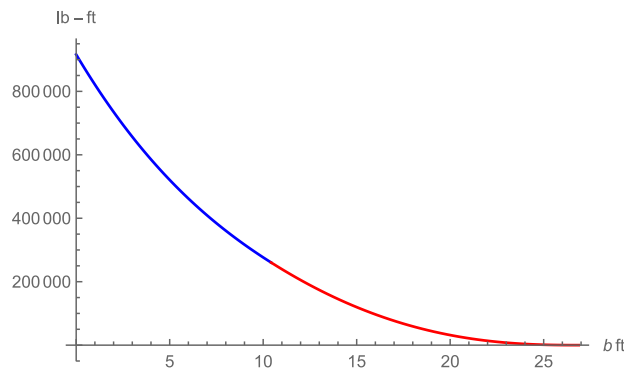


Figure 4.11 X-47B Moment Distribution. The moment decays exponentially as it approaches the wingtip.

To estimate the compressive load experienced by a panel in the upper skin of the wing, the moment is divided by the corresponding wing depth at each spanwise location, assuming that the moment is entirely supported by compressive and tensile loads in the upper and lower skins, respectively, while the shear is entirely supported by the internal spars. Dividing further by the chord length at each spanwise location, an estimate for the load per unit chord that any panel must support is shown in Fig. 4.12. This shows that, despite the decreasing moment value, the shortening chord length resulted in a spike near the hinge where the maximum load per unit span occurs. The loading was converted from pounds per foot to newtons per centimeter, but the spanwise location is shown in imperial units to match with the dimensions given by Northop Grumman.

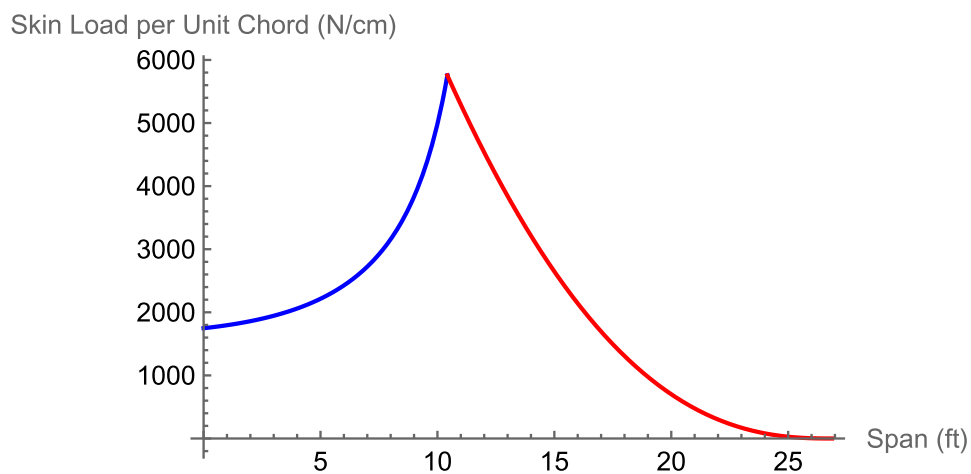


Figure 4.12 Load per Unit Span. The shortening chord lengths result in a spike near the hinge.

The underlying rib and spar spacings were unknown, but varying numbers of waveguides can be combined to form a panel of any desired width. For the purpose of the optimization, a panel was modeled as having 16 slots per waveguide and 12 waveguides per panel, so as to fit into a portion of a panel visible near the trailing edge of the wing in Fig. 4.13.

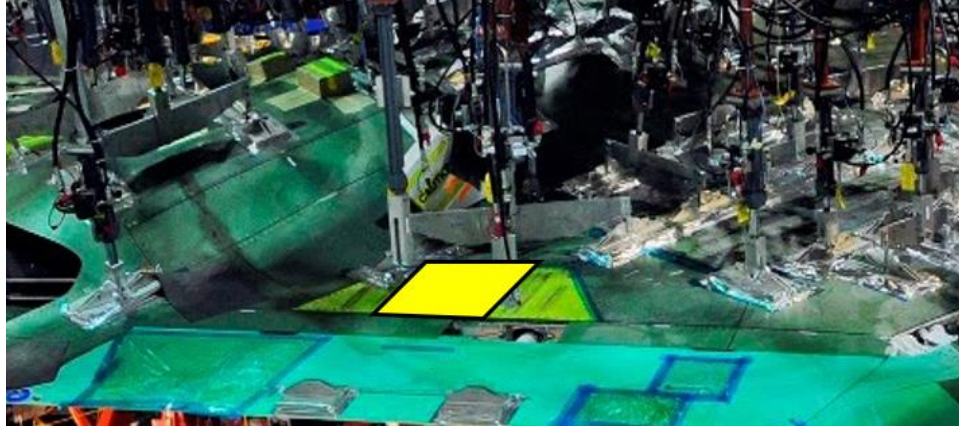


Figure 4.13 Panel Optimization Location. The test panel is placed in a location between two confirmed supports due to the underlying structure not being publicly available [50].

Due to the placement of the cables, it is assumed that ten ribs are spaced in roughly one-foot intervals along the span of the wing’s inboard section. With this assumption, the panel outlined in Fig. 4.13 would contain two waveguide panels, split down the centerline by one of the wing’s ribs.

Models with similar aspect ratios showed that local modes were prevalent, even when what appeared to be global buckling modes were seen. As a result, buckling occurs well before the loads predicted by beam equations of Timoshenko and Gere [26]. To account for panel buckling load’s relationship to the buckling load of a single waveguide beam, a curve was fit to the high-fidelity panel FEM critical load, based upon multiple aspect ratios and cross-sectional dimensions and then plotted alongside the data in Fig. 4.14.

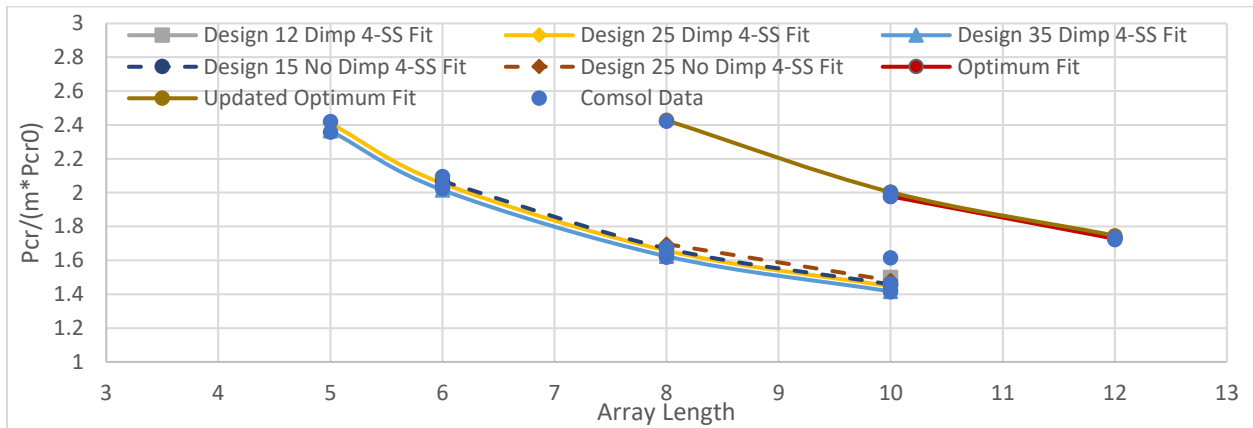


Figure 4.14 COMSOL Data and Curve Fits. The curve fit tracks the COMSOL data, following an exponential decay.

$$k = \left(-0.1524 \cdot \left(\frac{t_f}{t_{fo}} \right) + 0.3924 \cdot \left(\frac{t_{cs}}{t_c} \right) + 0.3593 \cdot \left(\frac{t_{fo}}{t_g} \right) + 3.888 \cdot \left(\frac{a}{b} \right) - 47.74 \cdot \left(\frac{d_6}{b} \right) \right) \cdot m^{-0.5031} + 0.8553 \quad (4.38)$$

where $\frac{a}{b}$ is the ratio of the panel's width over its length and m is the total waveguides. The panel factor k , can then be multiplied by the number of waveguides times the buckling load for a single waveguide from the prior analyses, allowing the 1-D models to now be used within the optimization of a larger panel. The panel's right edge is located roughly two feet from the assumed wing root in Fig. 4.12, requiring it to support a load of 185.9 N/mm.

Using the same optimization procedure as for the single waveguides, a Pareto front of potential designs is developed, with designs ranging from those with a very low mass and low buckling loads, to designs with a substantially increased buckling load and larger mass, as shown in Fig. 4.15. Additional plots in Appendix F demonstrate how the design variables varied across the front. Fig. F.2 shows that the centerline offset was increased until the previously listed constraint g_{18} prevents it from moving further out. Fig. F.3 shows that the height is linearly increased from its minimum to its maximum value before any other design variable, which then influences the trends of the remaining design variables. Figs. F.7 and F.8 show that once the height reached its maximum value, the slope of the thickness of the outer mold line t_{fo} and the 0° ply t_{ga} increase, with t_{fo} 's slope increasing slightly once t_{ga} reaches its maximum value. Additionally, Fig F.6 shows that, while it increased alongside the height initially, once the height reached its maximum value, the sleeve thickness only increases slightly until the inner and outer mold lines are at their maximum values, after which it begins to increase again. Fig F.12 also shows that the gap length was increased alongside the sleeve thickness, but began to decrease as the sleeve was left constant and the inner and outer mold lines were thickened. Once the outer mold line reached its maximum value, the gap length began to increase slightly, with the rate of growth increasing further after the inner mold line reached its maximum and the sleeve thickness began increasing again.

While all points along the front are Pareto optimal, a line was drawn between the utopia point, which marks the optimum value achieved for each objective if optimized independently, and the point closest to it to when the front is normalized by the utopian values. This point denotes a preferred optimal design that will be used for later validation.

Panel Application

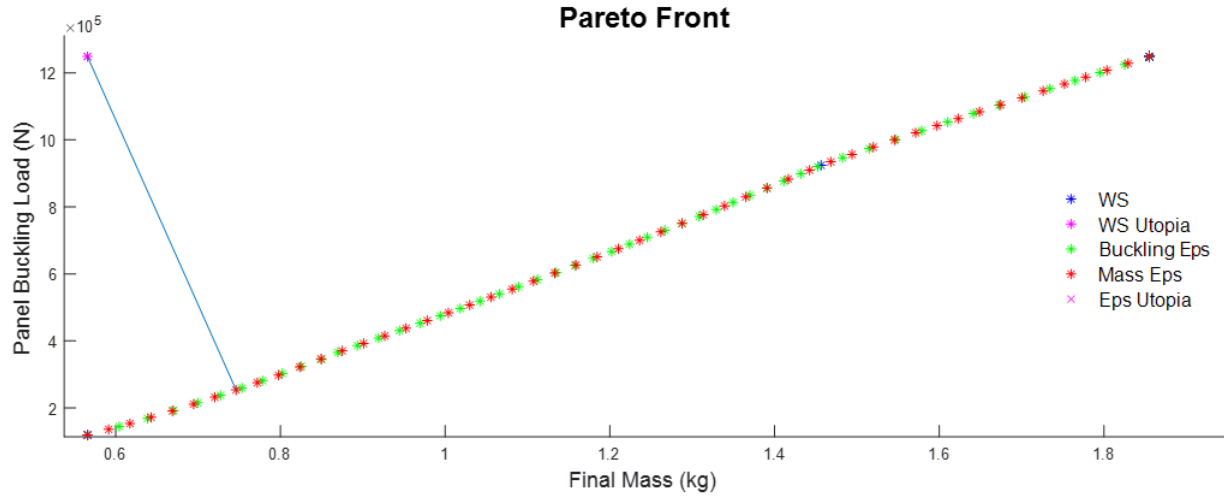


Figure 4.15 12 Waveguide Panel Optimization. The lower half of the front keeps the copper to a minimum by increasing the supporting materials, while the upper half is forced to add back copper to further increase its strength.

Just as with the single waveguide, the large variance in mass leads to the chosen optimum given in Table 4.11 favoring a decreased mass over an increased buckling load. Large slots and small thicknesses decrease the copper mass, while the favoring of graphite epoxy over fiberglass gives best strength to mass increase.

Table 4.11 Optimized Panel Dimensions.

Dimension	Value
d1	3.0 mm
d2	15 mm
d3	2.424 mm
d4	19 mm
d5	22.86 mm
d6	10.42 mm
t _c	0.125 mm
t _{cs}	0.125 mm
t _f	0.3343 mm
t _{fo}	0.4854 mm
t _{ga}	0.3599 mm
t _{gn}	0.0325 mm
t _{g45}	0 mm ([0 90] _s layup)
r	1.5 mm
δ	0.7506 mm

For this design, as with many on the lower left end of the Pareto front, the driving constraints were the dimpling constraints that ensured the fiberglass sleeve and outer mold line thicknesses are thick enough, while the graphite epoxy is thickened to provide the largest increase in strength for the lowest increase in mass. While the properties for an individual waveguide are lower for the optimized panel design, compared to their individually optimized counterparts, the panel size ensures that the properties in Table 4.12 are still strong enough to meet the load requirements.

Table 4.12 Panel Optimized Properties.

	Unslotted	Slotted
EI	1.608 $kN \cdot m^2$	1.581 $kN \cdot m^2$
EA	60.48 MN	59.99 MN
κAG	10.69 MN	10.54 MN

Table 4.13 Pareto Optimal Panel Design.

Objective Values	
P_{cr}	253.4 kN
M_{total}	0.7462 kg

Additionally, this design had a predicted panel factor of $k = 1.7322$, which when compared against the results from a higher fidelity COMSOL model, is only 0.69 percent less than the COMSOL model’s panel factor of $k = 1.7442$. The buckled structure in Fig. 16 shows the final panel buckles with a global buckling mode, though its load is slightly less, likely due to the inability to properly model the contact modelling when the gap closes. Instead, a prestress is used to approximate the load present upon the gap’s closure.

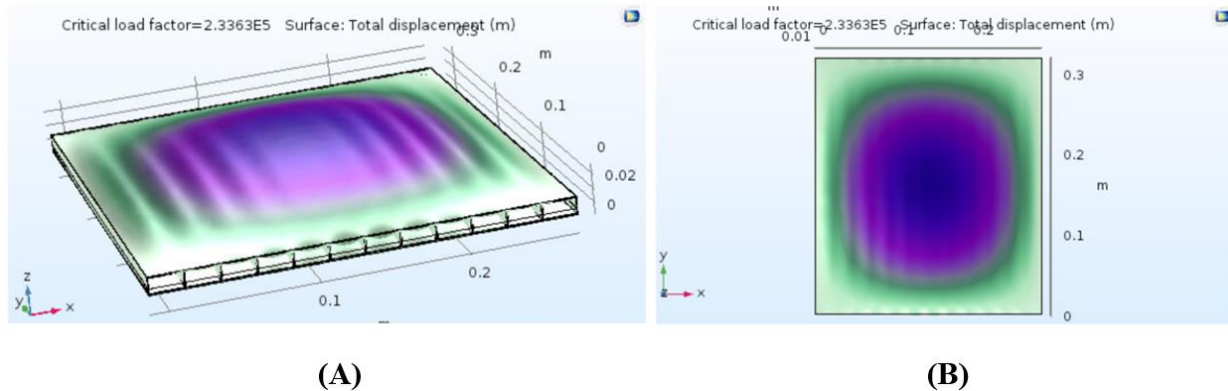


Figure 4.16 Optimum Panel Buckling Mode A) Corner View and B) Top View. The optimum design buckles with a global mode when constrained on the nodal axis.

With a fully optimized design, the panels can withstand the 4.5 load factor required for an X-47B’s flight loads, while still fitting into a panel roughly 1 ft² in size and weighing only about 1.65 lbs.

6. Conclusions

For a waveguide panel composed of multiple materials, the high stiffness of a structurally embedded copper waveguide causes it to shoulder a sizable portion of the load. Proper modeling of the stress concentrations at the slot corners showed that otherwise feasible designs would in fact fail due to high stress at the corners of the slots cut into its upper surface. Simply accounting for the fillet in the design process was insufficient to prevent failure, as the copper’s high stiffness and low yield would result in local failure well before the designs would buckle. To prevent

Conclusions

local failure due to these stress concentrations, an initial offset is required to ensure the copper does not fail prior to buckling. Implementing an initial offset between the end of the copper waveguide and the supporting materials allows for the supporting material to absorb enough of the load so that corner failure does not occur until after reaching the buckling load.

Through the use of a prestress term, the gap is accounted for within the standard eigenvalue analysis, avoiding the need to perform load-displacement analyses for every design. This is especially useful when used within a larger design optimization procedure, enabling the use of an eigenvalue buckling analysis that was impossible beforehand. The gap's inclusion allows for drastic increases in buckling load and/or decreases in mass compared to the designs without it. To expand the optimization to full panel designs, curve fits were generated based upon data taken from high-fidelity models. Using the high-fidelity data, an equation was generated to relate the buckling load of the panel, simply supported on all four sides, to the buckling load of a single waveguide design. With both the gap, stress concentration factor, and panel approximation included, the computational load for the optimization is drastically reduced and the need for both contact and plate modeling eliminated, allowing for the optimization to simplify the procedure from a high-fidelity 3D panel model down to a 1D beam model that can be rapidly optimized using a low fidelity mesh.

Chapter 5

Future Work

The hallmark of the work presented within this dissertation was reduction of computational and modelling requirements from high-fidelity 3-D models to low fidelity 1-D and 2-D models. However, this does prevent analysis of certain aspects that could be the subject for future study. The inclusion of the stress concentration factor accounted for the peak stresses that caused local failure around the slots. However, this was simplified using the 1-D beam models that employed uniform spacing and offsets for each slot in its calculations. The designs could be further refined by examining the structural effects of non-uniform slot offsets. Electromagnetic analysis of such a concept was conducted by Misilmani et. al. [48], but differences in slot shapes could also necessitate a supplemental electromagnetic analysis in parallel to further structural analysis. This would also include integrating the panels into larger models of the aircraft itself to quantify how the larger aircraft affects the radiation pattern, as well as modelling the influence of the power feed connected to the panel's ports. Additionally, the impedance of the surrounding materials would allow for better modeling of the design's electromagnetic performance, as well as how the potential deformation affects the radiation patterns and strength. The 1-D models allow for the buckling load and the load-displacement to be analyzed, but the effect of the compression of the slots would require 3-D multifunctional models impractical for optimization. Future research could investigate the effect of the compression of the slots, determining if the compression gradually shortening the slot lengths could potentially affect their electromagnetic performance. While in theory the effects should be negligible, it is something that could be investigated during the course of other analyses.

Another area for follow up research would be additional refinement of the panel fit in Chapter 4. Narrower panels would typically fail due to local dimpling or failure around the slots closest to the corners of the panels. As a result, the current iteration of the fit does not accurately predict the buckling loads of a narrow panel simply supported on four sides. Constraining the top and bottom of the loaded edges eliminated this in some models, but further modelling and analysis could provide a better fit that works over a larger range of panel widths. This would allow for the 1-D models to be used for optimization of narrower panels that may be required for small surface areas on future target aircraft. A final area of potential analysis is looking into non-uniform panels composed of multiple individual waveguides. So far, panels have been assumed to be composed of a given number of identical individual waveguides, but allowing the height and/or material thicknesses to vary along the panel may result in stronger designs.

Conclusions

Conclusions

SWASS designs have grown from the initial CLAS designs explored by the S³TD and MUSTRAP programs, to the designs proposed and analyzed by Kim, Ha, Albertson, and Canfield. Now, those designs have been updated again by the work presented within this dissertation. The creation of a governing equation for modelling stress concentrations fills in a gap in the current literature. With it, the stress concentrations in the waveguides can now be accurately predicted without the need for high-fidelity meshes, as well as those of designs on a similar scale, that previously fell outside the capabilities of the formulae in Roark's texts. The inclusion and modeling of an offset has also opened new avenues in structural design. For materials with a high stiffness, but low yield, it has now been shown that a slight offset can allow them to provide increases in strength and decreases in mass, while not compromising the structures as a whole.

The electromagnetic performance was examined in detail by the prior works by Kim, Ha, Albertson, and Canfield, but was also included within this work in the form of constraints aimed at ensuring the optimization did not favor structural performance at the expense of electromagnetic performance. These earlier works dictated the design variables that were then used in the optimization protocol, as well as which values were to be used for those not varied. A new analysis program, CREATE-RFTM SENTRi, was also employed to show that the performance was independent of the program used in the analysis. Multiple designs from along the optimized Pareto front all showed similar radiation patterns and maximum gain values, reinforcing that the optimization has maintained the performance within each design. Frequency sweeps also showed that the designs' peak performance regions included the target frequency of 10 GHz, though mismatching between the longitudinal spacing, slot length, and guided wavelength showed that two distinct regions exist with a dip in performance between 10.2 GHz and 10.3 GHz.

The introduction of an initial gap between the supporting materials and the slotted waveguide was not present in prior literature on the derivation of buckling eigenvalues or in the prior literature on SWASS models. Now that it is derived, the eigenvalue analysis accounts for the gap and eliminates the need for contact modelling and more complex models that slow the optimization process. This gap allows for designs with higher buckling loads and lower masses than previously possible. Without a gap, the inclusion of stress concentrations around the slot showed that models without a gap were entirely dominated, and only feasible if the slotted surface's thickness was independent of the unslotted surfaces' thicknesses. The use of the gap to prevent failure of the copper waveguide allows it to help shoulder

a portion of the load without failing, resulting in multifunctional designs that are stronger and/or lighter than the versions with an unloaded insert or waveguide loaded from the onset.

Moving from individual waveguides to a larger panel, a fit was created to relate the buckling of the panels pinned on all four sides to the buckling of the original single waveguide pinned on each end. This process can be done without requiring complex models of those larger panels. Issues arose with local failure and dimpling for narrow panels, but the fit works well for wider panels that show global buckling modes over local failure modes. While the exact width depends upon desired size of the panel, the 1-D model can be optimized by validating the fit for the anticipated panel against the loading at the intended integration location and size.

Appendix A. Corner Concentration Factor Data

Table A.1 Mesh Refinement Values. Finest mesh stress concentration factor converged to two significant digits.

Mesh	Corner Stress (N/m ²)	K _t	Change from Previous K _t (%)	Total Elements
Fine	140400	2.565	-	4,212
Finer	145200	2.653	3.317	5,322
Finest	143400	2.620	-1.244	7,900

Table A.2 Residuals for Each D/d Value. Global bivariate fit has a residual similar to the univariate models created for each individual model. With the overall accuracy of the same magnitude.

	Univariate R ²	Bivariate R ²
<i>D/d</i> = 1.043	0.9985	0.9834
<i>D/d</i> = 1.089	0.9980	0.9598
<i>D/d</i> = 1.14	0.9981	0.9860
<i>D/d</i> = 1.20	0.9994	0.9843
Total	0.9940	0.9135

Table A.3 Residuals for Global Fits for Each D/d Value. Bivariate fit is no longer able to maintain its accuracy for multiple slot lengths, with the inclusion of the slot-corner-distance term in the trivariate case recapturing the accuracy of the univariate fit.

	10 mm Slots			15 mm Slots		
	Univariate R ²	Bivariate R ²	Trivariate R ²	Univariate R ²	Bivariate R ²	Trivariate R ²
<i>D/d</i> = 1.043	0.9985	0.9765	0.9651	0.9984	0.9942	0.9047
<i>D/d</i> = 1.089	0.9980	0.9887	0.9661	0.9994	0.8609	0.9843
<i>D/d</i> = 1.14	0.9981	0.8640	0.9833	0.9996	0.8058	0.9766
<i>D/d</i> = 1.20	0.9994	0.7590	0.9378	0.9996	0.8979	0.9884
Total	0.9940	0.5882	0.8523	0.9970	0.5588	0.8539

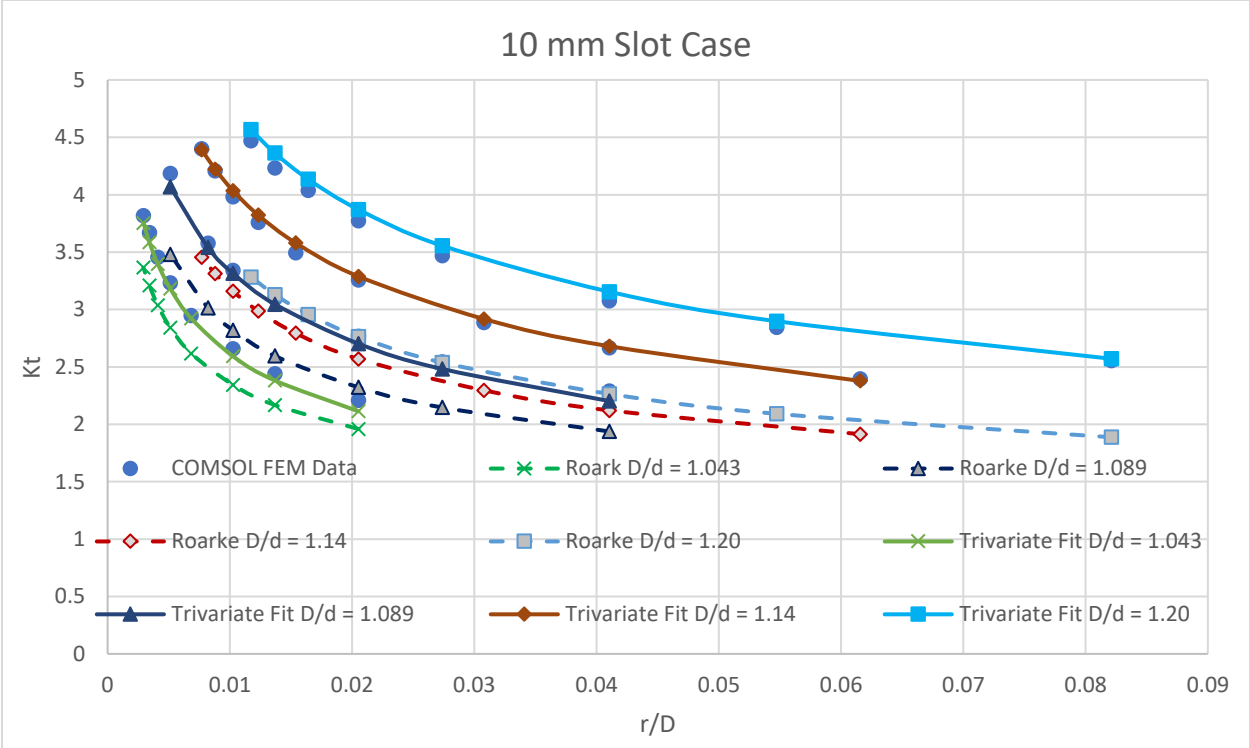


Figure A.1 Roark Type 5 Irregularity vs. Trivariate Fit for 10 mm Slots. As the D/d ratio increases, Roark’s fit becomes less and less accurate, while the Trivariate Fit maintains its accuracy throughout.

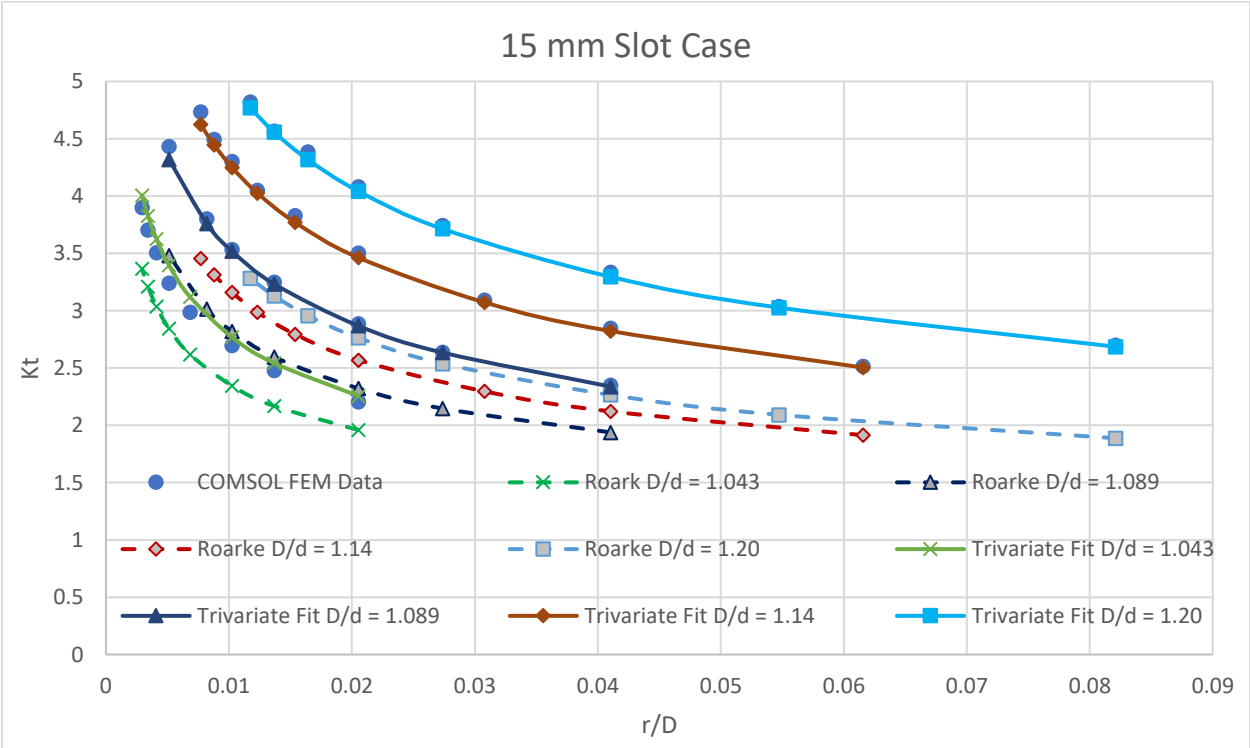


Figure A.2 Roark Type 5 Irregularity vs. Trivariate Fit for 15 mm Slots. Just as with the 10 mm Slots, Roark’s fit decreases in accuracy as D/d increases, while the Trivariate Fit maintains its accuracy throughout.

Appendix B. Stress Concentration Factor Supplemental Derivation

Within this appendix, the governing equation and assumptions that influenced the results shown within Chapter 2 are discussed in more detail. While the material relating to the stress concentration factors is discussed within the chapter itself, the information here will focus on the equations governing the optimization protocol used to refine the designs. The first point to discuss relates to the buckling load calculation shown within Eq. (2.8), which is repeated here for reference.

$$P_{cr} = \frac{P_e}{1 + \frac{\eta P_e}{AG}} \quad (2.8)$$

Within Eq. (2.8), P_e is calculated using the standard Euler Bernoulli formulation of the buckling problem:

$$[K] + P_e[N] = \{0\} \quad (B1)$$

The stiffness of the graphite-epoxy inner face sheet is calculated within each iteration as a function of the ply thicknesses of the $[0\ 90]_s$ laminate layup, which are included as design variables within the problem. For each layer of the laminate, the stiffness is calculated using [51]:

$$[Q_0] = \begin{bmatrix} \frac{E_A}{\Delta} & \frac{\nu_A E_T}{\Delta} & 0 \\ \frac{\nu_A E_T}{\Delta} & \frac{E_T}{\Delta} & 0 \\ 0 & 0 & G_A \end{bmatrix}, \text{ where } \Delta = 1 - \nu_A \left(\frac{\nu_A}{E_A} E_T \right) \quad (B2)$$

As before, E represents the Young's Modulus of the material, with the subscripts A and T indicating the axial and transverse directions, respectively. Poisson's ratio is represented by ν_A , while the shear modulus is represented by G_A . With each ply's local stiffness Q_0 specified, the global stiffness for the composite is assembled using the following set of equations:

$$\bar{Q}_{11} = Q_{11} \cos^4 \theta + Q_{22} \sin^4 \theta + 2(Q_{12} + 2Q_{66}) \sin^2 \theta \cos^2 \theta \quad (B3)$$

$$\bar{Q}_{22} = Q_{11} \sin^4 \theta + Q_{22} \cos^4 \theta + 2(Q_{12} + 2Q_{66}) \sin^2 \theta \cos^2 \theta \quad (B4)$$

$$\bar{Q}_{12} = (Q_{11} + Q_{22} - 4Q_{66}) \sin^2 \theta \cos^2 \theta + Q_{12}(\cos^4 \theta + \sin^4 \theta) \quad (B5)$$

$$\bar{Q}_{66} = (Q_{11} + Q_{22} - 2Q_{12} - 2Q_{66}) \sin^2 \theta \cos^2 \theta + Q_{66}(\sin^4 \theta + \cos^4 \theta) \quad (B6)$$

$$\bar{Q}_{16} = (Q_{11} - Q_{12} - 2Q_{66}) \cos^3 \theta \sin \theta - (Q_{22} - Q_{12} - 2Q_{66}) \cos \theta \sin^3 \theta \quad (B7)$$

$$\bar{Q}_{26} = (Q_{11} - Q_{12} - 2Q_{66}) \cos \theta \sin^3 \theta - (Q_{22} - Q_{12} - 2Q_{66}) \cos^3 \theta \sin \theta \quad (B8)$$

$$[\bar{Q}] = \begin{bmatrix} \bar{Q}_{11} & \bar{Q}_{12} & \bar{Q}_{16} \\ \bar{Q}_{12} & \bar{Q}_{22} & \bar{Q}_{26} \\ \bar{Q}_{16} & \bar{Q}_{26} & \bar{Q}_{66} \end{bmatrix} \quad (B9)$$

Derivation

The final \bar{Q} matrix is assembled by rotating each individual ply's stiffness matrix Q_0 into the global reference frame by their fiber angle θ [52].

With each ply's stiffness matrix in the shared reference frame, the ABD matrix shown in Eq. (B14) is calculated using:

$$[A] = \sum_{k=1}^N [\bar{Q}]_k (z_k - z_{k-1}) = \sum_{k=1}^N [\bar{Q}]_k t_k \quad (\text{B10})$$

$$[B] = \frac{1}{2} \sum_{k=1}^N [\bar{Q}]_k (z_k^2 - z_{k-1}^2) = \sum_{k=1}^N [\bar{Q}]_k t_k \bar{z}_k \quad (\text{B11})$$

$$[D] = \frac{1}{3} \sum_{k=1}^N [\bar{Q}]_k (z_k^3 - z_{k-1}^3) = \sum_{k=1}^N [\bar{Q}]_k \left(t_k \bar{z}_k^2 + \frac{t_k^3}{12} \right) \quad (\text{B12})$$

The ABD matrix allows for the thickness of each ply t_k to be accounted for in the design, alongside their midplane distances above or below the composite's global midplane \bar{z}_k [52]. The equivalent Young's Modulus for the full composite face sheet is then calculated by dividing both sides of Eq. (B10) by the total thickness of the composite face sheet, taking the A portion of the ABD matrix as an equivalent to the standard stress-strain relationship for a symmetric composite, whose B matrix would be approximately zero and non-axial sides are assumed to be unstressed. This results in Eq. (B13)

$$E_g \approx \frac{A_{11}}{t_g} = \frac{1}{t_g} \sum_{k=1}^N \bar{Q}_{11} t_k \quad (\text{B13})$$

$$\begin{Bmatrix} N_x \\ N_y \\ N_{xy} \\ M_x \\ M_y \\ M_{xy} \end{Bmatrix} = \begin{bmatrix} A & B \\ B & D \end{bmatrix} \begin{Bmatrix} \epsilon_{xx}^0 \\ \epsilon_{yy}^0 \\ \gamma_{xy}^0 \\ \kappa_x \\ \kappa_y \\ \kappa_{xy} \end{Bmatrix} \quad (\text{B14})$$

with the equivalent Young's Modulus for the graphite-epoxy face sheet E_g calculated, the eigenvalue buckling load P_e can be calculated, then then Timeshenko knockdown factor applied as in Eq. (2.8).

With the buckling load formulated, the mass acts as the second objective in the optimization procedure and is calculated simply as the volume of each material multiplied by their respective densities. Chapter 2 discusses the nine design variables, as well as some of the physical constraints. For a given buckling load, the amount of load carried by each material is calculated using a strain matching condition. The form shown in Eq. (B15) includes the offset parameter required for a waveguide to be fully stressed at its slot corners, but one constraint within the problem

Stress Concentration Factor Supplemental Derivation

formulation dictates that the resulting required offset δ must be less than the displacement created by simply loading the fiberglass and graphite epoxy layers alone. Doing so ensures that designs utilizing the offset would not fail before reaching the required value, thereby negating its advantages.

$$\frac{P_g}{E_g A_g} = \frac{P_f}{E_f A_f} = \frac{\sigma_{yield}}{K_t E_c} + \frac{\delta}{L}, \quad \text{where } P_{cr} = P_g + P_f + \frac{\sigma_{yield} * A_c}{K_t} \quad (\text{B15})$$

The resulting loading and displacements are double checked against the results of the composite analysis shown in Eq. (B16). The resulting global axial strain ϵ_{xx} is checked against the value from Eq. (B15) to ensure the two methods are in agreement. With the strains matching, the stresses within the composite are determined for each ply, ensuring that neither the 0s nor the 90s fail in either axial or transverse stress. The global strain and curvature vector is used to determine the local strains within each ply, which can then be used to determine their component stresses:

$$\begin{Bmatrix} \epsilon_{xx} \\ \epsilon_{yy} \\ \epsilon_{xy} \end{Bmatrix} = \begin{Bmatrix} \epsilon_{xx}^0 \\ \epsilon_{yy}^0 \\ \gamma_{xy}^0 \end{Bmatrix} + z \begin{Bmatrix} \kappa_x \\ \kappa_y \end{Bmatrix} \quad (\text{B16})$$

$$\begin{Bmatrix} \sigma_{xx} \\ \sigma_{yy} \\ \sigma_{xy} \end{Bmatrix} = [\bar{Q}]_k \begin{Bmatrix} \epsilon_{xx} \\ \epsilon_{yy} \\ \epsilon_{xy} \end{Bmatrix} \quad (\text{B17})$$

The final point of clarification revolves around the creation of Eq. 9 itself. The base of the equation lies in the strain matching condition, but inclusion of the offset required the addition of the δ term. One may specify an initial offset and use it to calculate the resulting strain in each material, but the form in Eq. (B15) centered on determining the minimum offset required to produce a design in which the waveguide would be fully stressed at its slot corners when the panel buckles. As a result, the relationship between the stress and strain of the waveguide, coupled with the stress concentration factor in Eq. (2.1), allowed for the offset itself to be determined from the desired failure load.

$$K_t = \frac{\sigma_{corner}}{\sigma_1} \quad (2.1)$$

$$\sigma_c = E_c \epsilon_c \quad (\text{B18})$$

$$\sigma_{yield} = K_t \sigma_c = K_t E_c \epsilon_c \quad (\text{B19})$$

This formulation is then combined with the offset, under the assumption that the total strain of the structure must match the strain within the copper added to the initial offset normalized by the waveguide length L .

Appendix C. AFRL Document

Modeling and Analysis of Slotted Waveguide Antenna Stiffened Structures Using CREATE Programs

Project: SENTRi Analysis of Slotted Waveguide Antenna Stiffened Structures (SWASS)

Scholar: Joseph Brooks

Mentor: Dr. John D'Angelo

Branch: RYMH

School: Virginia Polytechnic Institute

Abstract

Recent efforts to increase aircraft performance have led to proposals to integrate communications and radar structures into the skin of the aircraft itself. Current analyses have been conducted using commercial software, but analysis using the HPCMP's CREATE suite of programs is desired, as well as comparison against the existing models to validate viability. Initial models included the waveguide by itself as a test case, which demonstrated the overall radiation patterns were the same. However, frequency sweep data shows that CREATE-RF™ SENTRi's modeling of the thickness captures a shift in the peak gain frequency that the plate models of COMSOL do not. From there, the full model with supporting materials now allows for quick analysis of various material configurations, alongside ease in creation of panels to fit desired test aircraft.

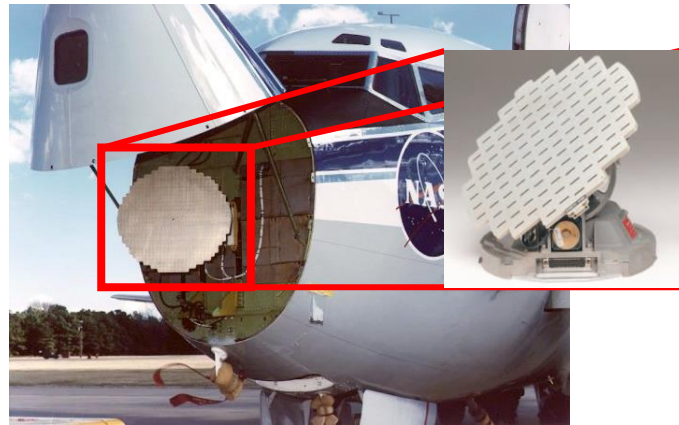


Figure C.1 Antenna Array Under a Radome. The slotted waveguide array is housed within the large void in the nose [1].

Introduction

Modern aircraft have developed into highly specialized machines, with even minute details within the design having large impacts on the aircraft's overall performance. One such area is the integration of radio frequency (RF) communications into the aircraft. These systems are typically designed independent of the aircraft to perform their purpose, then the aircraft itself is modified to accommodate them, often through the use of large interior spaces, as in Fig. C.1, or external antennae. With the former, the spaces limit the ability to modify the aircraft's shape or add additional structures, while the latter can adversely affect the aerodynamics of the aircraft, as well as potentially affect any stealth capabilities in more recent designs.

To combat these issues, the idea of conformal load-bearing antenna structures (CLAS) was created and analyzed by Paul Callus, in which the antennae are designed and integrated as part of the aircraft's structure. In this capacity, the antennae would now help to support part of the loading within the aircraft itself, rather than requiring loads be redirected away from them, with the aim being to improve the aircraft's overall performance and reduce its weight [3]. Callus's initial ideas coalesced into the idea of slotted waveguide antenna stiffened structures (SWASS), in which the honeycomb structure within the core of an aircraft's skin would be replaced by the antennae [4]. These ideas would be expanded upon in subsequent work, including that of Kim et al. [18], in which several designs were analyzed with various configurations. Design 4 is shown within Fig. C.2 and is used within this study. The design is composed of a copper waveguide surrounded by an electromagnetically (EM) transparent fiberglass shell, upper face sheet, and carbon fiber reinforced polymer (CFRP) supporting face sheet beneath.

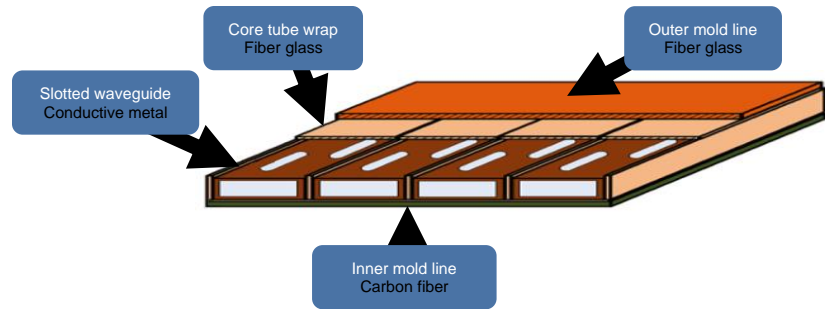


Figure C.2 SWASS Panel Design. The inner conductive material acts as the antenna, while the additional wrap and mold lines provide additional structural support.

Further analysis of the design has been conducted using the commercially available software COMSOL Multiphysics. However, due to the expense of such software, it was beneficial to the United States Air Force to develop equivalent models within their in-house modeling software. As such, the most recent work aimed to reproduce these models within CREATE-FT Capstone, allowing for subsequent analysis within CREATE-RFTM SENTRI, owned and operated by the Department of Defense's High-Performance Computing Group. Subsequent sections will detail the models and comparisons between the two software's results.

Experiment

The initial stages of the analysis involved recreating the waveguide models themselves within CREATE-FT Capstone. Fig. C.3 shows the nomenclature used for the overall dimensions, with Table 1 giving the corresponding numerical values. The first step in the experiment involved analyzing the waveguide by itself, so as to provide a base against which to compare later versions with the added layers and materials. Fig. C.4a shows the COMSOL model, while Fig. C.4b shows the equivalent CREATE-FT Capstone model. It should be noted that, due to the differences in analysis methods, the COMSOL model requires a volume of air in addition to the waveguide itself, while the CREATE-FT Capstone model does not.

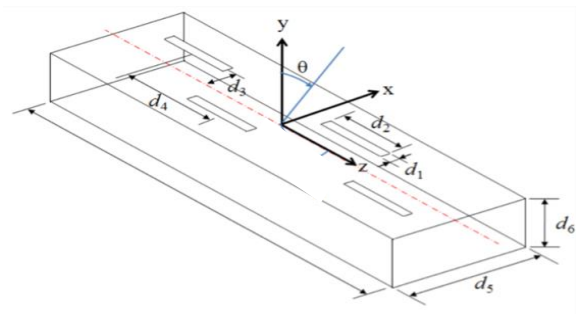


Figure C.3 Waveguide Dimensions. A slotted waveguide's dimensions are divided between those corresponding to the slot size (d_1 and d_2), slot locations (d_3 and d_4), and waveguide dimensions (d_5 and d_6).

Table C.1 Nominal Waveguide Dimensions. The base waveguide dimensions correspond to a WR-90 designed to operate at a frequency of 10 GHz.

Nominal Dimensions	Representative	Value (mm)
Slot Width	d1	2
Slot Length	d2	15
Slot Offset (mid-slot to mid-line)	d3	2
Slot Spacing	d4	20
Waveguide Width	d5	22.86
Waveguide Height	d6	10.16
Waveguide Length	L	240
Copper Thickness	tc	0.75
Fiberglass Thickness	tf	0.75
Graphite Epoxy Thickness	tge	0.75

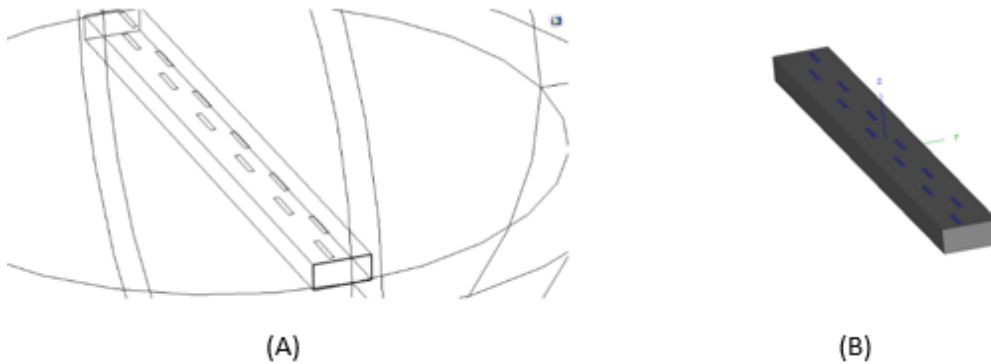


Figure C.4 A) COMSOL Waveguide Model and B) CREATE-FT Capstone Waveguide Model. The COMSOL model shows the spherical volume of air modeled around the waveguide itself, while the waveguides themselves are consistent with one another.

For the analysis of each model, creating the waveguide model depends upon which stage of analysis being conducted. For the base waveguide, the outer waveguide is defined before the central void and slots are separated from the previously solid block model. For the later models that include the surrounding fiberglass sleeve and supporting face sheets, such as the one shown in Fig. C.5, the sleeve must be defined first, before the waveguide, slots, and central void are defined within it as before. The face sheets can be defined at the end, and then the ends of the void are defined just as before. At each end of the central void, one end is defined as the same material as the waveguide itself, acting as a cap, while the other end is defined as a port, where the excitation frequency can be applied. The final model analyzed consists of a panel of 5 waveguides merged together. Fortunately, each base waveguide is the same as the individual

ones in Fig. C.5, which can then be expanded using an array to develop an array of any desired length, as shown in Fig. C.6.

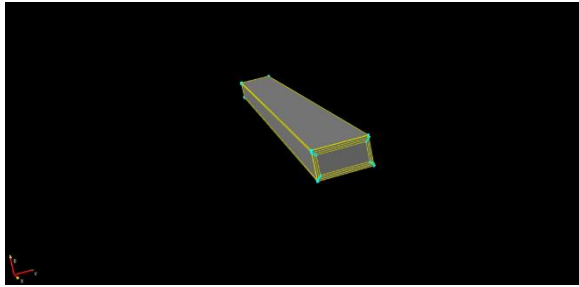


Figure C.5 Full Waveguide Model. The full model includes the metallic waveguide at the center, along with the additional supporting sleeve and face sheets.

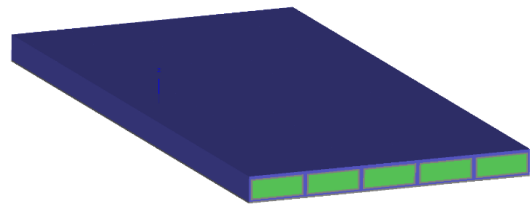


Figure C.6 Full Panel Model. Five identical versions of the previous full waveguide model are combined in an array to create an example panel, but can be varied for any desired size

Data/Results

Using the models of the waveguides alone, the first steps in the analysis revolved around applying a 10 GHz excitation to the model in both COMSOL and CREATE-RF™ SENTRI, then comparing the resulting radiation patterns. Fig. C.7a shows the COMSOL pattern, while Fig. C.7b shows the CREATE-RF™ SENTRI pattern. Both radiation patterns have similar shapes, but vary in their maximum values. For the COMSOL model, the maximum gain was approximately 17.61 dB, while the CREATE-RF™ SENTRI model’s maximum gain was approximately 13.57 dB.

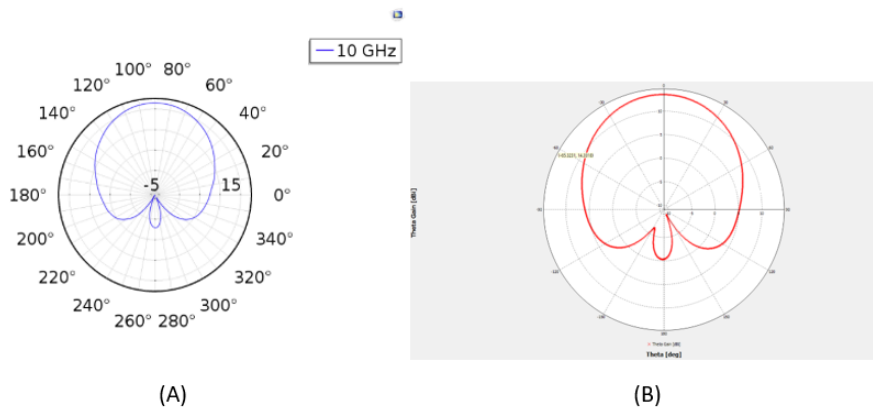


Figure C.7 A) COMSOL 10 GHz Radiation Pattern and B) CREATE-RF™ SENTRI 10 GHz Radiation Pattern. Both models show the circular radiation pattern with decreasing magnitude as you move away from the vertical immediately above the slotted surface.

The variation in maximum gain values prompted a frequency sweep between 8 GHz and 12 GHz. Fig. C.8 shows the results of the sweep within COMSOL while Fig. C.9 shows the results of the sweep within CREATE-RF™ SENTRI. The shapes both show a central operating range, but with the COMSOL data seemingly centered around 10.1 GHz, while the CREATE-RF™ SENTRI data is centered closer to 10.3 GHz.

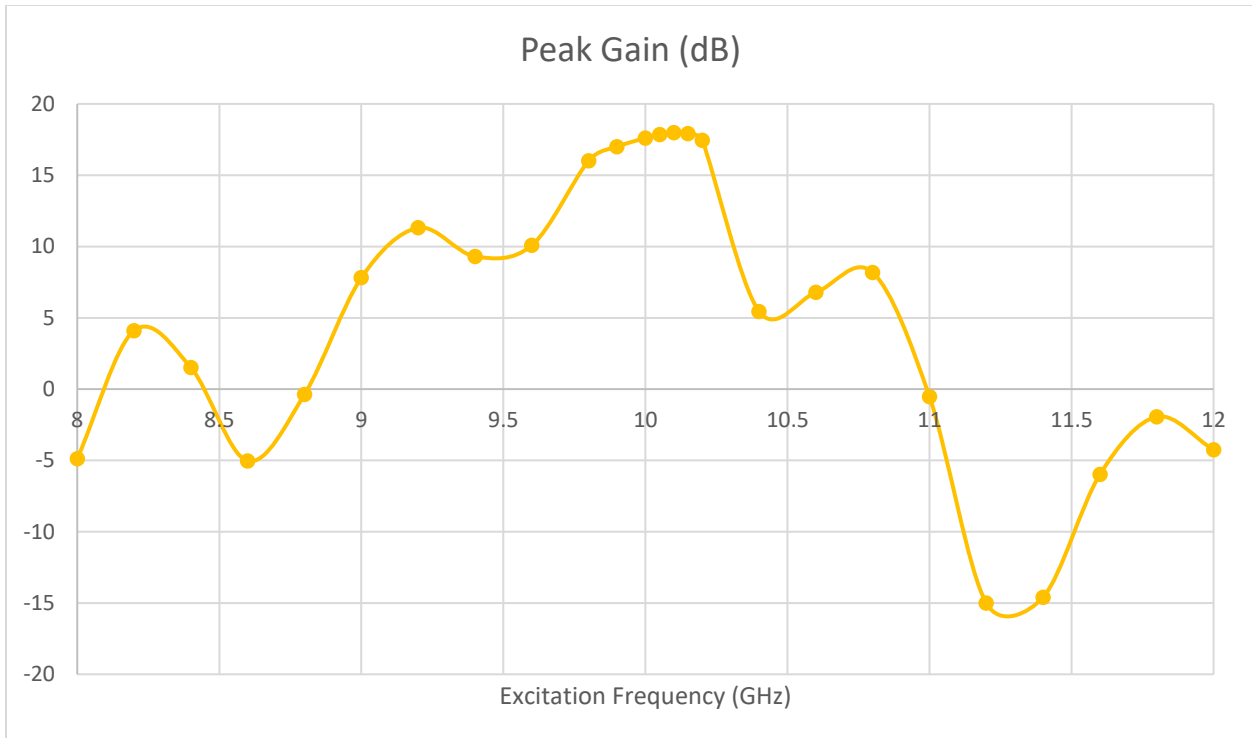


Figure C.8 COMSOL Frequency Sweep Peak Gain Values. The waveguide’s design appears to keep the peak frequency closer to the 10 GHz design of a WR-90 style waveguide antenna. Smaller gain values seem to indicate a wider operating range between 8.9 GHz and 10.9 GHz.

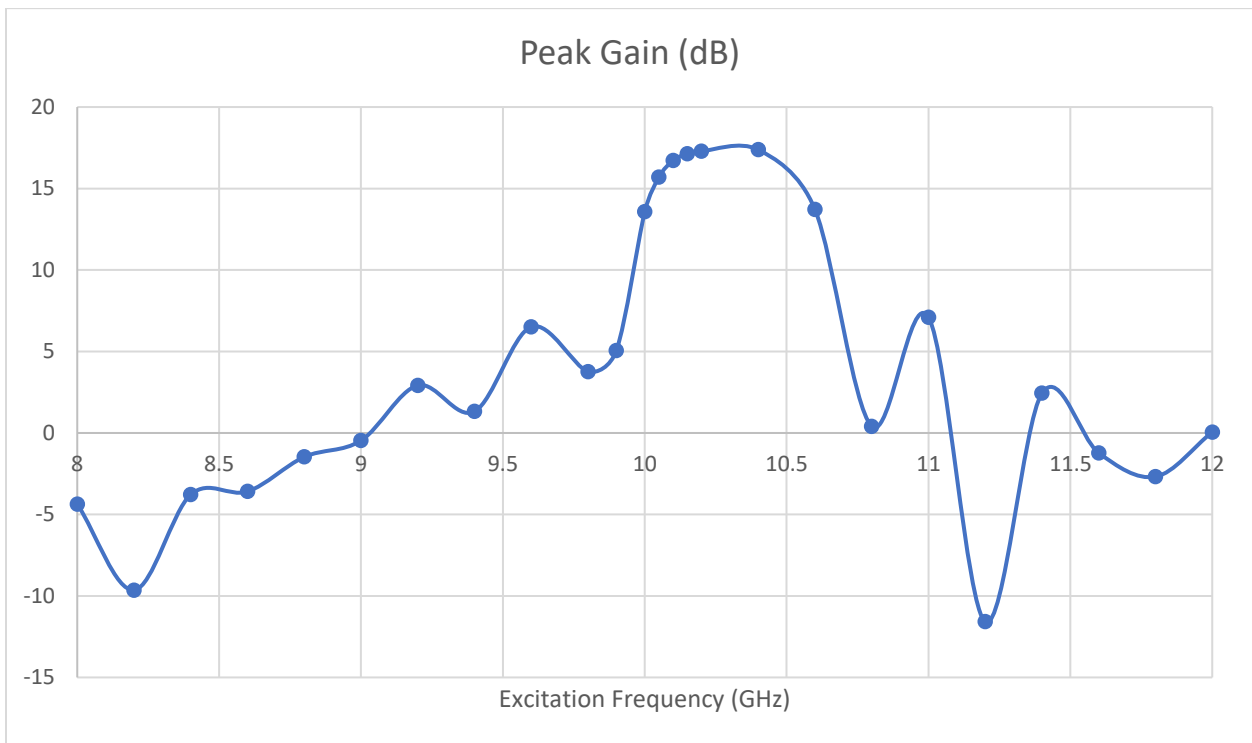


Figure C.9 CREATE-RF™ SENTRi Frequency Sweep Peak Gain Values. The inclusion of the waveguide’s thickness appears to have shifted the peak frequency closer to 10.3 GHz and slightly narrowed the operating range to between 9.1 GHz and 10.7 GHz.

With the peaks identified, the next step in the analysis involved adding in the additional materials to create the full model shown in Fig. C.4. When analyzed within CREATE-RF™ SENTRI, the radiation pattern closely resembled that within Fig. C.7b. The full panel was analyzed next, with Fig. C.11 showing the results of each port being fired within CREATE-RF™ SENTRI, while Fig. C.10 shows the composite version where all five ports are fired simultaneously in COMSOL.

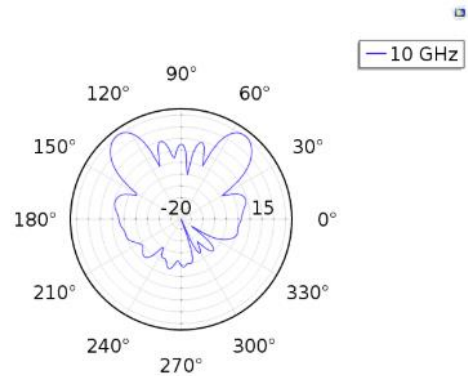


Figure C.10 COMSOL Panel Radiation Pattern for Simultaneous Firing. The patterns from each waveguide combine in a way that results in two main lobes approximately 40 degrees off from vertical.

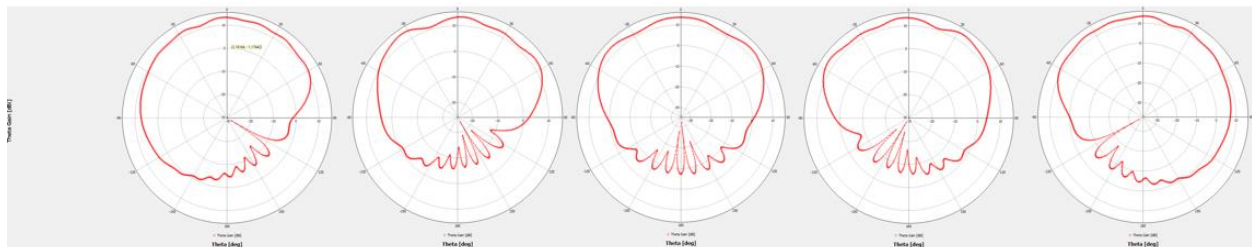


Figure C.11 CREATE-RF™ SENTRI Radiation Patterns for Each of the Five Port Fired Individually. Each port appears to resemble a slightly rotated version of the single waveguide's pattern in Fig. C.7b, changed due to the presence of the other waveguides.

Discussion/Conclusion

The similarities in shapes for the individual waveguides support the idea that both programs are reporting accurate data. Such a claim is aided by the frequency sweep data, which shows that the differences between the plate models in COMSOL and the modeled thicknesses of the CREATE-RF™ SENTRI model result in changes to the peak gain frequency. As the peak frequency is shifted further away from 10 GHz, this results in the maximum gain decreasing, likely explaining the lower magnitude, but similar shape. The variation supports the need to model the thickness of the waveguide fully, as its effects can lead to additional changes in the performance of the waveguides, alongside the dimensions of the slots.

Due to the similarities between the radiation patterns of the full model and the waveguide only model, it is possible to now capture the effects of changing the materials within the supporting materials. The current models simply denote materials as EM transparent, or impenetrable, but changing these to match the desired material properties can allow nuances to be seen. Additionally, the current general models allow for this to be done for as many materials as desired, allowing for multiple designs to be tested quickly in any future work. Such a possibility extends further into the panel model, as it is designed off of several identical versions of this base full model in an array that can be extended to any desired length. Future work can likely implement such designs as needed, along with phasing the ports such that the main radiation lobe is pointed in the desired direction. A final, long-term goal, would be to add these panels into larger models of the desired aircraft, allowing the observer to see how the aircraft itself affects the radiation patterns.

Appendix D. Offset Gap Term Derivation

Within this appendix, the update procedure used to account for the offset (gap) in the eigenvalue buckling analysis in Chapter 4 is shown in greater detail. The exact nature of the representative equations for axial and transverse displacements will vary depending upon which beam elements are employed, such as Euler-Bernoulli beam elements or Timoshenko beam elements. In both cases, the equations used will be composed of some combination of both linear equations and the Hermite Cubic equations, with the former being used for axial deformation regardless of the element type chosen for transverse deflection.

$$N_{a1}(x) = 1 - \frac{x}{L} \quad (D1)$$

$$N_{a2}(x) = \frac{x}{L} \quad (D2)$$

$$N_1(x) = 1 - 3\left(\frac{x}{L}\right)^2 + 2\left(\frac{x}{L}\right)^3 \quad (D3)$$

$$N_2(x) = x - 2\frac{x^2}{L} + \frac{x^3}{L^2} \quad (D4)$$

$$N_3(x) = 3\left(\frac{x}{L}\right)^2 - 2\left(\frac{x}{L}\right)^3 \quad (D5)$$

$$N_4(x) = -\frac{x^2}{L} + \frac{x^3}{L^2} \quad (D6)$$

Discretizing Eq. 4.14 in terms of these chosen equations and nodal displacements/rotations $\{a\}$ results in:

$$\begin{aligned} \delta^{(1)}\Pi = 0 = & \int_0^L [EA\{\delta a\}^T [N'_a][N'_a]\{a\} + EQ\{\delta a\}^T [N'_a][N'']\{a\} + EQ\{\delta a\}^T [N''] [N'_a]\{a\} \\ & + EI\{\delta a\}^T [N''] [N'']\{a\} - EA\{\delta a\}^T [N'_a][N'_a]\{a_0\} - EQ\{\delta a\}^T [N''] [N'_a]\{a_0\} \\ & - EQ\{a\}^T [N'_a][N'']\{a_0\} - EI\{a\}^T [N''] [N'']\{a_0\} \\ & + P(\{\delta a\}^T [N'_a] + \{\delta a\}^T [N'_a][N'_a]\{a\} + \{\delta a\}^T [N''] [N'']\{a\})] dx - \{\delta a\}^T \{F\} \end{aligned} \quad (D7)$$

Looking first at the Euler-Bernoulli beam element, the characteristic equations are represented as:

$$w(x) = N_1 w_1 + N_2 \theta_1 + N_3 w_2 + N_4 \theta_2 \quad (D8)$$

Offset Gap Term Derivation

$$u(x) = N_{a1}u_1 + N_{a2}u_2 \quad (D9)$$

While the procedure outlines in Eqs. (4.19) - (4.21) remains the same, the use of Euler-Bernoulli beam elements reduces the matrices in Eqs. (4.22) and (4.23) reduce to:

$$[K] = \begin{bmatrix} \frac{EA}{L} & 0 & \frac{EQ}{L} & -\frac{EA}{L} & 0 & -\frac{EQ}{L} \\ 0 & \frac{12EI}{L^3} & \frac{6EI}{L^2} & 0 & -\frac{12EI}{L^3} & \frac{6EI}{L^2} \\ \frac{EQ}{L} & \frac{6EI}{L^2} & \frac{4EI}{L} & -\frac{EQ}{L} & \frac{6EI}{L^2} & \frac{2EI}{L} \\ -\frac{EA}{L} & 0 & -\frac{EQ}{L} & \frac{EA}{L} & 0 & \frac{EQ}{L} \\ 0 & -\frac{12EI}{L^3} & -\frac{6EI}{L^2} & 0 & \frac{12EI}{L^3} & -\frac{6EI}{L^2} \\ -\frac{EQ}{L} & \frac{6EI}{L^2} & \frac{2EI}{L} & \frac{EQ}{L} & -\frac{6EI}{L^2} & \frac{4EI}{L} \end{bmatrix} \quad (D10)$$

$$[N] = \begin{bmatrix} \frac{1}{L} & 0 & 0 & -\frac{1}{L} & 0 & 0 \\ 0 & \frac{6}{5L} & \frac{1}{10} & 0 & -\frac{6}{5L} & \frac{1}{10} \\ 0 & \frac{1}{10} & \frac{2L}{15} & 0 & -\frac{1}{10} & -\frac{L}{30} \\ -\frac{1}{L} & 0 & 0 & \frac{1}{L} & 0 & 0 \\ 0 & -\frac{6}{5L} & -\frac{1}{10} & 0 & \frac{6}{5L} & -\frac{1}{10} \\ 0 & \frac{1}{10} & -\frac{L}{30} & 0 & -\frac{1}{10} & \frac{2L}{15} \end{bmatrix} \quad (D11)$$

For Eq. (4.21), the element lengths L would all be replaced by the initial length L_0 , as detailed in Chapter 4. To update the matrices using Eqs. (4.16) – (4.18), the governing equations are updated to the form shown in Przemieniecki [45]:

$$N_1(x) = \left(\frac{1}{1 + \Phi_s}\right) \left(1 - 3\left(\frac{x}{L}\right)^2 + 2\left(\frac{x}{L}\right)^3 + \left(1 - \frac{x}{L}\right)\Phi_s\right) \quad (D12)$$

$$N_2(x) = \left(\frac{L}{1 + \Phi_s}\right) \left(-\frac{x}{L} + 2\left(\frac{x}{L}\right)^2 - \left(\frac{x}{L}\right)^3 - \frac{1}{2}\left(\frac{x}{L} - \left(\frac{x}{L}\right)^2\right)\Phi_s\right) \quad (D13)$$

$$N_3(x) = \left(\frac{1}{1 + \Phi_s}\right) \left(3\left(\frac{x}{L}\right)^2 - 2\left(\frac{x}{L}\right)^3 + \frac{x}{L}\Phi_s\right) \quad (D14)$$

$$N_4(x) = \left(\frac{L}{1 + \Phi_s} \right) \left(\left(\frac{x}{L} \right)^2 - \left(\frac{x}{L} \right)^3 + \frac{1}{2} \left(\frac{x}{L} - \left(\frac{x}{L} \right)^2 \right) \Phi_s \right) \quad (\text{D15})$$

$$\text{where, } \Phi_s = \frac{12EI}{\kappa GA_s L^2} \quad (4.24)$$

These equations result in the forms of the matrices shown in Eqs. (4.22) and (4.23).

Appendix E. Panel Curve Fit Data

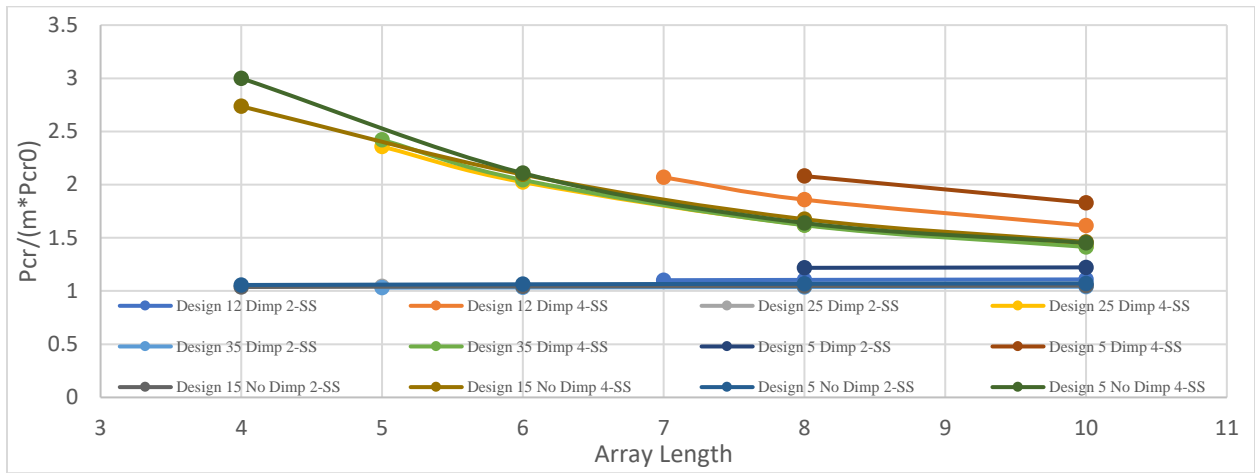


Figure E.1 Panel Buckling Data Sets. When pinned on two sides, designs buckle at loads roughly equal to the array length times the original buckling load, while designs pinned on four sides buckle at loads that exponentially decay towards the simply supported on two sides as the width approaches the length.

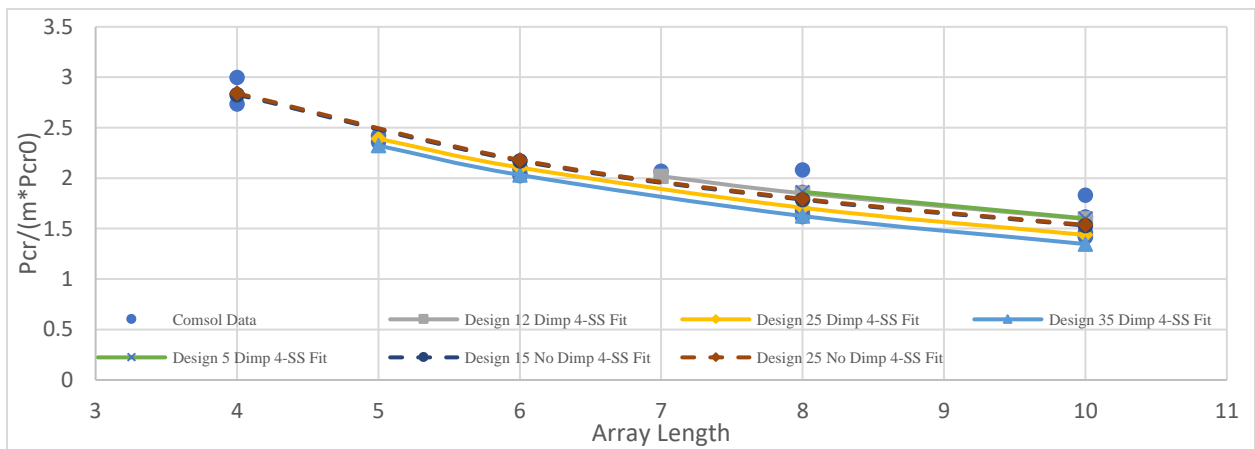


Figure E.2 Panel Buckling Fit. The curve fit closely matches the majority of data points, with only a single outlying set outside of the fit lines.

Appendix F. Design Variable Pareto Trends

Several distinct regions can be seen in the Pareto trends of the design variables. Fig. F.2 shows that the centerline offset was increased until constraint g_{18} prevents it from moving further out. Fig. F.3 shows that the height is linearly increased from its minimum to its maximum value before any other design variable, which occurs at roughly the same design as when the centerline offset reaches its maximum value and then influences the trends of the remaining design variables. Figs. F.7 and F.8 show that once the height reached its maximum value, the slope of the thickness of the outer mold line t_{fo} and the 0° ply t_{ga} increase, with t_{fo} 's slope increasing slightly once t_{ga} reaches its maximum value. Additionally, Fig F.6 shows that, while it increased alongside the height initially, once the height reached its maximum value, the sleeve thickness only increases slightly until the inner and outer mold lines are at their maximum values, after which it begins to increase again. Fig F.12 also shows that the gap length was increased alongside the sleeve thickness, but began to decrease as the sleeve was left constant and the inner and outer mold lines were thickened. Once the outer mold line reached its maximum value, the gap length began to increase slightly, with the rate of growth increasing further after the inner mold line reached its maximum and the sleeve thickness began increasing again.

In several of the plots, spikes can be seen at various points along each curve. The majority of these spikes are the result of noise from the solver attempting to converge during the optimization procedure. However, the spikes in Figs. F.2, F.10, and F.12 are more pronounced and occur as the active constraint switches between the dimpling constraints and the stress at the corner of the slots. Once all three dimpling constraints are no longer active and the corner stress constraint becomes the driving constraint, the spikes oscillations disappear in these variables, with only slight ones appearing in the copper thicknesses.

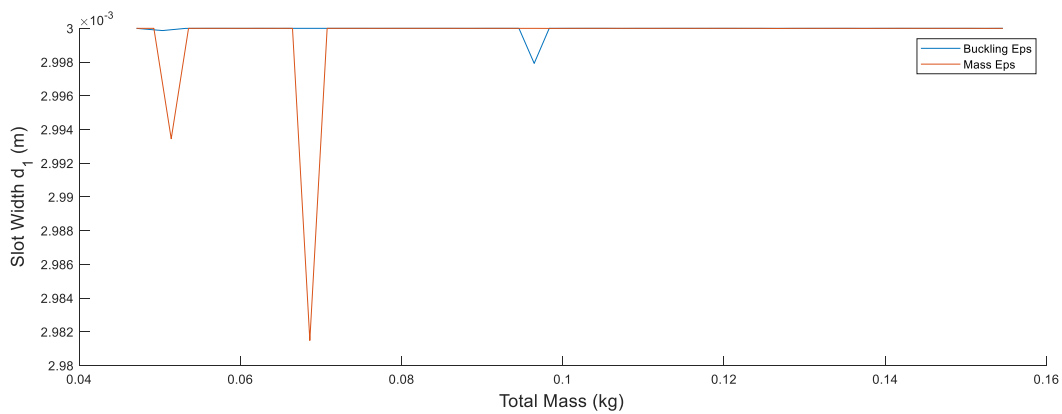


Figure F.1 Slot Width Pareto Trend. The Slot width remains at its maximum value with small spikes, likely from convergence issues.

Design Variable Pareto Trends

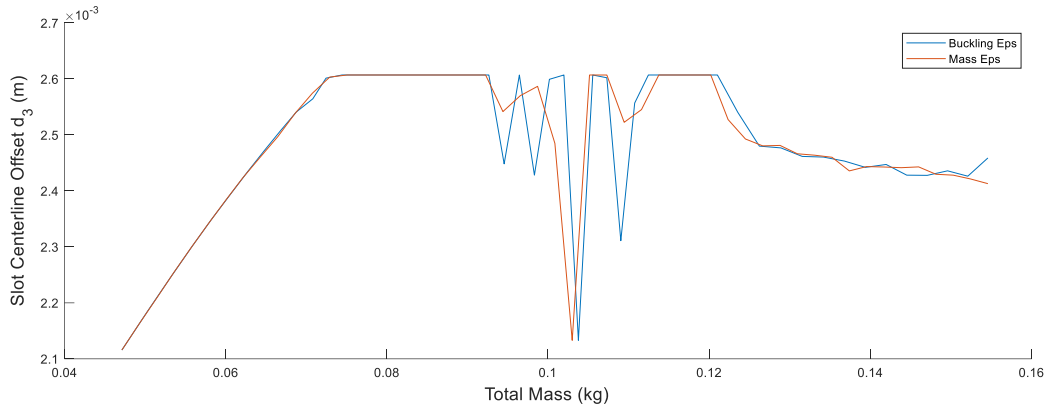


Figure F.2 Slot Centerline Offset Pareto Trend. The centerline offset increases it becomes 10 percent greater than the optimal value, followed by a region of instability as the active constraints change, then a slow decrease as the dimpling constraints deactivate.

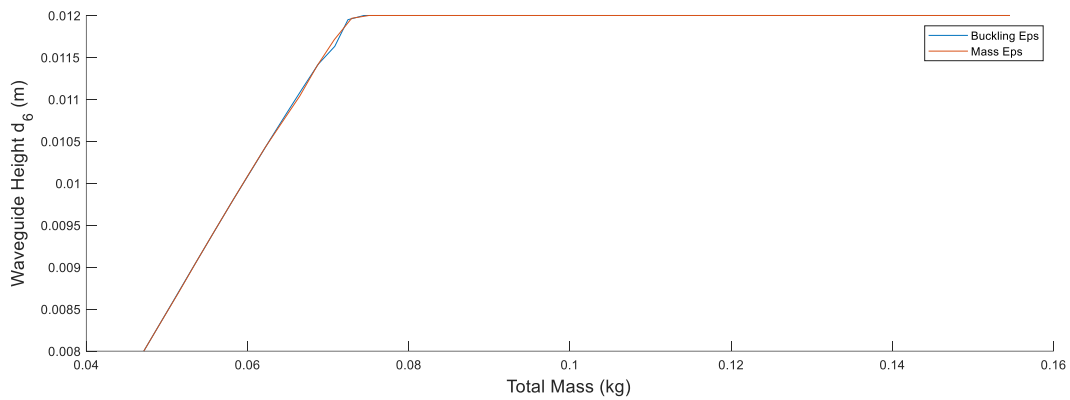


Figure F.3 Waveguide Height Pareto Trend. The height increases linearly from its minimum to its maximum to increase the stiffness of the designs.

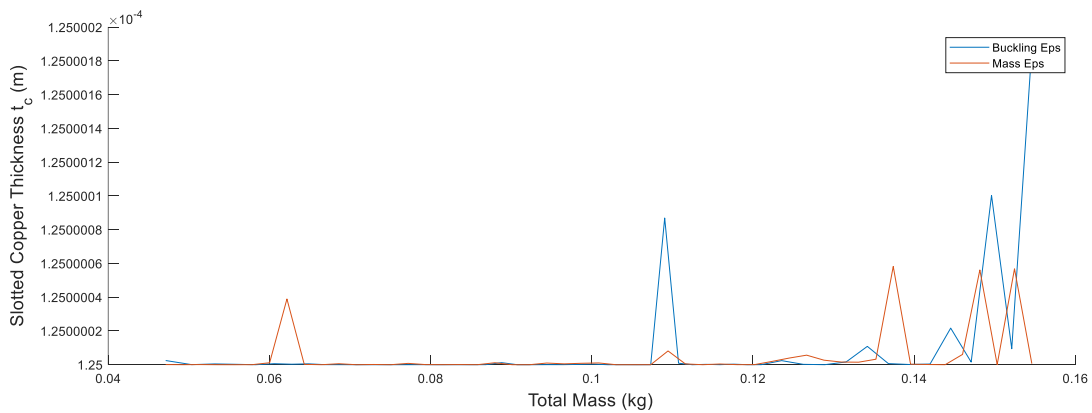


Figure F.4 Slotted Copper Thickness Pareto Trends. The slotted copper thickness remains roughly constant for all designs, with only slight variations caused by the convergence of the solver.

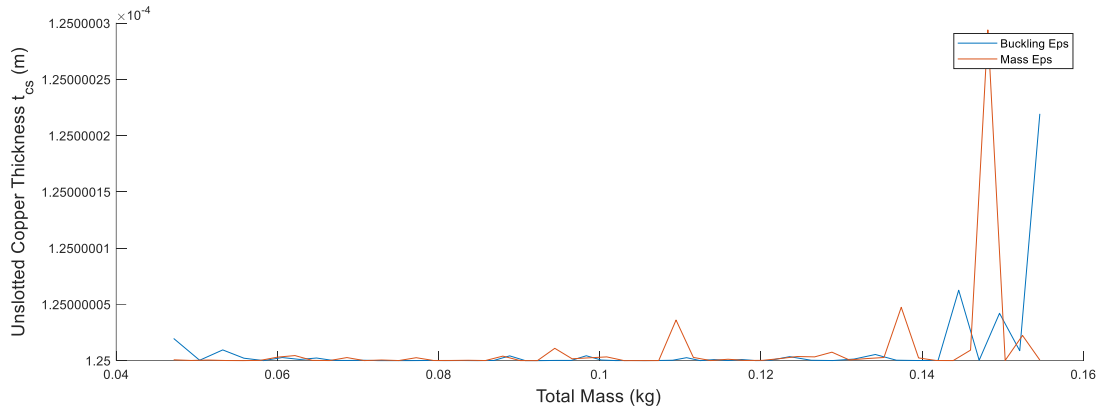


Figure F.5 Unslotted Copper Thickness Pareto Trends. The unslotted copper thicknesses remains roughly constant for all designs, with similar variations to the slotted copper thickness.

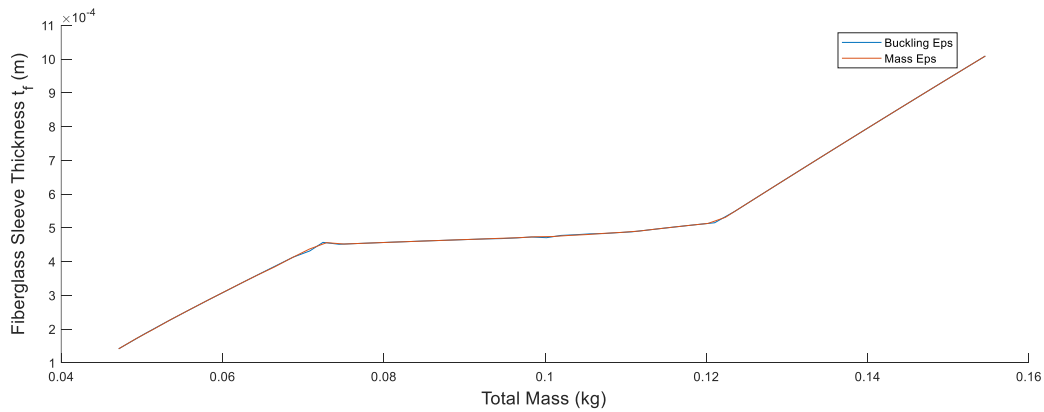


Figure F.6 Fiberglass Sleeve Thickness Pareto Trend. The sleeve thickness increases until reaching a point where the inner mold line begins to thicken for additional strength, remaining constant until the inner and outer mold lines have reached their maximum thicknesses.

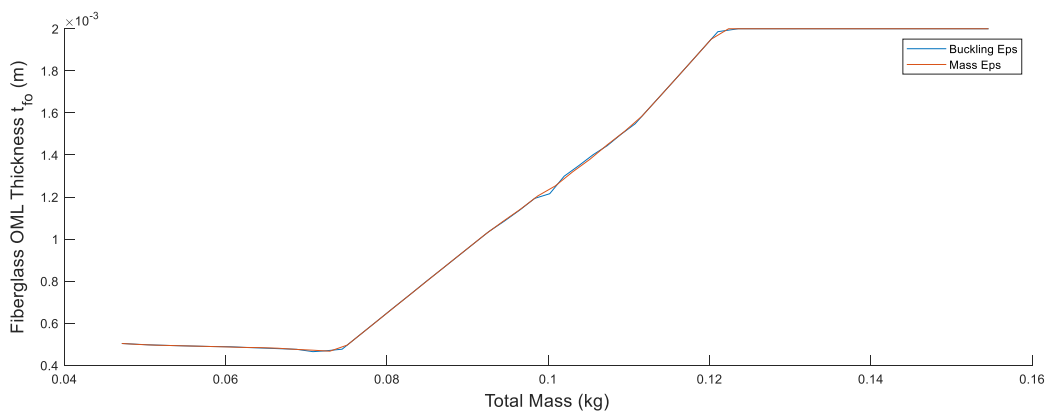


Figure F.7 Fiberglass OML Thickness Pareto Trend. The OML thickness remains small until the height peaks, after which it begins to increase linearly until reaching its maximum value.

Design Variable Pareto Trends

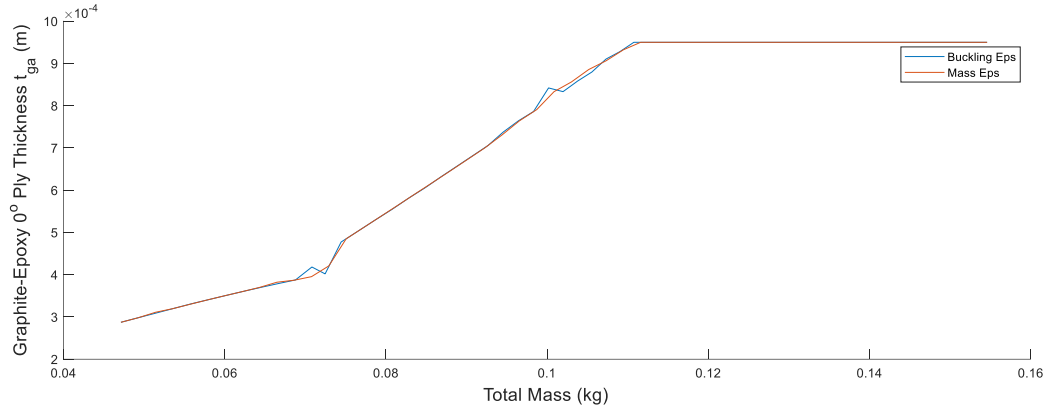


Figure F.8 0° Ply Thickness Pareto Trend. The 0° plys increases linearly, with the slope increasing slightly after the height reaches its maximum.

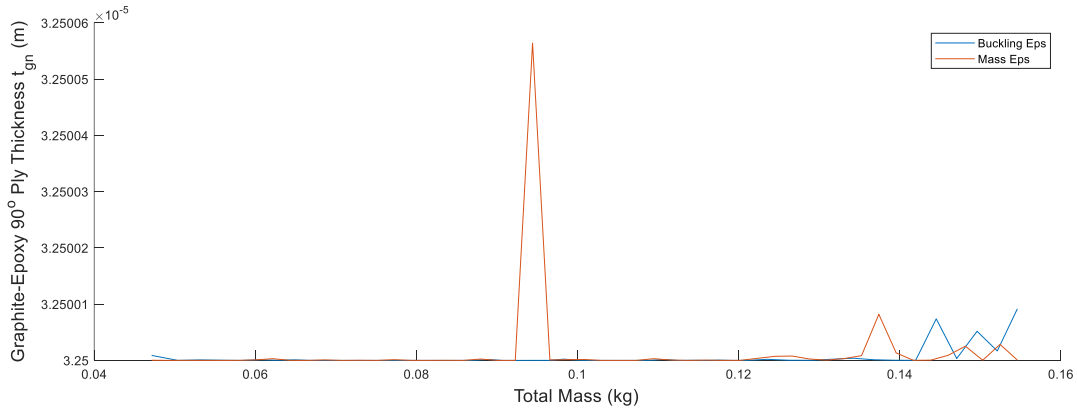


Figure F.9 90° Ply Thickness Pareto Trend. The 90° plys remained roughly at their minimum with slight variations due to convergence.

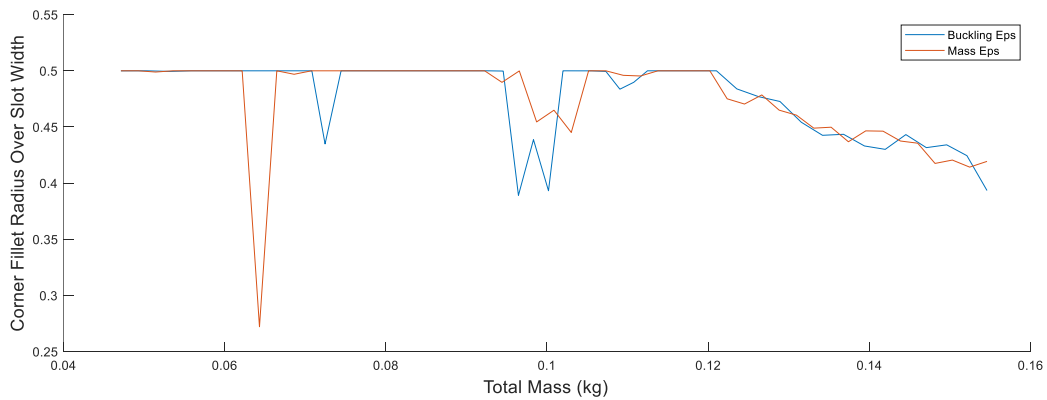


Figure F.10 Fillet Radius Over Slot Width Pareto Trend. The fillet radius remains close to its maximum of half the slot width, but has some variations where active constraints begin to change and begins to decrease as the designs become stiffer.

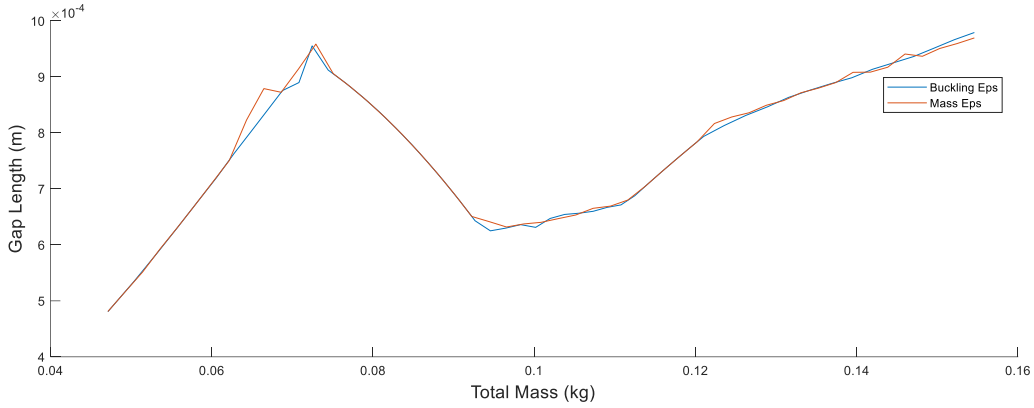


Figure F.11 Offset Pareto Trend. The offset increased linearly until the height reached its peak, after which it decreased as the inner and outer mold lines thickened, only increasing again once both reach their maximum values.

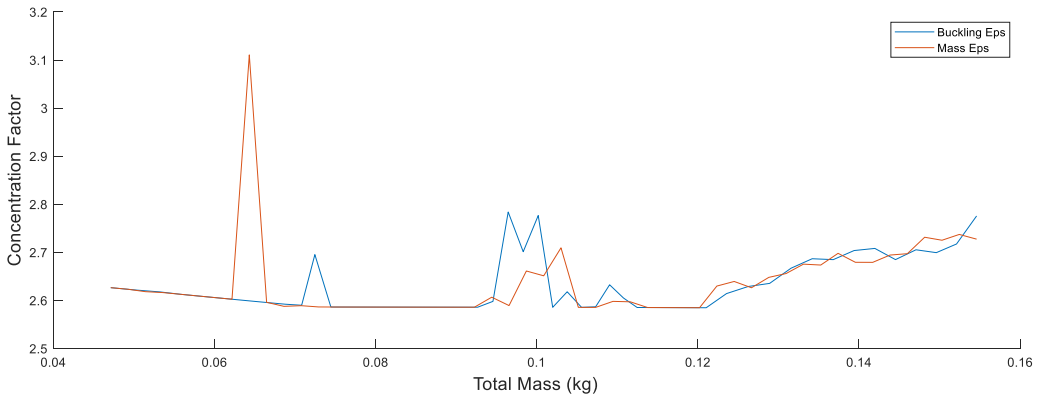


Figure F.12 Concentration Factor Pareto Trend. The concentration factor is kept low until the fillet radius begins to decrease in the higher mass designs.

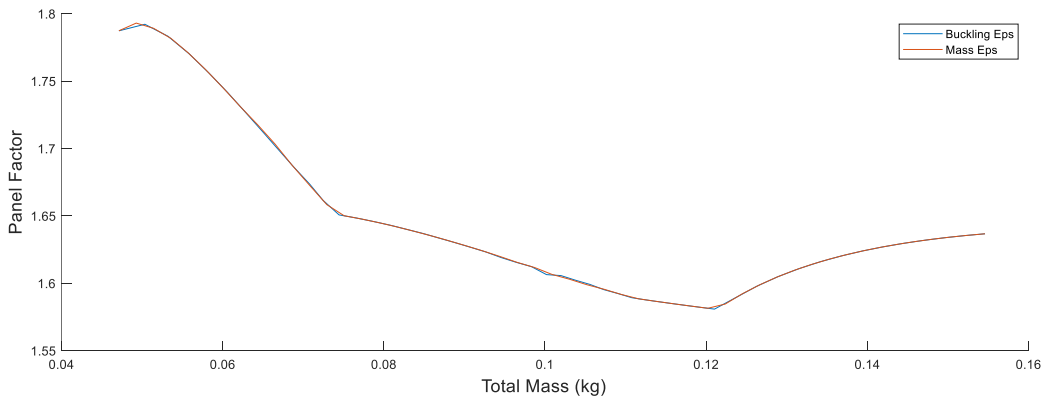


Figure F.13 Panel Factor Pareto Trend. As the designs become stronger, the panel factor decreases, not increase again until the inner and outer mold lines reach their maximum and the sleeve thickness begins increasing again.

References

- [1] NASA, *Airborne weather radar*, 2009.
- [2] U. S. Navy, *FA-18 Super Hornet VFA-41 retusche*, 2018.
- [3] P. J. Callus, "Conformal Load-Bearing Antenna Structure for Australian Defense Force Aircraft," Defense Science and Technology Organization, Victoria, Australia, 2007.
- [4] P. J. Callus, "Novel Concepts for Conformal Load-Bearing Antenna Structures," Defense Science and Technology Organization, Victoria, Australia, 2008.
- [5] P. J. Callus, K. J. Nicholson, A. Bojovschi, K. Ghorbani, W. Baron and a. J. Tuss, "A Planar Antenna Array Manufactured from Carbon Fiber Reinforced Plastic," in *28th International congress of the Aeronautical Sciences*, Brisbane, Australia, 2012.
- [6] J. Sabat, "Structural Response of the Slotted Waveguide Antenna Stiffened Structure Components Under Compression," Air Force Institute of Technology, Dayton, 2010.
- [7] A. Bojovschi, K. J. Nicholson, A. Galehdar, P. J. Callus and K. Ghorbani, "The Role of Fiber Orientation on the Electromagnetic Performance of Waveguides Manufactured from Carbon Fibre Reinforced Plastic," *Progress in Electromagnetics Research B*, vol. 39, pp. 267-280, 2012.
- [8] W. Kim, T. Ha and R. Canfield, "Radio Frequency Optimization of a Slotted Waveguide Antenna Stiffened Structure," Elsevier, Blacksburg, VA, 2014.
- [9] W. Kim and R. Canfield, "Design Optimization of Slotted Waveguide Antenna Stiffened Structures," Air Force Research Laboratory, Dayton, OH, 2014.
- [10] N. Albertson and R. Canfield, "Electromagnetic Modeling of Large Phased Arrays of Structurally Embedded Waveguides," in *58th AIAA/ASCE/AHS/ASC Structures, Structural Dynamics, and Materials Conference, AIAA SciTech Forum*, Grapevine, TX, 2017.
- [11] N. Albertson, "Electromagnetic and Mechanical Modeling of Large Phased Arrays of Structurally Embedded Waveguides," Blacksburg, VA, 2018.
- [12] A. J. Lockyer, K. H. Alt, D. P. Coughlin, M. D. Durham, J. N. Kudva, A. C. Goetz and J. Tuss, "Design and development of a conformal load-bearing smart skin antenna: overview of the AFRL Smart Skin Structures Technology Demonstration (S3TD)," *Smart Structures and Materials 1999: Industrial and Commercial Applications of Smart Structures Technologies*, Newport Beach, CA, 1999.
- [13] K. H. Alt, A. J. Lockyer, D. P. Coughlin, J. N. Kudva and J. Tuss, "Overview of the DoD's RF Multifunction Structural Aperture (MUSTRAP) Program," *Annual International Symposium on Smart Structures and Materials*, Newport Beach, CA, 2001.

- [14] B. P. Smallwood, R. A. Canfield and A. J. Terzuoli Jr., "Structurally Integrated Antennas on a Joined-Wing Aircraft," in *44th AIAA/ASME/ASCE/AHS Structures, Structural Dynamics, and Materials Conference*, Norfolk, VA, 2003.
- [15] M. Urcia and D. Banks, "Structurally Integrated Phased Arrays," in *2011 Aerospace Conference*, Big Sky, MT, 2011.
- [16] R. S. Elliott, "An Improved Design Procedure for Small Arrays of Slotted Slots," *IEEE Transactions on Antennas and Propagation*, Vols. AP-31, no. 1, pp. 48-53, 1983.
- [17] T. Ha and R. Canfield, "Design Optimization of a WR-90 Slotted Waveguide," in *52nd AIAA/ASME/ASCE/AHS/ASC Structures, Structural Dynamics and Materials Conference*, Denver, CO, 2011.
- [18] W. Kim, R. A. Canfield, W. Baron, J. Tuss and J. Miller, "Modeling and Simulation of Slotted Waveguide Antenna Stiffened Structures," in *19TH INTERNATIONAL CONFERENCE ON COMPOSITE MATERIALS*, 2013.
- [19] N. Alberston, *Electromagnetic and Mechanical Modeling of Large Phased Arrays of Structurally Embedded Waveguides*, Blacksburg, VA, 2018.
- [20] W. Young, R. G. Budynas and A. Sadegh, *Roark's Formulas for Stress and Strain*, 8th Ed., New York: McGraw-Hill, 2011.
- [21] J. Brooks and R. Canfield, "Slotted Waveguide Stress Concentration Factor," *AIAAJ*, vol. 60, no. 6, pp. 3844-3851, 2022.
- [22] W. Kim, R. A. Canfield, W. Baron, J. Tuss and J. Miller, "Structural Design and Optimization of Slotted Waveguide Antenna Stiffened Structures," *Carbon-Related Materials in Honor of Nobel Laureate Akira Suzuki's Lecture at IUMRS-ICEM 2018*, pp. 65-86, 2018.
- [23] *COMSOL Multiphysics Software Package, Ver. 5.2a*, COMSOL Inc..
- [24] W. D. Pilkey, *Peterson's Concentration Factors* 2nd Ed., New York, NY: Dover Publications, 1989.
- [25] T. J. Ortega, "X-47B UCAS Unmanned Combat Air System," Northrop Grumman Systems Corporation, San Diego, 2015.
- [26] S. Timoshenko and J. Gere, *Theory of Elastic Stability* 2nd Ed., New York, NY: Dover Publications Inc., 1989.
- [27] R. A. Canfield, "Quadratic Multipoint Exponential Approximation: Surrogate Model for Large-Scale Optimization," in *Advances in Structural and Multidisciplinary Optimization*, Springer International Publishing, 2017, pp. 648-661.
- [28] K. Schittkowski, "NLPQL: A FORTRAN Subroutine Solving Constrained Nonlinear Programming Problems," in *Annals of Operations Research*, 1986, pp. 485-500.

- [29] J. Brooks and R. Canfield, "Slotted Waveguide Stress Concentration Factor," *AIAA Journal*, vol. 60, no. 6, pp. 3844-3851, 2022.
- [30] *CREATE-RF SENTRI*, Department of High Performance Computing Modernization Program, 2022.
- [31] P. J. Bevelacqua, "Slotted Waveguide Antennas," 2019. [Online]. Available: <https://www.antenna-theory.com/antennas/aperture/slottedwaveguide2.php>. [Accessed 26 August 2022].
- [32] R. J. Stevenson, "Theory of Slots in Rectangular Waveguide," *Journal of Applied Physics*, vol. 19, pp. 4-20, 1948.
- [33] W. H. Watson, "Resonant Slots," *Journal of the Institution of Electrical Engineers - Part IIIA: Radiolocation*, vol. 93, pp. 747-777, 1946.
- [34] R. S. Elliott and L. A. Kurtz, "The Design of Small Slot Arrays," *IEEE Transactions on Antennas and Propagation*, vol. 26, pp. 214-219, 1978.
- [35] P. Wade, "Slot Antennas," in *The WIGHZ Online Microwave Antenna Book*, 2019.
- [36] J. Brooks and R. Canfield, "Multifidelity Design of Structurally Embedded Waveguides," *Pending Publication*, 2022.
- [37] J. S. Arora, "Multi-Objective Optimum Design Concepts and Methods," in *Introduction to Optimum Design: Fourth Edition*, New York, Academic Press, 2017, pp. 771-794.
- [38] *CREATE-FT Capstone*, Department of High Performance Computing Modernization Program, 2022.
- [39] R. Cook, D. Malkus, M. Plesha and R. Witt, "Formulation Techniques: Variational Methods," in *Concepts and Applications of Finite Element Analysis: Fourth Edition*, Madison, John Wiley & Sons, 2002, pp. 142-143.
- [40] V. K. Goyal and R. K. Kapania, "Dynamic Stability of Laminated Beams Subjected to Nonconservative Loading," *Thin Walled Structures*, vol. 46, no. 12, pp. 1359-1369, 2008.
- [41] I. H. Shames and C. L. Dym, "Finite Elements for Elastic Stability," in *Energy and Finite Element Methods in Structural Mechanics*, New York, NY, Taylor & Francis, 2003, p. 401.
- [42] J. Thomas, "A Finite Element Approach to the Structural Instability of Beam Columns, Frames, and Arches," George Marshall Space Flight Center, NASA, Marshall, 1970.
- [43] I. H. Shames and C. L. Dym, "Finite Elements for Elastic Stability," in *Energy and Finite Element Methods in Structural Mechanics*, New York, NY, Taylor & Francis, 2003, pp. 628-633.
- [44] J. Przemieniecki, "Inertia Properties of Structural Elements," in *Theory of Matrix Structural Analysis*, Mineola, Dover Publications Inc., 1985, pp. 74-80.
- [45] J. Przemieniecki, "Stiffness Properties of Structural Elements," in *Theory of Matrix Structural Analysis*, Mineola, Dover Publications Inc., 1985, pp. 293-295.

- [46] *AZO Materials*, Manchester.
- [47] S. B. Singh and D. Kumar, "Cutout Shape and Size Effects on Response of Quasi-Isotropic Composite Laminate Under Uni-axial Compression," *Structural Mechanics and Engineering*, vol. 35, no. 3, 2010.
- [48] H. M. Misilmani, M. Al-Husseini and K. Y. Kabalan, "Design of Slotted Waveguide Antennas with Low Sidelobes for High Power Microwave Applications," *Progress in Electromagnetics Research*, vol. 56, pp. 15-28, 2015.
- [49] R. P. Ley, W. Lin and U. Mbanefo, "Facesheet Wrinkling in Sandwich Structures," NASA CR-1999-208994, El Segundo, 1999.
- [50] B. McKinney, "Tests Prove That Tailless, Unmanned Jet Can Operate Safely in All Planned Flight Test Environments," Northrop Grumman, Palmdale, 2011.
- [51] E. J. Barbero, *Introduction to Composite Material Design 2nd Ed.*, New York, NY: CRC Press, 2010.
- [52] M. H. Dato, "Laminate Strength Analysis," in *Mechanics of Fibrous Composites*, New York, NY, Elsevier Science Publishers, 1991, pp. 248-366.
- [53] K. Schittkowski, "Design of Slotted Waveguide Antennas with Low Sidelobes for High Power Microwave Applications," in *Annals of Operations Research*, 1986, pp. 485-500.
- [54] S. P. Timoshenko and J. M. Gere, "Buckling of Thin Plates," in *Theory of Elastic Stability 2nd Edition*, Mineola, Dover Publications Inc., 2018, pp. 348-439.